Melting and Deformation of the Ross Ice Shelf, Antarctica, by Multi-Year Phase Sensitive Radio Echo Sounding

A thesis
submitted in partial fulfilment
of the requirements for the Degree
of
Master of Science
In Environmental Science

by

by Joseph A. Snodgrass

School of Earth and Environment
University of Canterbury
2021

Abstract

Antarctic ice shelves are an important part of the Antarctic ice sheet system, holding back the grounded ice front from accelerating onto the ocean and contributing to sea level rise. As ice shelves float on the ocean, they are the most vulnerable to oceanic and environmental changes. The oceans in the ice shelf cavity remain some of the most unexplored places in the world with only a few observations. The Ross Ice Shelf is the largest ice shelf in the world, buttressing 11.6m of potential sea level rise within its catchment. This study presents the first precision Autonomous Phase-sensitive Radio Echo Sounding (ApRES) measurements of ice shelf thickness, internal deformation and basal melting across an entire traverse of the Ross Ice Shelf.

Autonomous Phase-sensitive Radio Echo Sounding (ApRES) is a ground-based instrument that can record reflections of internal layers and the ice shelf base to millimetre precision using phase-based measurements. The ice shelf thickness change and internal deformation are used to determine basal melting. Phase coherence of stable internal and basal reflectors over the survey period allows this type of analysis.

Up to 5 seasons of annual ApRES measurements were collected at 32 locations along the South Pole Overland Traverse (SPOT) and Siple Coast Traverse (SCT). The survey covered a 1000km transect of the Ross Ice Shelf (RIS) from Mina Bluff to the Kamb Ice Stream (KIS). Strong basal reflection strength in the north and southern regions indicated well-defined ice-ocean interfaces formed from basal melting. Weaker reflections and lower apparent thickness across the central RIS sites indicated the presence of marine ice or debris.

Basal melting was 0-0.02 m a^{-1} for a large area of the central RIS, with data gaps where marine ice and debris are present. Basal melting rises to 0.25-0.45 m a^{-1} at the southern and northern ends of this region due to the expected influence of High Salinity Shelf Water (HSSW) and Antarctic Surface Water (AASW) respectively. Basal melt rates of 0.01-0.04 m a^{-1} were consistent across the Siple Coast study area and reached 0.14 m a^{-1} within 11km of the KIS grounding zone. With increasing distance downstream from the KIS and WIS, the basal melting rate decreased and the strain thinning rate increased as the ice shelf continued to thin.

Remote sensing observations of basal melting must account for the dynamic thinning component of the total ice shelf thickness change. The MEaSUREs satellite velocity datasets were used with strain processing scripts from Alley et al. (2018) to calculate vertical strain deformation across the study area. The satellite-derived strain rates correlated well with the ApRES ground based strain rates, supporting the accuracy of current remote sensing deformation methods and basal mass balance studies. The ApRES basal melt rates showed similar patterns to those from remote sensing and ocean modelling but were generally smaller and less spatially variable. This indicates the RIS is maintaining steady state basal

mass rates across its interior. The spatial variability suggests there remains inaccuracies and uncertainties for remote sensing studies, possibly due to the accumulation models, that could be addressed by future ApRES or climate studies.

Acknowledgements

This project was only possible with the support of a significant number of people. I would first like to thank my supervisors Dr Wolfgang Rack and Dr Heather Purdie, for their outstanding support, encouragement, and knowledge throughout this project. It was a pleasure to work with you after years of dreaming of Antarctic research.

This thesis is the result of six seasons of fieldwork, organisation and planning as part of the Aotearoa New Zealand Ross Ice Shelf Programme (ANZRISP). I must express my thanks to the many people who organised and carried out the fieldwork: Daniel Price, Michelle Ryan, Wolfgang Rack, Christina Hulbe, Adrian MacDonald, Kelly Gragg and Martin Forbes. This research was only possible due to your hard work over the past six Antarctic seasons and the support of the ANZRISP.

Small opportunities grow, so thank you to Ngāi Tahu and Nigel Scott for providing the opportunity to attend the PCAS programme through Te Tauira a te Kaiwhakatere Scholarship. You opened the opportunities to Antarctic research, so I am very thankful for the support of my iwi.

To all my Gateway Antarctica and PCAS colleagues, you are the 'coolest' department on campus. I am extremely grateful to have been a part of it and wish you all the best in the future. I wish to especially thank the Gateway Antarctica' Ice Nerds': Shelley, Gemma, Dan, Rodrigo and Usama, for all their advice and ideas while trying to solve the problems arising throughout the work. The weekly meetings were a fantastic window out of COVID lockdowns.

This thesis is the culmination of a 5-year journey at the University of Canterbury. So, finally, thank you to my parents, my sisters, my whānau and friends for their unending encouragement and support throughout.

Ehara tōku toa I te toa takitahi. He toa takitini tōku toa.

My strength is not due to me alone, but due to the strength of many.

Table of Contents

List of Figures

List of Tables

Abbreviations

ANZRISP	Aotearoa New Zealand Ross Ice Shelf Project
ApRES	Autonomous phase-sensitive Radio Echo Sounding
BAS	British Antarctic Survey
CIR	Crary Ice Rise
CMI	Continental Meteoric Ice
EAIS	East Antarctic Ice Sheet
FMCW	Frequency Modulating Continuous Waveform
GPR	Ground Penetrating Radar
GPS	Global Positioning System
HF	High Frequency (Radio waves)
HSSW	High Salinity Shelf water
ISW	Ice Shelf Water
KIS	Kamb Ice Stream
LMI	Local Meteoric Ice
mCDW	Modified Circumpolar Deep Water
MIU	Marine Ice Unit
pRES	phase-sensitive Radio Echo Sounding
RIS	Ross Ice Shelf
SCT	Siple Coast Traverse
SLE	Sea Level Equivalent
SPOT	South Pole Overland Traverse
VHF	Very High Frequency (Radio waves)
VSR	Vertical Strain Rate
WAIS	West Antarctic Ice Sheet
WIS	Whillans Ice Stream

1 Introduction

The Antarctic ice Sheet holds 70% of the world's freshwater, which would raise sea-level rise by 58 meters when completely melted (Fretwell et al., 2013; Rignot et al., 2019). The marine West Antarctic Ice Sheet (WAIS) is the most vulnerable part of the ice sheet and contains 5-6 metres of sea-level rise potential (Alley & Bindschadler, 2001; Naish et al., 2009). Sea level projections for 2100 range from 0.26 – 0.82 m depending on the emission scenario (IPCC, 2014) and understanding ice sheet mass loss processes are important to improve sea level predictions and effective policy decisions into the future. Ice shelves are extensions of the grounded ice sheet but are floating on the ocean, losing mass through basal melting or iceberg calving (Depoorter et al., 2013; Rignot et al., 2013). As ice shelves are in direct contact with the ocean, they are vulnerable to both oceanic and atmospheric environmental change. This makes ice shelves the most vulnerable part of the Antarctic Ice Sheet system to global environmental change (Bindschadler et al., 2013; Mercer, 1978). Reduction or collapse of ice shelves leads to an imbalance of the grounded ice sheets due to loss of ice shelf buttressing (Rott et al., 2002). Nearly one-fifth of the grounded Antarctic Ice Sheet drains its ice through the Ross Ice Shelf (RIS) into the ocean. In this thesis, the longest and most precise record of radar measurements to date is used to evaluate basal melting and freezing along a traverse across the whole of the RIS. Together with satellite measurements, conclusions will be drawn on basal ice shelf processes of the largest Antarctic ice shelf, at locations that are largely inaccessible for direct measurements.

Mass loss of the Antarctic Ice Sheet has been observably accelerating, contributing to rising sea levels (Paolo et al., 2015; Rignot et al., 2019). Antarctica ice shelves cover an area of 1.5 million km^2 (Rignot et al., 2013), border 61% of the Antarctic coastline (Bindschadler et al., 2011), and transport 80% of the Antarctic ice mass (Jacobs et al., 1992). Basal melting is the highest proportion of mass loss from the ice sheet system, totalling 1516 ±106 Gt a-1 (Liu et al., 2015). Understanding ice shelf processes is therefore a requirement for predicting future ice sheet response to environmental changes.

Ice shelf mass loss does not directly impact sea-level rise as they are largely in hydrostatic equilibrium with the ocean. However, they provide backpressure against ice upstream, opposing the driving force of grounded ice flowing into the ocean (Dupont & Alley, 2005). A reduction in buttressing due to ice-shelf collapse or thinning causes wide-reaching acceleration and thinning of upstream glaciers (Dupont & Alley, 2005; Hulbe et al., 2008; Rack & Rott, 2004; Rignot et al., 2004; Rott et al., 2002). Regional or localised ice shelf thinning also reduces buttressing force and can impact grounded glaciers far from the affected region (Reese et al., 2018). The increased mass flux from grounded ice acceleration directly contributes to global sea-level rise (Rignot et al., 2004). Changes to ice shelf extent, volume and production of Ice shelf Water (ISW) have further implications for environmental

systems by changing ocean circulation patterns, sea ice and albedo, and ecosystem habitats (Hellmer, 2004).

The RIS is the largest ice shelf in the world with an area approximately the size of France (~500,000 km^2). With a total catchment area of over 2 million km^2 the RIS buttresses 11.6m of sea-level equivalent (SLE) (Tinto et al., 2019). The RIS is currently estimated to be close to a steady state with an ice shelf cavity sheltered from warming water masses (Depoorter et al., 2013; Moholdt et al., 2014). Borehole measurements through the ice shelf are expensive, rare and transient. Direct observations of the cavity have only been made at four sites across the interior RIS (Begeman et al., 2018; Jacobs et al., 1979; Stevens et al., 2020); Non-intrusive geophysical techniques can be used to survey sub-surface features such as internal layers, crevasses and the ice shelf base. Such ground-based measurements can cover a larger spatial extent but still require significant logistical support and interpretation of the medium's physical properties (Crary et al., 1962). Satellite observations provide large-scale long-term and ongoing measurements of ice-shelf changes. However, they are limited to surface measurements of glaciological features and require additional input data and assumptions (such as snow accumulation and steady state) when estimating basal mass balance (Moholdt et al., 2014; Neckel et al., 2012; Rignot et al., 2013). A lack of precise basal melting measurements over large areas restricts the ground validation of the spatial pattern and temporal variation of regional basal melting based on satellite data.

The British Antarctic Survey (BAS) developed the Autonomous Phase Sensitive Radio Echo Sounding (ApRES) to precisely measure changes of internal layers and basal reflections to millimetre precision in ice up to 2000m thick. Below the firn layer, ice thickness changes due to dynamic thinning and basal melting or freezing. Repeated ApRES surveys of the ice column allow the calculation of total thickness change and to separate vertical strain and basal melt rates (Brennan et al., 2014). Strain thinning rates can be derived from satellite velocity fields, but ground measurements of vertical strain are rare and will better constrain the wide scale estimates.

To this point, precise determination of basal melt rates from ground-based measurements across the RIS has focused on areas with high melt rates near the calving front and grounding lines; such measurements can be taken within a single summer period or within a year (Begeman et al., 2018; Marsh et al., 2016; Stewart et al., 2019). ApRES measurements of the central ice shelf region have not been undertaken yet due to logistical challenges, and the expectation of very low magnitude melt, making it difficult to determine change from short term measurements. Across the interior of the RIS, even low magnitude variations in basal mass balance are important for evaluating the mass balance of the RIS and changes to environmental processes as they potentially occur over such massive areas of the ice shelf.

1.1 Aims and Objectives

This research will evaluate spatial and temporal patterns of basal melting and strain deformation as indicators of long-term stability of the RIS. It will make use of multi-annual ApRES measurements along a 1000 kilometre transect spanning across the central Ross Ice Shelf from the Siple Coast grounding line in the southwest line to within 100km from the ice shelf front in the northwest. Improved understanding of basal processes and internal deformation in this area will allow evaluation of the basal mass balance of the RIS and its potential vulnerability.

This aim will be achieved by accomplishing the following objectives;

- Analyse ApRES waveforms from 32 locations acquired along the RIS SPOT and Siple Coast traverse between 2015 and 2020 in order to separate strain thinning from basal melting.
- Interpret ApRES basal and internal reflection characteristics and evaluate basal melting and shelf thickness at the 32 ApRES locations.
- Evaluate the spatial distribution of basal melting and freezing regimes in comparison with previous airborne data.
- Estimate wide-scale vertical strain rates across the RIS using satellite-derived velocity products for comparison with ApRES measurements.
- Draw conclusions about the representativity of satellite-based products and oceanographic models of the basal mass balance of the Ross Ice Shelf.

The work will contribute to the Aotearoa New Zealand Ross Ice shelf Program (NZRISP). The NZRISP seeks to broadly investigate Ross Ice Shelf and its many dimensions, including the effects of tides on the shelf, the stability of the shelf over geologic time using a hot-water drill, and the ice shelf's stability through GPS and radar.

2 Ice Shelf Principles

Ice shelves are dynamic bodies of ice being pushed out into the ocean by the driving force of the Antarctic Ice Sheets (Cuffey & Paterson, 2010). Ice becomes buoyant as it enters the ice shelf grounding zone and exits once it reaches hydrostatic equilibrium with the ocean. The ice shelf moves vertically with the tidal motion causing tidal flexure across the grounding zone between the grounded ice and the fully buoyant ice (Vaughan, 1995). The grounding zone and the ice shelf front create the boundaries that define the extent of the ice shelf. Ice flows from the grounding zone out to the open ocean at the calving front. Mass is lost through ice shelf wide basal melting and iceberg calving. The missing basal shear stresses from sea water allow ice shelves to spread across the ocean resulting in large areas of ice extension where it is unrestricted by lateral topography.

A stable ice shelf is in a state of dynamic equilibrium, with the long-term mass gain being equal to mass loss and a constant thickness profile and area. The system gains mass through glacier inflow, surface accumulation of snow, and marine ice accretion at the base from supercooled seawater. Ice shelves, and therefore the Antarctic Ice Sheet, loses mass mostly through basal melting and iceberg calving (Figure 1). The dynamic movement, combined with their remote location, makes precisely surveying individual mass change components challenging. Drilling through constantly deforming ice is difficult, and the equipment logistics are expensive, so access to the ice shelf cavity has only been achieved several times. This chapter describes the key glaciological processes linked to ice shelf dynamics and mass balance.

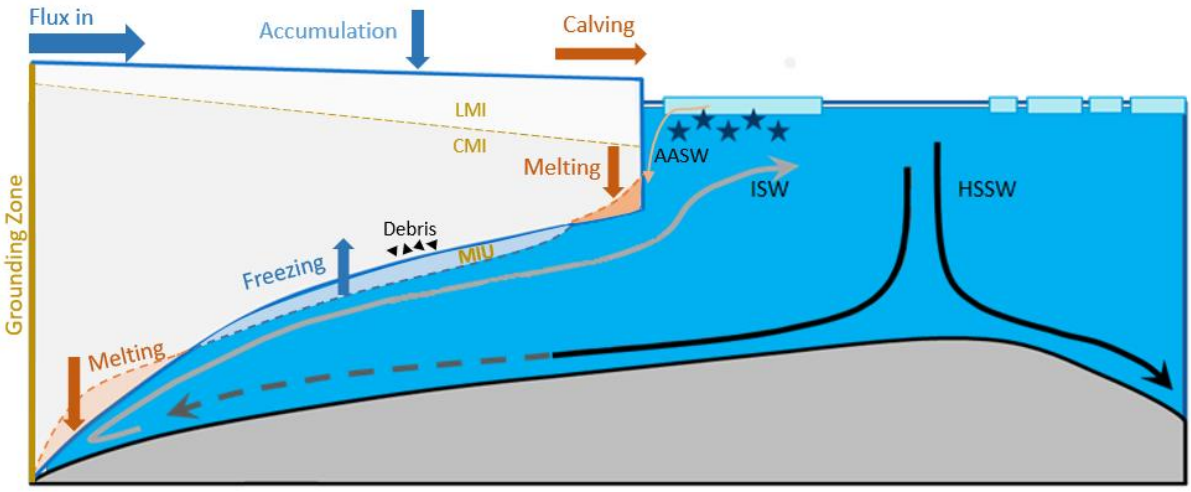

Figure 1. *A simple schematic of ice shelf mass balance fluxes and cold cavity circulation. LMI - Local Meteoric Ice, CMI - Continental Meteoric Ice, MIU – Marine Ice Unit HSSW – High Salinity Shelf Water, ISW – Ice Shelf Water, AASW – Antarctic Surface Water*

2.1 Ice Shelf Structure

Below the firn transition, ice structure and origin are used to interpret the ice shelf column processes. Ice is divided horizontally by the glacier or ice stream outlet, with bands of ice originating from the same outflow having a similar flow pathway across the ice sheet and ice shelf. Units can be divided vertically by their internal structure using geophysical methods (Das et al., 2020).

The local meteoric ice unit (LMI) is the upper unit of ice, originating from precipitation deposited on the flat ice shelf as horizontal layers parallel to the ice shelf surface. The planar layering is preserved with the compaction to firn and later ice (Kruetzmann et al., 2011). The changes in layer density and the parallel layers are well suited for RES measurements from the surface, perpendicular to these internal layers (Dowdeswell & Evans, 2004; Plewes & Hubbard, 2001).

The lower continental meteoric ice unit (CMI) contains ice originating from the continental ice sheets. CMI has been previously impacted by basal shear stresses and bed topography from glacier dynamics, resulting in a more complex, non-planar structure of internal layers less homogeneous than the LMI unit. Spatial variability is expected from different catchment areas and ice deformation histories. The interface between these two units has been identified in the wide-scale ROSETTA radar transects across the RIS (Das et al., 2020)

The structure of the ice shelf is dependent on ice deformation and ocean thermodynamics. Regions of melting have an abrupt boundary between the ice and ocean. Basal topography includes scalloping, terraces and channels formed from currents and eddies at the boundary (Dutrieux et al., 2014). Marine ice can form, rise, and accrete to the ice shelf's underside in regimes of basal freezing (Grosfeld et al., 1997). This marine ice unit (MIU) has been observed to be hundreds of metres thick below the Filchner-Ronne and Amery Ice Shelves (Craven et al., 2009; Oerter et al., 1992). Conversely, very thin MIUs have been found across the RIS, and peninsula ice shelves (Neal, 1979; Stevens et al., 2020). Pressure refreeze at the base of the grounded ice entrains debris within the lower layers of ice that persist onto the ice shelf until basal melting releases them (Stevens et al., 2020).

ISW generated at the grounding line rises following the ice shelf base's topography due to being less dense and saline than sea water. Where ISW rises above the pressure suppressed melting threshold, the water will become supercooled, start to form frazil ice, and freeze to the base of the ice shelf (Craven et al., 2009; Joughin & Padman, 2003; Joughin & Vaughan, 2004; Oerter et al., 1992). This creates a spatially variable MIU at the base of the ice shelf. Freezing processes include freezing directly to the ice shelf base and the buoyant rise of frazil ice and platelet ice to collect and compact the seawater interface (Langhorne et al., 2015).

2.2 Surface Mass Balance

Ice shelves gain mass at the surface through the accumulation of precipitation as snow. Considering the low precipitation rates across Antarctica, ice shelf accumulation is relatively high, receiving 20% of Antarctic precipitation over 11% of the total ice sheet and ice shelf area (Rignot et al., 2013). Spatial variability of surface mass balance across the ice sheet is caused by variable precipitation as well secondary processes of wind transportation and redistribution. The sparse surface accumulation measurements across the ice sheet require large interpolation areas, and different patterns of precipitation, redistribution and compacting snow make modelling spatial variability of snow accumulation challenging.

Freshly deposited snow has a density of 100-200 kg m^{-3}. Snow metamorphism rapidly increases density due to sublimation diffusion, wind transport, and sintering processes (van den Broeke, 2008). As the snow is buried, compaction from overburden pressures becomes the dominant cause of density change (Kruetzmann et al., 2011). Snow becomes classified as firn once it has persisted over a single summer period. Firn has a variable density increasing from 400 up to 830 kg m^{-3} at the firn-ice transition boundary, where air bubbles become sealed from each other. The glacial ice can continue to approach the maximum density of pure incompressible ice, 917 kg m^{-3} (Cuffey & Paterson, 2010). The depth and density of the Antarctic firn transition is spatially variable across the Antarctic Ice sheet, depending on temperature, precipitation and wind strength at the surface (Li & Zwally, 2004).

2.3 Basal Melting

Tides, winds, and density differences of water masses drive the ocean circulation in the cavity and transport heat into the cavity (Assmann et al., 2003; MacAyeal, 1984). Thermodynamic processes at the ice-water interface drive basal melting rates. Ice shelf basal melting occurs when seawater at the ice-ocean interface is above the pressure melting temperature, resulting in a net upwards heat flux. Three separate modes categorise basal melting processes, separated by distinct oceanic sources of heat transport to the ice shelf interface (Jacobs et al., 1992).

Mode 1 melting is caused by High Salinity Shelf Water (HSSW) intruding into the ice shelf cavity and driving melting at the grounding line. HSSW is formed during sea ice formation on continental shelves when brine rejection produces relatively dense, warm water that descends through the ocean column. Formed through sea ice freezing, HSSW is close to the ocean surface freezing temperature (-1.9 °C). The pressure-dependent freezing point decreases with depth by 0.76 C per 1000 m (Dinniman et al., 2016). The increased density of the HSSW causes the water mass to descend and follow the bathymetry to the grounding line and induces melting where the HSSW is above the pressure melting temperature (Tinto et al., 2019). The highest melt rates are at the deepest grounding lines, where HSSW will preferentially descend, and the pressure melting point is the most reduced (Marsh et al., 2016).

Mode 2 melting is generated when the relatively warm modified circumpolar deep water (mCDW, ~1 C) is able to access the continental shelf and the ice shelf cavity (Jacobs et al., 1992). Where mCDW reaches the ice interface, it produces rapid melting as it can reach temperatures of up to 4C warmer than the pressure melting point at the ice shelf base (Dinniman et al., 2016).

Mode 3 melting is observed when Antarctic Surface Water (AASW) intrudes under the ice shelf front. AASW has a consistent cold-core with temperatures similar to the surface freezing point, creating melt rates similar to *mode* 1 (Dinniman et al., 2016). Seasonal warming of the thin surface layer from atmospheric interactions can cause much higher melt rates where the cavity profile allows the water mass to intrude under the ice shelf (Arzeno et al., 2014; Horgan et al., 2011; Stewart et al., 2019).

The three modes are generated from large scale oceanographic and geographic processes, including the atmospheric conditions on sea ice formation patterns and ocean dynamics such as the accessibility of the continental shelf for the Antarctic Circumpolar Current (ACC) and CDW (Petty et al., 2013). Ocean circulation and cavity bathymetry control large scale patterns of basal melting while basal topography and surface roughness control small scale patterns. Subglacial hydrology under the grounded ice sheet and water outflow near the grounding line can also create localised zones of high melt rates (Marsh et al., 2016). Complex basal topography can cause small scale melting variability from preferential melting at the lower depths and freezing above the pressure melting temperature and crevasse or scalloping circulation patterns (Jordan et al., 2014).

Ice shelf cavities are categorised into cold and warm cavity ice shelves as a result of the dominant ocean processes (Petty et al., 2013). Cold cavity ice shelves are dominated by HSSW from sea ice production on the continental shelf or downwelling of AASW across the continental shelf, limiting the access of the warmer mCDW. Colder water masses result in low melt rates (0.1-1 m a^{-1}) for cold cavity ice shelves, including the largest, the RIS, the FRIS and the Amery. Cold cavity basal melting is dominated by mode 1 melting from higher sea ice production and mode 3 melting. Warm cavity ice shelves along the Amundsen and Bellingshausen Seas near the Antarctic Peninsula maintain high rates of mode 2 melting from mCDW intrusion (1-10ma^{-1}) (Dinniman et al., 2011).

2.4 Basal Freezing

Basal melting releases cold, fresh ice shelf water (ISW). The lower salinity and density cause ISW to buoyantly rise, following the topography of the ice shelf base. The cold water becomes supercooled once it reaches the pressure melting temperature, allowing frazil ice growth and basal accretion to the ice (Oerter et al., 1992). This basal freezing occurs across the central ice shelf from Mode 1 ISW and underneath sea ice from Mode 3 melt water

outflowing from the ice shelf cavity (Haas et al., 2021; Jenkins & Doake, 1991). Marine ice formation can offset proportions of basal melting mass loss by returning ice to the system. Marine ice accumulation and thickness varies spatially, as access to direct measurements is difficult must be determined by modelling, thickness changes and geophysics measurements.

2.5 Ice Shelf Dynamics

2.5.1 Strain Principles

For glaciology applications, the strain is a measure of ice deformation in response to stress acting upon the ice. Vertical strain thinning is the deformation component of ice shelf thickness change and must be well-constrained when determining small changes from basal melting. Satellite velocity, stake fields and measuring internal layer deformation have all been used to estimate strain thinning, but few studies have compared these methods over large extents. Strain is categorised as either: pure shear, where deformation is compressive (negative), extensive (positive), or shear (parallel deformation at varying rates, right lateral/left lateral) (Cuffey & Paterson, 2010). Ice strain deformation in one dimension (ε) is calculated by the length caused by the deformation relative to the initial length measured:

$$\varepsilon = \frac{L_f - L_i}{L_i} \tag{2.1}$$

Where L_i is the initial length, and L_f is the final length following ice deformation. Strain rates express the rate of ice deformation over time. The nominal strain rate ($\dot{\varepsilon}$) is, therefore:

$$\dot{\varepsilon} = \frac{\delta L \,/\, L_0}{\delta t} \tag{2.2}$$

Where δL is the change in length, L_0 is the undeformed length, and δt is the time taken for deformation to occur. Logarithmic strain expresses positive and negative proportional strain rates to evaluated using the same scale. Logarithmic strain rates have the same strain value with an inverse sign, where the nominal strain rate would be -0.5 and 1.

$$\dot{\epsilon} = \frac{1}{\Delta t} \ln\left(\frac{L_f}{L_0}\right)$$

At low strain rates, logarithmic strain rates will be very similar to the nominal strain. Differences between the two methods only become significant at high strain rates (Alley et al., 2018).

Stresses and resulting strains occur in each of the mediums three dimensions. The variation of strain deformation across ice shelves is dependent on the coastal geometry and ice flux across the grounding line. Ice shelf flow dictates where regions of ice convergence and divergence occur, either transverse or longitudinal directions. Areas of net horizontal ice convergence result in ice column thickening, while net horizontal ice divergence regions will result in ice-shelf thinning. As there is no friction from a bed, there is no basal shear stress acting on floating ice, and so depth dependant shear strain is not present. The differential velocity of adjacent ice flow, such as those near the edges of the high-velocity ice streams, glacier outlets or grounded ice, still results in horizontal shear strains.

Pure ice is incompressible, and so by disregarding compressive firn layers, it is assumed the strain of the three dimensions must sum to zero to obey the conservation of mass (Hooke, 2019). Where ε_{xx}, ε_{yy} and ε_{zz} are the normal strain rates in the x, y and z dimensions, respectively (Hooke, 2019).

$$\dot{\varepsilon}_{xx} + \dot{\varepsilon}_{yy} + \dot{\varepsilon}_{zz} = 0 \tag{2.3}$$

In situations where only two dimensions of strain can be measured, the third can be determined by the residual of the other two strains given mass is constant and fracturing or crevassing does not occur. This relationship can determine vertical strain rates when only the two horizontal axes are known. Surveys of stake grids can measure horizontal strain deformation of ice shelves. Satellite velocity derived strain fields uses the same principle, measuring position changes (speed and direction) across a much wider region and without having to deploy physical stakes grids.

2.5.2 Structural Dynamics

Ice shelves receive minimal basal friction from the ocean and so are unrestricted by basal topography to spread through gravity-driven spreading. Multiple glaciers and ice streams flowing out into the ocean can converge to combine into a large ice shelf. Suture zones originate from the convergence of two separate ice flows, resulting in positive vertical strain (Jansen et al., 2013). The thin ice thickness of suture zones facilitates basal freezing by being above the pressure melting point for ISW, causing marine ice melange to bond to the convergence base. Suture zones have been recognised as regions of weakness that pool meltwater and facilitate the ice shelf collapse (Kulessa et al., 2019).

Flux variations from input streams influence the dynamics, flow, and strain of the entire ice shelf, with temporal variations in grounding line flux that leave a lasting impact on the ice shelf's flow structure. Streak lines along the ice shelf show remnant terrestrial ice topography paths from the grounding line. Past variations in ice stream flux are apparent

where streak lines are not parallel to the current flow direction of the ice shelf (Hulbe & Fahnestock, 2007).

Ice rises and ice rumples occur where an ice shelf is grounded on elevated bathymetry. These features are expressed by an increase in surface elevation bordered by freely floating ice and a surrounding zone of tidal flexure (Vaughan, 1995). Ice rises are categorised by stagnant grounded ice (Matsuoka et al., 2015), while ice rumples only impede ice flow without causing complete stagnation. Zones of ephemeral grounding from tidal cycles are not considered ice rumples as they exert little buttressing force on the ice shelf (Schmeltz et al., 2001). These grounding features cause strain thickening upstream, where ice is forced against the grounded ice and downstream where ice reconverges to fill in the 'low pressure' zone (Alley et al., 2018).

2.6 Thickness Change

To determine basal melt rate rates ($\dot{M}_b$) as a component of the total thickness (H) of a moving ice column (Lagrangian frame of reference), all other components of thickness change must be taken into account. These include: surface accumulation rate ($\dot{M}_s$), firn compaction rate ($\dot{f}$) and the vertical strain rate ($\dot{\epsilon}_z$) multiplied across the ice thickness (H) to determine the total strain thickness change. Therefore, the ice thickness rate of change with respect to time is calculated using:

$$\frac{dH}{dt} = \dot{M}_s - \dot{M}_b - H\dot{\epsilon}_z - \dot{f} \tag{2.1}$$

Remote sensing approaches can only measure the ice shelf surface and so must account for accumulation and firn compaction rates when analysing thickness and freeboard changes. By co-registering geophysical measurements at the firn-ice transition boundary, the surface thickness changes can be excluded, leaving strain and basal mass change. The vertical strain rate of the ice column is directly measured from the relative movement of internal layers, and when applied over the ice column thickness, the remaining component of thickness change is from basal melting.

3 Ross Ice Shelf Study Area

This chapter introduces the Ross Ice Shelf study area and describes the local geography, glaciological, and cavity bathymetry relevant to interpreting the ApRES dataset, basal melting processes, current state of knowledge and the scope of the research.

3.1 Location

Located in the Ross Sea Embayment between the East and West Antarctic ice sheets (EAIS and WAIS), the Ross Ice Shelf (RIS) is the largest ice shelf in the world by area, covering approximately 500,000 km^2 (Rignot et al., 2013). The RIS is bordered to the south and west by the Transantarctic Mountains, damming the polar plateau of the EAIS behind them. The lower altitude Mary-Byrd land is situated to the east of the RIS and the open Ross Sea to the north (Figure 2). Broad ice streams transport ice from the WAIS, while narrow and steep valley glaciers transport ice from the EAIS through the Transantarctic Mountains. Iceberg calving occurs along the ice shelf front at the boundary with the Ross Sea. The largest outflows of ice entering the RIS are from the WAIS's four major ice streams and the large valley glaciers from the EAIS.

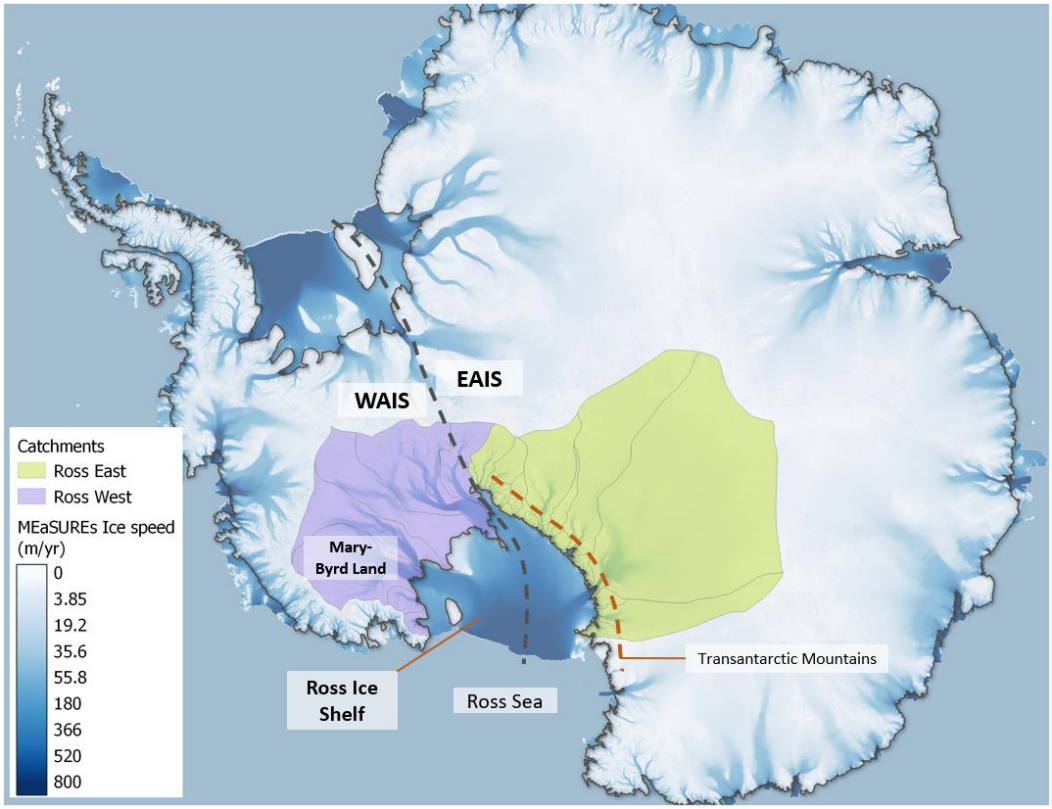

Figure 2. *Map of the Antarctic Ice Sheet and RIS catchment area. The division between the West Antarctic Ice Sheet (WAIS) and East Antarctic Ice Sheet (EAIS) (grey dashed line), with the catchment boundaries and ice velocity displayed as the base map.*

The majority of the RIS area has an ice thickness of 300-500 meters. This can increase to maximums of 700-1000 meters at the grounding lines and minimums of 150-250 meters at the calving front (Figure 3). Ice velocity increases as the ice moves from the grounding line towards the calving front, where the velocities reach 800m a^{-1} (Figure 4) (Rignot et al., 2011). The residence time of ice from the grounding line to the calving front depends on the source and flow path but are generally around 1000 years (Mouginot et al., 2017). Some areas close to stagnation are found near the stagnant Kamb Ice Stream and upstream of Steershead Ice Rise pinning points.

3.2 Glaciological Setting

The RIS's position with large catchments in both the West and East Antarctic Ice Sheets results in a glaciological setting of two distinct origins of ice converging into the Ross Embayment. The differences in ice origins and tectonic driven cavity differences result in the common division into the Ross East and Ross West. The Crary ice Rise (CIR) and associated downstream suture zone are considered roughly the point of division between the two ice sheet catchments.

The western RIS is feed by 56.1 ± 4 Gt/year of ice transported across the grounding line from the EAIS, with a catchment area of 1,500,000 km^2 (Rignot et al., 2013). Ice transport from the EAIS is by topographically constrained outlet glaciers cutting through the Transantarctic Mountains. The Byrd catchment is the largest by area, but the Skelton, Shackleton and Scott also cover significant areas. Across the entire RIS basal melt rates and surface accumulation rates are approximately equal, with an ice shelf average rate of 0.1 - 0.3 ma^{-1} water equivalent (Agosta et al., 2019; Rignot et al., 2013).

The smaller WAIS is a marine ice sheet with a considerable proportion of ice grounded below sea level. Studies are ongoing about its stability in a changing climate and ocean system (Bindschadler, 2006), with a potential global sea-level rise of 5 to 6 meters stored in the ice sheet (Alley & Bindschadler, 2001). The WAIS contributes 73.0 ± 4 Gt/year of ice to the RIS through several large ice streams (named A-F or Bindschadler, Whillans, Kamb, MacAyeal, Echelmeyer) from a catchment area of 800,000 km^2 (Rignot et al., 2013), equalling approximately 40% of total WAIS ice discharge (Price et al., 2001). The WAIS contributes slightly more ice to the RIS's area, covering 60% of the ice shelf.

Streak lines across the RIS are visible in satellite imagery and show the historic flow path of ice from the grounding zone to the calving front (Hulbe & Fahnestock, 2007; Hulbe et al., 2013). These streak lines match the modern ice flow direction for much of the ice originating from the EAIS glaciers. However, some areas show very different modern flow direction to the streak lines of ice emanating from the West Antarctic Ice Streams (Hulbe et al., 2013). This variation is indicative of a history of variable flux from the WAIS ice stream outlets impacting the dynamics of the ice shelf (Hulbe & Fahnestock, 2007). Most notably, the Kamb Ice Stream is estimated to have stagnated 150-160 years ago (Hulbe et al., 2013;

Retzlaff & Bentley, 1993). Ice shelf velocities downstream from the ice stream grounding line are in the order of 1-5m per year.

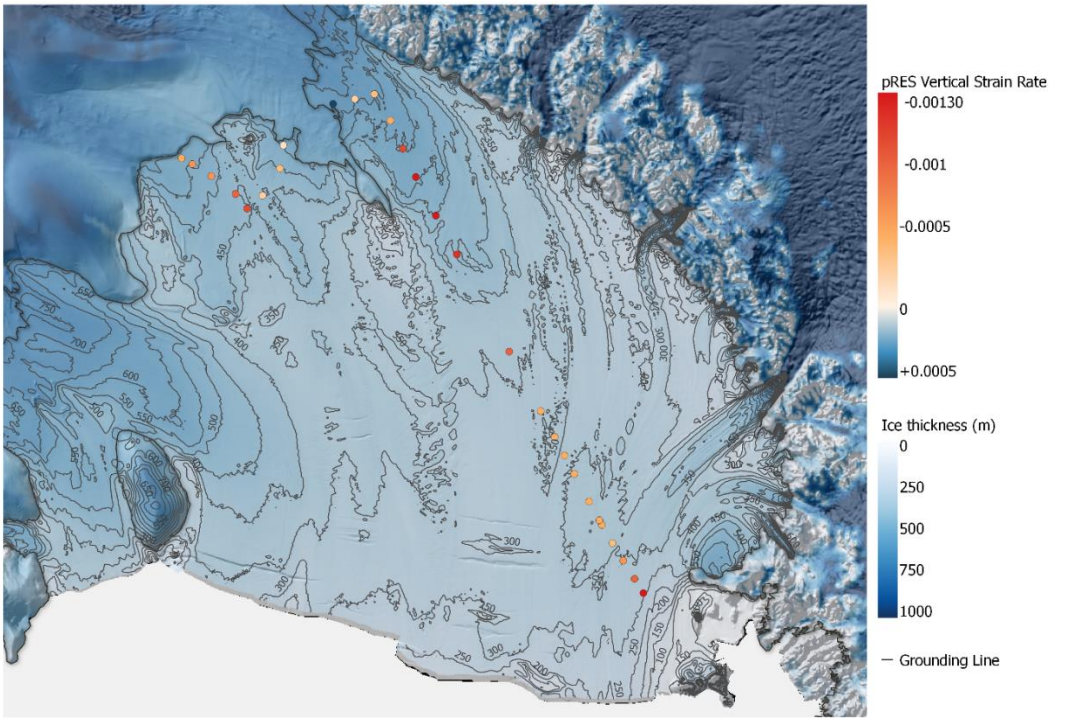

Figure 3. *BEDMAP2 Ice thickness across the RIS (Fretwell et al., 2013).*

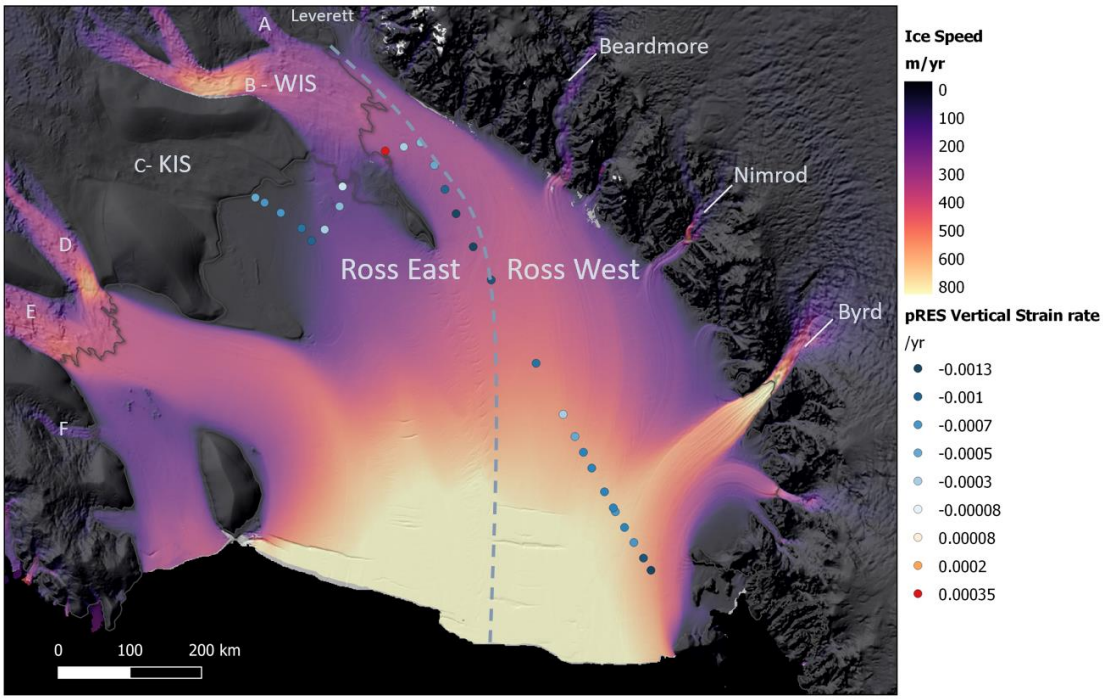

Figure 4. *MEaSUREs Ice Shelf Velocity across the RIS. The Ross Ice Shelf and the division between Ross East and Ross West are labelled.*

The CIR and Roosevelt Island are the two major ice rises present on the RIS. CIR is a prominent, linear ice rise extending out in the middle of the Whillans Ice Stream (WIS) outflow on the Siple Coast. It is not an isolated grounded area surrounded by ocean cavity, but a protrusion of the grounding line, with grounded ice from WIS diverging around the CIR to reconverge downstream. Cooling trends derived from two boreholes across the CIR estimate the site to have become grounded 1.1k - 580 years ago (Bindschadler et al., 1990), not an older remnant of grounded ice from a previous extent of the ice sheet. Several small unnamed ice rumples are present in the Siple Coast region as isolated pinning points in the very shallow cavity (Matsuoka et al., 2015; Moholdt & Matsuoka, 2015).

3.3 Ice Shelf Cavity and Oceanic Processes

The RIS cavity is the southernmost section of the Ross Sea and one of the least explored oceans. Very few direct oceanographic observations of the RIS cavity exist, with only three transient borehole measurements of the central cavity, two of them in the last few years (Stevens et al., 2020). Oceanographic data collected along the calving front remains the most extensive available dataset for modelling and understanding cavity processes (Grosfeld et al., 1997; Hellmer & Jacobs, 1995).

Estimates of the cavity bathymetry are challenging to constrain as direct measurements are expensive, and geophysical measurements must be made through both ice and seawater. Gravity and seismic surveys continue to improve the resolution of the cavity bathymetry (Tinto et al., 2019). The most extensive dataset of cavity bathymetry come from (Timmermann et al., 2010) featured in the BEDMAP2 dataset. The poor constraint of bathymetry is most impactful where ice shelf thickness and bathymetry falsely identified grounded regions. In this instance, the thickness between the known grounding line and 100m cavity depth is interpolated (Timmermann et al., 2010).

The cavity is separated roughly along the centre into two distinct tectonic regions, distinguished by bathymetry and magnetic anomalies and closely aligned with the glaciological boundary between the East and West RIS. Bathymetry beneath the ice shelf is generally deeper beneath the western RIS (EAIS side) with a mean depth of 670m and shallower beneath the East RIS (WAIS side) with a mean depth of 560m (Tinto et al., 2019). This bathymetry influences the cavity depth, resulting in deeper cavity thickness beneath the western RIS and shallower thicknesses beneath the eastern RIS

Figure 5) Through improvements to the sub-ice shelf bathymetry resolution, models of ocean mass intrusion into the RIS cavity revealed HSSW intrusion is mostly confined to the West RIS, most AASW intrusion is around Ross Island and mCDW only has minor intrusion to the east (Tinto et al., 2019). The tidal cycle under the eastern Ross Ice Shelf is diurnal and can exceed 2 m in some locations (Padman et al., 2018).

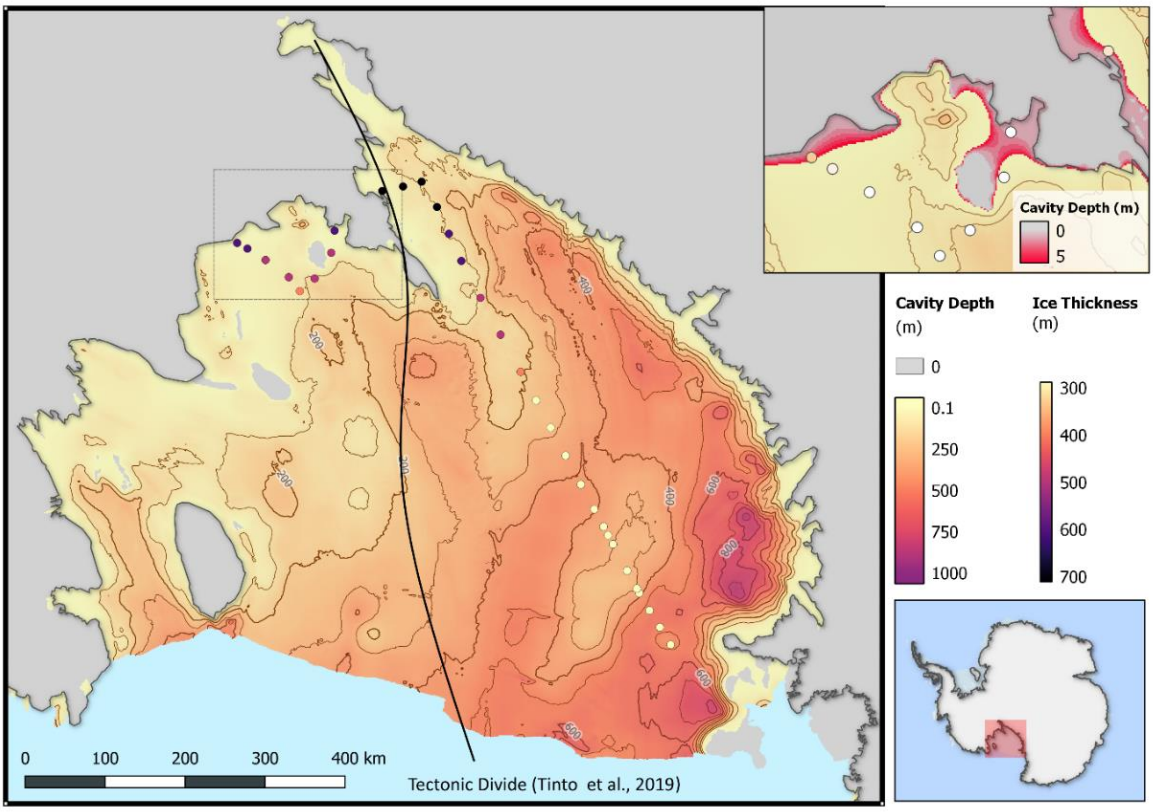

Figure 5. *Cavity depth of the RIS from BEDMAP2. ApRES measurement sites are displayed with BEDMAP2 ice thickness. Note the isolated grey ice rumples present in the Siple Coast region. Inset view of the Siple Coast highlights regions with interpolated cavity depth less than 5m.*

3.4 Ice-Ocean Interactions

The RIS has long been a focus of scientific research due to its importance to the Antarctic Ice Sheet and the global climate system. Detailed investigation began in the International Geophysical Year (IGY) in 1957-58 when the RIS was circumnavigated and surveyed with elevation, seismic gravity, magnetic and radar surveys (Crary et al., 1962). The first ice core drilling on the RIS occurred at Little America Camp, <3km from the ice shelf front near the Bay of Whales (Ragle et al., 1964). The survey informed the first interior cavity measurements during December 1977, 450km south of the calving front at site J9. A thin layer of fresher water was present just below the ice shelf base with a warmer water mass at greater depths indicated melting (Clough & Hansen, 1979) while thermodynamic flux measurements determined basal freezing (Zotikov et al., 1980).

The second direct measurement of the RIS interior cavity after J9 was hot water drill site 2 (HWD-2) as a part of the Aotearoa New Zealand Ross Ice Shelf Project (ANZRISP). During December 2017, oceanographic, benthic and glaciological measurements were taken through the 25cm wide HWD-2 borehole, including video (Stevens et al., 2020). The

borehole revealed a layer of bubble poor, sediment-rich ice originating from the entrainment of sediment at the base of the Liv Glacier. This layer was approximately 70m thick and extended to the basal interface. At the ice-ocean interface, video imagery revealed a 0.1m layer of ice crystals frozen to the ice shelf base from basal freezing. However, oceanographic measurements revealed water temperatures from 0-8 mK above the in situ melting temperature resulting in an estimated basal melt rate of 0 - 0.09my^{-1}, indicating a cycle of ephemeral freezing and melting. Water sampling and ongoing oceanographic measurements were made over nine days, after which a long-term mooring containing CTD instruments and current meters was deployed. Satellite altimetry, radar and seismic surveys supported the borehole measurements.

Over the 2018 Antarctic season, the ANZRISP continued fieldwork at the Siple Coast with borehole and geophysical surveys at the HWD-1 site downstream from the Kamb Ice Stream. Direct measurements of HWD-1 borehole pressure recorded an ice thickness of 582.5 m (Huw Horgan, personal correspondence*).*

Satellite measurements of ice shelf altimetry and velocity have enabled wide-scale studies of basal mass balance across the entire Antarctica ice shelf extent, including the RIS. The cold cavity RIS has basal mass balance close to zero across much of its area (Moholdt et al., 2014). Higher melt rates were identified at the grounding line of major outflows and near the Ross Island calving front, but most of the interior has very low magnitudes of melting or freezing relative to other ice shelves (Adusumilli et al., 2020; Rignot et al., 2013).

A non-linear increase of basal melt rates as the calving front across the RIS calving front was determined from ICESAT laser altimetry measurements, up to a maximum of 2.8 ± 1.0 m a^{-1} within 1km of the calving front (Horgan et al., 2011). A constant strain rate field of 0.001 a^{-1} was utilised to determine the strain thickness change. Sixteen km^3 a^{-1} of melt was estimated to be produced within 40km of the calving front.

The RIS maintains much lower basal melt rates relative to smaller ice shelves. In the eastern RIS (WAIS side), mass loss is dominated by calving, with very little net basal mass loss (Rignot et al., 2013). The mass loss of the western RIS (EAIS side) was equally shared by calving and basal melting processes. The results confirmed elevated basal melting rates at the grounding lines and calving fronts, with low basal melting and freezing rates across the central region.

3.4.1 ApRES Surveys

Previous Autonomous Phase-sensitive Radio Echo Sounding (ApRES) surveys on the RIS has been limited to specific, localised high melt rate areas. The four main studies have measured basal melt and strain rates at the calving front (Stewart et al., 2019), near the Whillans grounding line (Begeman et al., 2018; Marsh et al., 2016) and near the grounding line (Huw Horgan, personal correspondence).

Basal melting near the calving front adjacent to the Ross Island and extending inland to Mina Bluff was surveyed by (Stewart et al., 2019). These increased melting rates were linked to the inflow of solar-heated water from the Ross Sea Polynya. Summer melting rates of up to 7 ma^{-1} were found at the edge of the calving front. Basal melt rate exponentially decreased with distance from the ice shelf front with melt rates of 1 ma^{-1} present near White Island.

Marsh et al. (Marsh et al., 2016) used ApRES to survey surface expressions of basal channels 1.7km seaward of the WIS grounding line. The highest ApRES measured melt rates are 16-22 ma^{-1} at the upstream formation of the channel. This was related to the hydrological outflow of subglacial lakes from beneath the WIS along distinct sub-glacial channels. These melt rates decreased as the established depression progressed downstream and returned to baseline melt rates.

ApRES surveys of deep grounding line basal melt rates have been undertaken at the KIS and WIS in association with sub-ice cavity borehole measurements at HWD-1 and WISSARD (Begeman et al., 2018). These studies produced opposite trends in the spatial variation of basal melting with distance from the grounding zone. At KIS, the summer melt rates of 2.0 ma^{-1} decreased with distance from the grounding zone to 0.2 ma^{-1} 10 kilometres downstream *(*H. Horgan, personal communication*)*. Located within a narrow embayment, the WISSARD location saw summer basal melt increase 0.02 ma^{-1} near the grounding line to 0.12 ma^{-1} downstream over similar distances (Begeman et al., 2018).

3.5 Field Sites and Rationale

The traverse ApRES sites consist of 32 flagged locations along the 1000km SPOT and SCT routes (Figure 6). The SCT sites P1 to P6 are aligned perpendicular to flow across the active WIS separated by the CIR. One measurement was taken on grounded ice upstream of the CIR. Site P3 to P5 are situated in complex deformation areas adjacent to the grounding zones upstream of the CIR and ice rumples. Sites P7 to 11 are arranged parallel to flow downstream from the KIS, approaching within 11km of the grounding line at P11. Current estimates for site velocity, ice thickness, elevation and cavity depth are shown in Table 1. Summer ApRES surveys have been undertaken to the south of P11 and to the north of T1, measuring the mode 1 melting at the grounding line and mode 3 melting at the calving front (Stewart et al., 2019) (H. Horgan, pers. comm.). This survey is designed to measure the gaps in high precision measurements across the central RIS from the grounding line to the calving front. Low expected melt rates across the central RIS informed the annual remeasurement times, allowing small rates of change to become measurable.

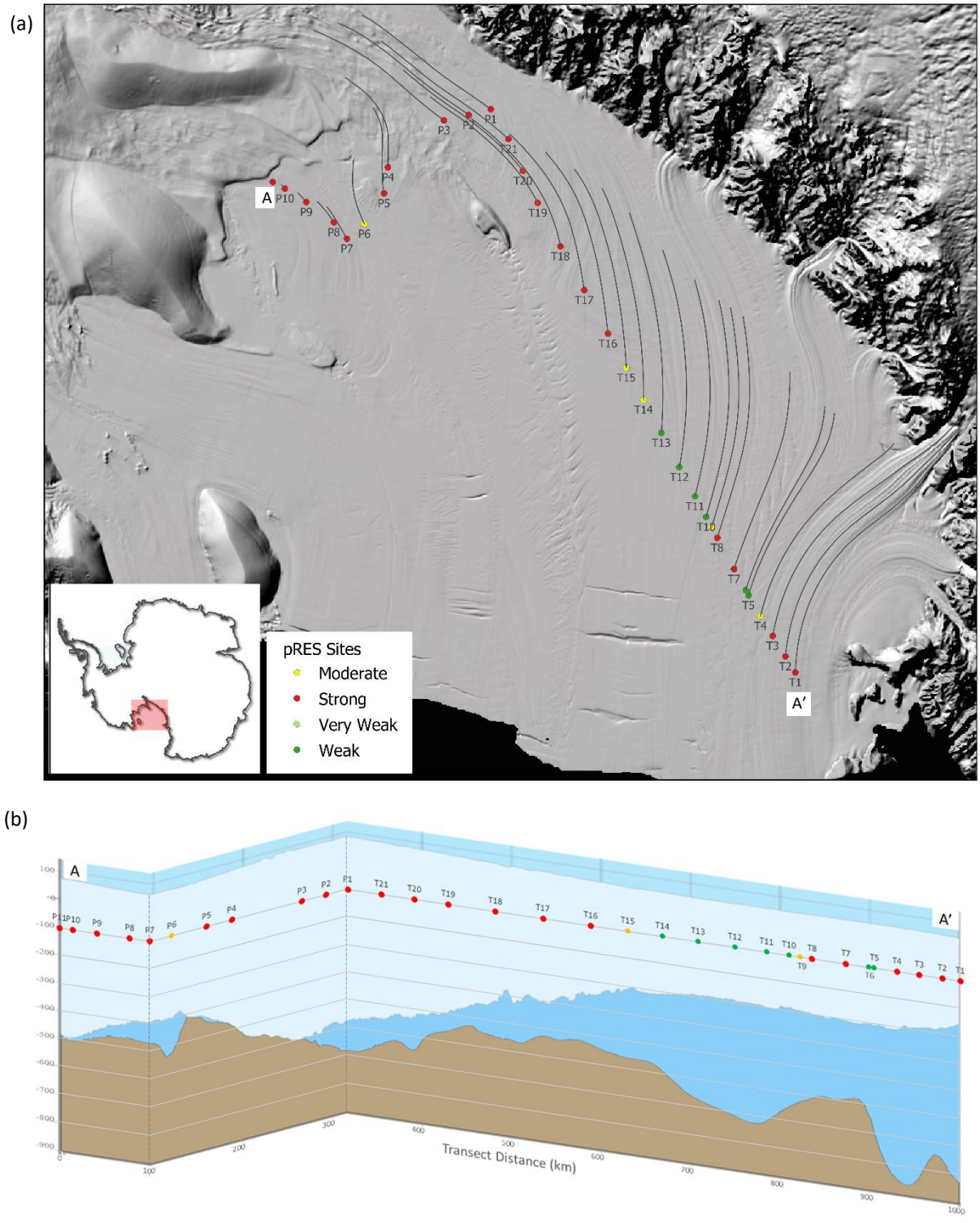

Figure 6. *ApRES site locations of this study in (a) map view and (b) BEDMAP2 cross section. T1-21 along the SPOT and P1-11 along the SCT. REMA elevation map clearly displays the surface features and streak lines across the RIS. Flow paths indicate 500 years backwards trajectory across the modern velocity field.*

Table 1. *Glaciological interpolations at each 2019 field site position from the MEaSUREs and BEDMAP2 datasets.*

Site	MEaSUREs Ice Velocity (m a^{-1})	BEDMAP2 Surface elevation (m)	Bed Elevation (m)	Ice Thickness (m)	Cavity Thickness (m)
Ross East					
T1	622	49	-825	308	566
T2	655	52	-747	331	468
T3	696	53	-835	346	542
T4	735	55	-841	366	530
T5	737	54	-671	361	364
T6	730	54	-624	358	320
T7	709	54	-588	360	282
T8	668	53	-604	353	304
T9	651	53	-623	348	328
T10	638	52	-648	343	357
T11	617	53	-709	354	408
T12	598	52	-705	345	412
T13	567	52	-666	348	370
Ross West					
T14	537	54	-581	366	269
T15	501	54	-556	365	245
T16	470	58	-527	406	179
T17	430	64	-523	462	125
T18	386	68	-553	492	129
T19	333	75	-555	566	64
T20	325	79	-642	603	118
T21	337	83	-639	631	91
P1	346	86	-680	658	108
P2	341	85	-641	662	64
P3	330	86	-597	679	4
System_Test	180	78	-519	597	0
P4	171	73	-483	555	1
P5	168	67	-446	497	16
P6	169	63	-518	460	121
P7	106	63	-469	456	76
P8	73	64	-462	468	58
P9	31	69	-476	516	29
P10	13	74	-500	562	12
P11	6	73	-487	555	5

The SPOT sites T1 to T21 are all arranged linearly along the SPOT ice road covering the majority of ice paths from the EAIS. To the north, T1 begins on the edge of the Byrd outflow and continues south to the Siple Coast turn off at P1. Ice velocity begins transverse to the traverse but shifts to be approximately parallel to the south. The SPOT sites cover most central sites furthest from the grounding lines.

The marked sites move with the ice shelf flow, and repeat measurements survey the same ice column. Using this lagrangian reference frame, the global coordinates of the measurement will continue to move downstream each year. The highest velocities over 730 ma^{-1} were seen at sites T4-T6 on the margins of the Byrd outflow, decreasing as the traverse travels south to a 330 ma^{-1} at P3. Lower velocities were present at the Siple Coast sites, decreasing from 171 ma^{-1} to 6 ma^{-1} as the sites approached the KIS grounding line (Rignot et al., 2017). The 500 year back trajectory of ice using modern flow vectors reveals increasing displacement at northern sites (Figure 6). This interpretation does not account for past flux variations south of T14 but displays the current state of the ice shelf dynamics upstream of sites. The traverse covers ice originating from the Transantarctic Mountains from Byrd to Leverett catchments and two significant ice streams from the WAIS, the KIS and WIS.

4 Methods

4.1 Radio Echo Sounding Using Phase-Sensitive Radar

Radio-echo sounding (RES) is a geophysical technique which is used since the 1960s to observe the thickness, basal topography and internal layers of glaciers and ice sheets (Robin et al., 1969; Schroeder et al., 2020). The transparent nature of ice and snow to Very High-Frequency radio (VFH) (30-300MHZ) and Ultra-High frequency radio waves (UHF, 300-1000MHz) allows electromagnetic (EM) radio waves to pass through the medium virtually unimpeded (Waite & Schmidt, 1962). Higher frequencies have a higher resolution but lower penetration depths within the ice. The EM frequency (f) and velocity within the medium (v) determine the corresponding wavelength (λ).

$$\lambda = \frac{v}{f} \tag{4.1}$$

The behaviour of EM radiation at a given frequency depends on the dielectric properties of the medium, in particular, the relative electrical permittivity (ε_r) and the electrical conductivity (σ) (Jol, 2008). Dielectric properties of common earth materials are shown in Table 2. Electrical permittivity (F m^{-1}) is a medium's capacity to store an electrical charge and impede the flow of an electric current or electromagnetic radiation propagation. The electrical permittivity of a medium is defined relative to free space (8.854 x 10^{-12} Fm^{-1}) as the relative permittivity (ε_r) or the dielectric constant (Plewes & Hubbard, 2001). The presence of liquid water, salts and impurities such as entrained volcanic ash layers can alter the relative permittivity of pure ice. Electrical permittivity is also sensitive to material properties such as crystal orientation and, to a small extent, temperature and pressure (Boned et al., 1979; Johari & Charette, 1979). For snow with density ρ (in kg m^{-3}), the relative dielectric permittivity is a mixture of air and pure ice (Table 2), which can be approximated by (Kovacs et al., 1995):

$$\varepsilon_r'(\rho) = (1 + 0.000845 \cdot \rho)^2 \tag{4.2}$$

The velocity (v) of electromagnetic waves is dependent on the dielectric permittivity of the medium the wave is passing through and the speed of light in a vacuum (c). The ε_r of pure ice (3.15) results in a propagation velocity of 0.169 m ns^{-1}. For freshly deposited snow with a density of 350 kg m^{-3} due to higher air content, ε_r is 1.3 with a velocity of 0.23 m ns^{-1}.

$$v = \frac{c}{\sqrt{(\varepsilon_r)}} \tag{4.3}$$

Electrical conductivity (mS m^{-1}) is the ability of a medium to conduct an electrical current. While the conductivity of ice has some dependence on pressure and temperature, it is primarily a function of ion or impurity concentration (Fujita & Mae, 1993). High conductivity causes increased attenuation of electromagnetic waves and signal loss. Radio waves travel through pure ice very effectively due to the low conductivity, and echo sounding can be accomplished to depths upwards of 3-4 km (Jol, 2008). The high conductivity of seawater and marine ice attenuates VHF radio waves and presents a barrier for radar.

Table 2. *Typical electrical properties of common environmental mediums.*

Material	**Relative permittivity** εr	**Conductivity σ** (mS/m)	**Velocity v** (m/ns)	**Attenuation** α (dB/m)
Air	1	0	0.3	0
Pure ice	3.15	0.01	0.169	0.01
Snow (350 kg m^{-3})	1.3	<0.01	0.23	<0.01
Snow (600 kg m^{-3})	2.27	<0.01	1.99	<0.01
Distilled Water	80	0.01	0.033	0.002
Fresh water	80	0.5	0.033	0.1
Sea water	80	$3x10^3$	0.01	10^3
Dry Sand	3–5	0.01	0.15	0.01
Saturated Sand	20–30	0.1–1.0	0.06	0.03–0.3
Silt	5–30	1–100	0.07	1–100
Clay	5–40	2–1000	0.06	1–300
Granite	4–6	0.01–1	0.13	0.01–1

Source: Plewes *and Hubbard (2001)*

Where variations in dielectric properties occur between layers within the ice, some radar energy is reflected towards the surface to be measured by the RES receiver. The amount of energy reflected at the interface is dependent on the relative contrast in dielectric properties between two media. The remaining energy passes through the boundary and continues propagating downwards. The reflection coefficient is the power ratio between the incident and the reflected signal. The reflection coefficient is approximately -2dB for the ice shelf base reflection, while internal layers are much lower within -60 to -90 dB (Brennan et al., 2014). For comparison, an ice-bedrock interface has a reflection coefficient of -10 to -25 dB, with the variance caused by the minerals present at the interface (Dowdeswell & Evans,

2004). Scattered englacial debris within ice produces backscattering and radar clutter, limiting the penetration of the signal (Smith & Evans, 1972) and creating stronger reflections within these layers (Hodson et al., 1997). Basal layers of highly conductive marine ice create low signal reflections due to the opaque, high attenuation medium. The diffusion of ion concentration within the marine ice and the brine ejection during formation creates a weaker dielectric contrast and reflection signal than the ice-ocean interface.

Without major shear stresses on the ice shelf, horizontal deposition and stratigraphy of snow in layers is maintained throughout burial and the transition to ice. Parallel stratigraphy is optimal for the RES analysis of nadir structures and requires less complex interpretations and surveys to determine common midpoints. Englacial layers observed in RES are the result of volcanic deposits changing acidity (Legrand & Mayewski, 1997), ice fabric layers (Fujita et al., 2000), dust (e.g. tephra) or entrained morainal or basal debris. Density changes through melt or refreezing snow metamorphosis and mechanical settling within firn and snow layers dominate the cause of internal reflections measured by RES (Kruetzmann et al., 2011; van den Broeke, 2008).

The measured two-way-travel time (TWT) of the radar signal between the transmitter and reflector can be converted to the range R (depth) (Figure 7) by using the radar wave velocity v in the following equation:

$$R = \left(\frac{TWT}{2}\right) v \tag{4.4}$$

Variable velocities in firn and ice must be taken into account to obtain the true depth of a reflector. By maintaining the lower velocity of pure ice will underestimate the ice column thickness. Equation 4.4 assumes that the distance between transmitter and reflector is much smaller than the reflector depth or known and corrected.

Using this method and assuming internal layers parallel to the surface, reflection points are expected to be centred directly between the two radar antennas. Several assumptions are made with this understanding of GPR methods to interpret layer range. The radar wave paths to and from the reflection are assumed to be isotropic, maintain the same velocity and propagation in both travel directions.

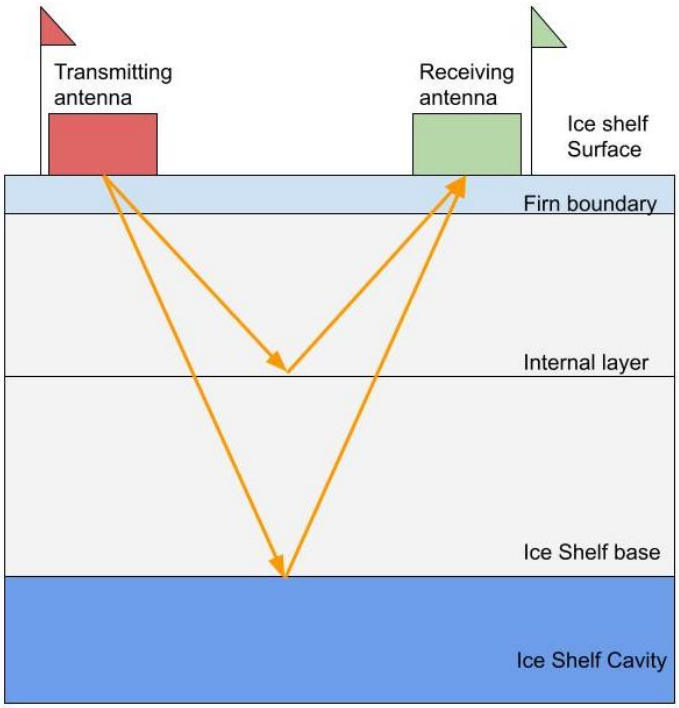

Figure 7. *Schematic of the ApRES field set-up. Including the radar transmitter, receiver, and the radio waves pathway between them, reflecting from internal layers and the ice shelf base at a centre-point.*

4.1.1 ApRES Principles

Description of the PRES system and development

The British Antarctic Survey (BAS) developed a frequency modulating continuous waveform (FMCW), phase-sensitive radio-echo sounder (pRES) to measure the ice shelf structure and basal reflection to the precision required to calculate the vertical strain and basal melting with repeat measurements (Corr et al., 2002). The upgraded autonomous phase-sensitive radio-echo sounding (ApRES) model featured much lower power consumption and components rated for -40C conditions, making it suitable to deploy for long periods over the polar winter. This enabled autonomous data collection when left in the field, collecting multiple measurements per day. The newer system was also more compact, allowing for easier transportation and operation during field campaigns (Brennan et al., 2014). ApRES has been used in both the Antarctic and Greenland ice sheets since its development to measure ice thickness, vertical strain rates (Kingslake et al., 2014), tidal flexure (Jenkins et al., 2006), basal melt rates (Brennan et al., 2014) and ice fabric (Jordan et al., 2020). These techniques have been applied to ice shelves, grounded ice sheets, ice streams, ice rises and remote polar glaciers. ApRES has the potential to be a valuable tool for mountain glacier research. However, it is currently difficult to gain approval for use in more populated regions than the poles due to the system's large bandwidth and potential interference with critical frequencies.

The ApRES instrument transmits at a nominally constant amplitude with a nominal power of 100mW or 20dBm. Each transmitted chirp from the radar features a linear ramping frequency increase from 200 to 400 MHz over 1 second. The received signal is processed first through an amplifier, an adjustable attenuator, another amplifier, then frequency deramped by mixing with the currently transmitting signal. An active filter enhances the amplitude through the given gain settings before being digitised and saved to the system files. The analog to digital converter (ADC) has a voltage range of 0-2.5V. Table 3 lists the ApRES instrument specifications.

Table 3. A*PRES specifications (Brennan et al. 2014)*

Operating frequency (centre), fc	300 MHz
FM sweep bandwidth, B	200 MHz
RF power, Pt	20 dBm
Antenna gains, Gt, Gr	10 dBi
Noise figure, N	6 dB (F = 4)
Associated standard range resolution, ΔR	43 cm with εr = 3.1
Depth precision in phase-sensitive mode	3 mm RMS, provided SNR >21 dB
Pulse duration, T	1 s
Total acquisition time	60 s for c. Ten pulses each with four RF gain values
ADC sampling rate	>12 k samples/s
Ice attenuation	0.015 dB/m
Maximum operating range, R	2 km
Reflection coefficient between internal layers, ρ	−60 to −90 dB
Reflection coefficient at ice sheet base, ρ	−2 dB

With a ramping frequency, the chirp's time to travel to the reflection and back to the radar results in a lower frequency than what the radar is currently transmitting. The frequency difference between these two frequencies is linearly dependant on the range distance to the reflection layer.

Mixing the transmitted and received signals generates a sum or difference frequencies. The difference frequency is selected by a filter and recorded. The frequency and phase information of the transmitted signal is very precisely defined. By tracking and measuring the phase information, phase-sensitive techniques can be used to process the measurement.

The deramped frequency of the FMCW pRES is derived using the expression:

$$f_d = \frac{2B\sqrt{\varepsilon_r}}{Tc} \tag{4.5}$$

Where B is the sweep bandwidth, and T is the pulse duration. The range to a reflection boundary is not a single measurement, but an average depth spread across the radar footprint. The standard range resolution (ΔR) represents the minimum vertical distance required to resolve two separate reflections and is calculated for FMCW systems using:

$$\Delta \mathrm{R} = \frac{v}{2B} \tag{4.6}$$

Using the above constants and the 200 MHz bandwidth of the ApRES system, the conventional range resolution of the pRES system without phase processing is 0.43m with the additional advantage of a very high SNR (Brennan et al., 2014). Using interferometric techniques, the changing distance between sensor and target from two measurements is determined at much higher accuracy and is typically assumed to be a fraction of the wavelength. For ApRES with a radar wavelength in snow of ~ 0.4 m, the achievable accuracy is in the mm range (Brennan et al., 2014).

The radar signal spreads with distance from the transmitter. The pRES footprint radius (r) is therefore dependent on the range to the reflection boundary layer (R), calculated using the equation:

$$r = \sqrt{2R\Delta R} \tag{4.7}$$

The range measured by the radar is an average of surface roughness across the basal reflection footprint. For ice with a 300 m basal reflection boundary, the expected radar footprint radius is 16m resulting in a footprint area of 810m^2. For the thickest basal reflection measurement of ~700m, the radar footprint reaches a 24.5m radius covering 1885m^2, respectively. These calculations are made using the assumption of a boundary layer parallel with the measurement surface. Reflections from outside of this radar footprint are considered off-nadir.

The angle subtended by the limited resolution footprint of depth R can be calculated using the above parameters:

$$\alpha \simeq \frac{2r}{R} = \sqrt{\frac{8\Delta R}{R}} \tag{4.8}$$

If the received voltage exceeds the limits of the ADC, signal clipping occurs when converting the signal to digital. The upper range of the signal will not be correctly resolved, the dynamic range of the converted signal is lost, and signal clipping occurs. The transmitted signal maintains a constant output power, but the returning signal is much weaker from energy attenuation within the medium, energy reflection, and energy dispersion with depth. To ensure a sufficiently strong signal is received without overloading the system, the attenuator in the receiver chain and the AF gain amplifier are adjusted to best suit the site conditions. When establishing a field site, several gain and attenuation settings are tested to determine the most suitable settings for the site. The site settings depend on the strength of the reflections, the ice thickness, and the attenuation of the ice. The histogram of the ADC dynamic range values is analysed for signal clipping and dynamic range to determine the best settings. The histogram should appear as a normal distribution around the 0V centre with tails approaching zero frequency. Signal clipping is identified by an increased count of values hard up against the positive and negative values.

The ApRES instrument can be operated in two modes depending on the survey objectives. In attended mode, the pRES is operated manually using a computer web browser via an Ethernet cable. Radar measurement parameters are adjusted in this mode to find the optimal settings and the data files extracted through the browser.

The attended mode is used for finding the correct measurement settings to be defined in the configuration file before a long-term deployment in unattended mode. The manual operation of attended mode allows the instrument to be used as a survey tool across multiple sites. The instrument measures a series of point locations that are repeated after a particular time.

4.2 ApRES Dataset

4.2.1 Field Measurements

The ApRES requires only a simple set up for each survey measurement. The instrument sits inside a pelican box linked with cables to two identical skeleton design antennae and the controlling laptop via an ethernet cable. For measurements, one antenna operates as the transmitter and the other acts as the receiver (Figure 7 and Figure 8). Whenever possible, the same set of cables, antennas and transmitter are used for the measurements, so no change in equipment influences the sensitive radar signal.

Two flags were established at each site, approximately 9.5 meters apart, to mark the exact antennae position for each repeated measurement. The flag height above snow was measured from 2019 onwards to estimate annual snow accumulation. A handheld GPS unit was used to measure the position change of each site between repeat measurements.

Figure 8. *Field setup of the ApRES measurement at a marked measurement site. Flags mark the antenna positions.*

4.2.2 ApRES Dataset Description

ApRES measurements were started in the 2015 Antarctic field season along the northern SPOT route (Ryan, 2016). These measurements have been continued alongside logistics support to deep-field sites to include the much longer survey transects.

Table 4 outlines the annual datasets for each field survey.

In 2018 the ApRES instrument malfunctioned and would not register the basal reflection. Another ApRES unit had to be used from 2020 onwards to replace a faulty unit for the remainder of the survey. A single measurement of grounded ice up at site System_test was made between P3 and P4 as another calibration point of the two ApRES units. Siple coast measurements were unaffected. Measurements of basal melting required the exact same ice column to be remeasured.

Table 4. *Sites measured and field comments for each season of measurements.*

Antarctic Season	Sites Measured	Notes from annual measurements
2015	T1-T12	Sites T1-12 established and marked with flags Each site was measurements were made at each site with a repeat period of 5-14 days. Signal clipping at sites T1-3
2016	T1-T7	T8-T12 were unable to be surveyed due to weather constraints Signal clipping present at site T3
2017	T1-T11	All sites remeasured except T12
2018	T1-T21 P1 -T11	New sites T13-21 and P1-11 established and marked with flags Extends study area to 100km of RIS
2019	T1-T21 P1-P11 System_Test	ApRES instrument change to a newer model after poor calibration with another unit. System_Test measurement on grounded ice. Flag height measured for rough accumulation rates.
2020	T1-T21 P1-P11	Missing marker flags at T1, T2, T4 and T13-21 Sites were re-established at the estimated location

4.3 ApRES Methods

The BAS has developed and provided a suite of MATLAB scripts utilising the signal processing toolbox, specifically for the processing of ApRES measurements. This study used the latest available BAS data package, updated by Craig Stewart, for all ApRES processing. The package includes many functions performing the loading, processing and displaying of the data. For simplicity, only the user-operated scripts are included within the description of the processing methods.

4.3.1 Pre-Processing

The newer ApRES machine introduced for the 2019/20 season recorded additional header configurations in the survey files not present in previous data files. The new files were not compatible with the MATLAB script package analysis without removing ten blank header lines from the DAT file header information. The deleted header metadata was related to GPS and iridium communication information, unused for ApRES survey measurements due to the time taken to establish these connections. Therefore, the removal does not impact the recorded information or analysis between sites in any negative way.

4.3.2 Amplitude Profile

The script ***Fmcw_plot.m*** plots each ApRES measurement's amplitude and phase information with depth. This raw depth is calculated from the TWT using the velocity of light in ice. The only user-defined parameters for these scripts was the depth displayed, with a maximum range of 2000m. Throughout this study, a range between 400 and 800m was sufficient to view the ice shelf base.

Radar measurements from the same site were plotted together to compare the interannual coherence and reliability of internal layers and the basal reflection depth. Maximum, minimum, average and range statistics from each measurement were recorded. The x and y values for the peak amplitude for the basal reflection and the linear trend between reflection amplitude and depth was modelled.

The basal reflection strength for each ApRES measurement was interpreted using a qualitative scale (

Table 4). 'Very Weak' reflections displayed no single distinct basal reflection signal. 'Strong' reflections featured a sharp amplitude peak over a 0–2-meter range. The scale categorises the 'peakiness' and specularity of the basal reflection to interpret the nature of the dielectric contrast and the ice-ocean interface at the ice shelf base.

While the qualitative classification is robust for distinctly strong or weak basal reflections, the distinction of moderate classifications is more subjective for sites with complex or ambiguous basal reflection shapes. Moderate classifications include; distinct but low amplitude basal reflections, steps in the basal reflection greater than 2m range, or multiple

strong basal peaks. The large variety of reflection shapes meant many sites bordered weak/moderate or moderate/strong categories depending on the complexity of features.

Table 5. *Criteria for qualitative interpretation of basal reflection strength. The chosen basal reflection peak is marked (orange), and the beginning of the basal reflection ramping (yellow).*

Example Reflection	Rational
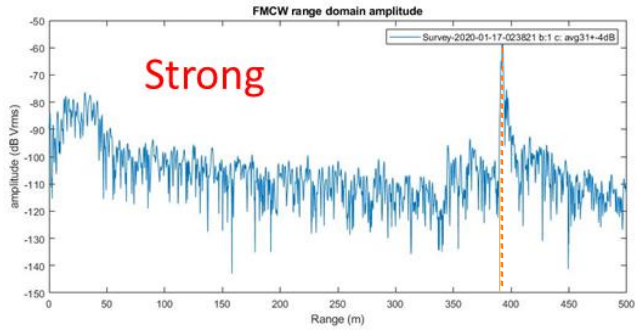	**Strong** - A clear, sharp reflector. High peakiness over a very short range.
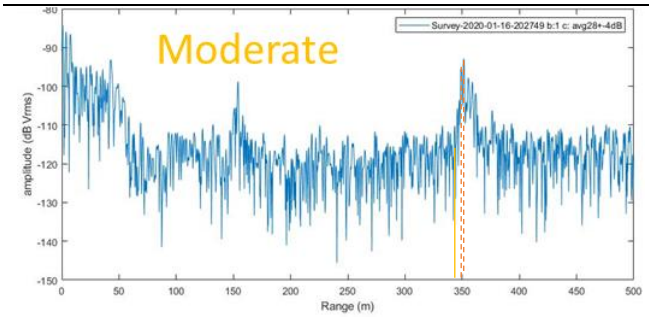	**Moderate** - A basal reflection signal without a single sharp reflection amplitude increase, and a lower amplitude change. It may be displayed as steps, multiple peaks or gradual ramping over a slightly larger range than a strong reflection (10-50m).
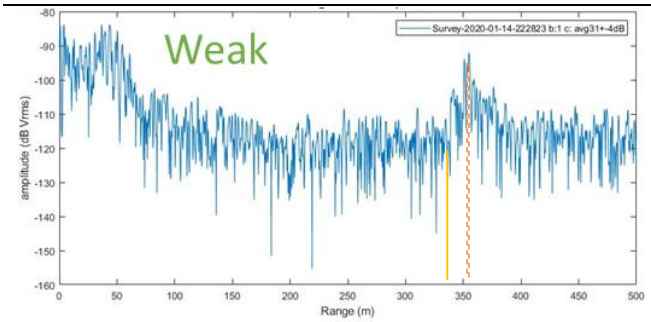	**Weak** - A basal reflection signal spread diffusely over a larger range.
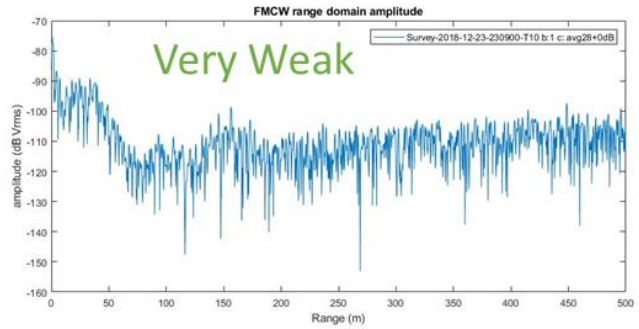	**Very weak** - An imperceptible basal reflection

A quantitative measure of basal reflection power was implemented to support the qualitative manual interpretations. The basal reflection power depends on the basal reflection coefficient and the ApRES gain and attenuation settings, so the difference between internal layer amplitude and basal amplitude was used as the measure. The internal reflection amplitude was linearly modelled with depth to estimate the reflection strength at the ice shelf base. The highest amplitude peak across the base range determined ice thickness for weak reflection sites where a clear basal peak cannot be identified (Table 5). This method does not quantify the range of the basal reflection, so there is still some variation between reflection power and classified reflection strength, particularly between weak and moderate sites.

Sites with reflection power over 30 dB have been classified qualitatively as strong reflections, while powers below 20 have primarily been defined as weak. Moderate reflection power dominates the middle 20-30dB.

4.3.3 Ice Thickness

The ice thickness at each site was calculated using a constant radar velocity of 0.169 m/ns to determine the range of the basal reflector from the two-way travel time. The thickness was manually selected using the same criteria as for determining basal reflection power above. A firn correction was applied to the raw thicknesses to account for increased velocity in the lower density firn. Firn density profiles are sparse across the RIS, and so the standard -7m firn correction was used for all sites (Arnold, 2016; Ryan, 2016).

4.3.4 Inter-Annual Processing

Fmcw_process_config.m contains all the user-defined parameters for the fmcw_melt processing script for executing strain and melt analysis. The most significant inputs include:

The functions ***cfg.padfactor***, ***cfg.chunkWidth*** and ***cfg.useUDStrainRate*** were tuned to determine the best modelling of the strain fitting with depth when the default and recommended settings would not correctly model the range change of internal layers through the ice column. Errors solved by properly tuning these settings include phase unwrapping errors, causing strain fitting with 'steps' and large zig-zag fluctuations from a linear fitting in the lower layers.

Table 6. *FMCW_process_config.m configuration file inputs*

Configuration Parameter	Description
cfg.bedSearchRange	Defines the range over which the base reflection is searched for. The basal reflection interpretations from fmcw_plot inform this value.
cfg.bedMethod	Defines the method used for bed identification. Input maxAmp uses the maximum basal amplitude. Input xcorr matches the reflection shape between measurements.
cfg.bulkAlignRange	Defines the depth range that is used to co-register the two measurements.
cfg.firnDepth	Defines the firn depth to exclude from strain fitting.
cfg.bedBuffer	This is used to remove spectral leakage from the base or remove incoherent internal layers at the ice shelf base from strain fitting.
cfg.padfactor	Pad factor (interpolation factor). Higher pad factors increase the bin lag, and a value greater than 10 is required for Smart Unwrap processing.
cfg.chunkWidth	The chunk width used to determine the fine offset of bin lag with depth.
cfg.useUDStrainRate	The user manually defines the vertical strain rate.

Fmcw_melt.m was used to analyse the reflection information of two repeating ApRES measurements to calculate the basal melt component of thinning between the repeat times. Where multiple measurements were made annually, all combinations were processed to determine the best correlation between measurements settings. For sites with more than two seasons of data, measurements up to 2 years apart were processed. This was necessary for some measurements at the end of the 2018 ApRES survey that were unable to match enough internal layers for an accurate strain fitting with the years prior and following. For these sites, the long term measurements between 2017 and 2019 were used with a measurement period of approximately two years.

Co-registration

Before further processing the measurements, the two radar profiles are co-registered through cross-correlation of the upper layers (Figure 9). The correlation value between the two profiles is calculated, and any shift correction is applied to the second radar profile to align the upper internal layers and remove any vertical shift of the radar position between measurements. This shift removes changes due to surface accumulation and upper firn compaction from the calculated thickness and range changes.

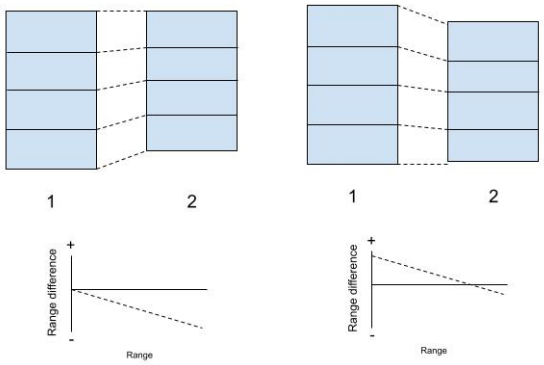

Figure 9. *Co-registration of upper internal layers during ApRES processing. Co-registration of the ice column should align the upper layers of the ice shelf. The range difference at depth 0 should also be zero. When the intercept does not align, the strain thinning rate will remain accurate as the slope is unchanged. The basal melt rate will still be accurate as co-registration will also change the bed range difference by the same offset. The basal strain thinning and observed thickness change may not be accurate.*

Vertical Strain

The change in the range of internal layers is plotted against depth. Where strain thinning occurs, internal layers are travelling towards the surface, resulting in a negative range change from the baseline of the ApRES radar. For floating ice shelves with no basal shear stress, the vertical strain rate is assumed to be constant over the ice column, and the range change of internal layers increases linearly with depth (Cuffey & Paterson, 2010).

Above the firn-ice transition**,** the compaction of snow and firn also contributes to the thinning of internal layers until it reaches the incompressible density of ice (~900kg m^{-3}). Therefore, upper layers will appear to be undergoing a higher rate of strain thinning than the rest of the ice column, with an exponential decrease of this strain rate as it approaches the density of ice, where it will represent the strain rate across the entire ice column.

The defined firn transition depth excludes these compressible firn layers above the boundary from the ice column's strain fitting. For sites across the RIS, a firn boundary of 50-

70 meters was used (van den Broeke, 2008). The firn boundary was confirmed for individual sites by identifying the beginning of the curved deviation from the linear strain fitting of the lower ice column.

The vertical strain across the entire ice column is calculated by modelling a linear fit to the range change with depth (Cuffey & Paterson, 2010). A linear fit was representative as all sites were greater than 5km from the grounding zone and so removed from depth variable strain rates of tidal flexure. The error is estimated from the residuals of this model. Both r^2 and P values of the linear fit are used to assess the quality of the strain fitting, particularly when comparing the same site from different measurements. The strain value is used for estimating the basal strain thinning component from basal thickness change between the two measurement periods. For comparison with other sites and studies, it must be converted to a rate of change. As strain is unitless, the rate unit a^{-1} is used but note that shorter period studies may use day^{-1} strain rates. Matching specific low reflection power internal layers becomes more difficult at depth with increasing relative deformation. The linear strain fit will often be determined using the upper layers and then extrapolated down to the ice column base to estimate the basal range change to vertical strain.

Basal Melt Rates

The basal reflection depth for two consecutive measurements is determined by a user-defined method. The high precision basal range change is determined by phase change between the two measurements. Half wavelength ambiguity can occur with changes greater than the half-wavelength (~0.3m), where the number of phase unwrappings is uncertain. In this instance, the TWT distance informs the number of additional wavelengths change. The addition of phase information when determining ice shelf thickness of the second measurement will result in a variation to the manually picked basal peak but must be checked alongside these to ensure the right phase unwrapping has been used. This precision is relative to the basal peak and shifted from co-registration, and it is not considered more accurate than the picked base.

By modelling the vertical strain rate and the range change of internal layers within the ice column as linear a function with depth, the expected basal strain thinning over the measurement can be predicted. The difference between the total thinning and the strain thinning is attributed to basal melting (Figure 10). The measurement error is calculated from the estimated error of the linear strain model and the basal range change.

The ApRES sites are separated by 30 km on average, situated on ice with different origins and properties, so the processing settings for each site must be tuned manually. Sites with similar thicknesses and ice origin still required some tuning between sites. Significant changes in the basal reflection of internal coherence between annual measurements also required significant tuning to produce accurate and coherent strain fittings. Where strain

was unable to be accurately determined automatically, a user input for strain could be used to input an approximate value for the strain rate.

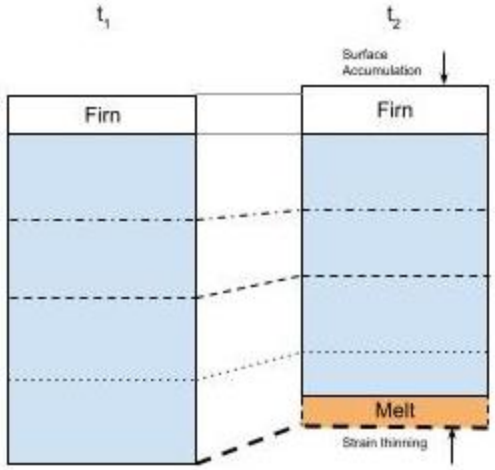

Figure 10. *Diagram of ice column thickness change between t1 and t2.*

Multiple melt analyses were performed at each site using all possible radar measurements combinations and configuration settings. The best melt product and the quality of the calculations were determined by comparing the following measures. The coefficient of determination (R^2) of the linear strain model was high, or a manual assessment of the matched internal layers. The linear model intercept is approximately at the origin of the graph. There is a high correlation between upper layers (above 0.80) and a co-registration shift within an expected range (±0.5m). When a half wavelength ambiguity warning was identified, the phase derived bed observed thickness change was assessed against the raw thickness changes.

4.3.5 Instrument Variability and Malfunctions

Several sites from the 2018 survey displayed very different reflection shape throughout the ice column, most notably at the basal reflection. Sites T2 to T5, T8 to T9, T12, T15 and T16 all displayed a reduction in amplitude and some no observable basal reflection. The change in basal reflection is not considered realistic due to the observed loss of coherence seen throughout the entire ice column. This decrease in coherence created very low correlations between internal layers during strain fitting. For this reason, the year 2018 was often unable to be processed when calculating melt rates at these sites. A two year measurement period was used for sites where 2017 measurements could be substituted.

The southern measurements during the 2018 traverse still show strong basal reflections, strong correlations between measurements and successful determination of strain rates and melt rates. This degeneration of data quality at the last sites measured in the 2018 season is

attributed to the beginning of a malfunction of the ApRES instrument finally identified at the start of the 2019 traverse measurements, where no basal reflection could be measured. Therefore, the only limitation to the dataset interpretation is reduced to T13 to 17, where internal reflection incoherence is present, but there are no additional years to substitute. One further complication of basal reflection shape variability occurs at sites T10 to 13. In the subsequent 2019 traverse dataset, T10 to 11 and T4 continue to display "very weak" basal reflection strength and T12 to 13 display basal reflection strengths lower than previously measured in the 2018 survey. This suggests changes to interannual basal conditions were hidden or exacerbated by an instrument malfunction for the 2018 survey of these sites.

For southern sites, basal melting and strain fittings were possible using the 2018 ApRES data despite changing the ApRES instrument and measurement settings. This demonstrated that the analysis of annual measurements can still be resolved using two separate instruments with different measurement settings.

Further measurements in the 2020 field season saw numerous measurement settings applied for survey measurements at the same locations. These revealed significant changes in the reflection profile and the basal reflection peak shape, with changes to attenuation and gain settings. However, in the 2020 survey, weak basal reflection zones at T10 to 13 reappeared using the same measurement settings as 2019.

4.4 Satellite Datasets

Horizontal strain rates of the ice shelf are derived from satellite measured ice surface velocities. Maps of satellite velocities are used to determine convergence and divergence, similar to traditional surveys of stake networks. This study of regional strain rates across the RIS used multiple Antarctic velocity maps from NASA MEaSUREs products (Making Earth System Data Records for Use in Research Environments) provided by the National Snow and Ice Data Centre (NSIDC). Ice and bed topography were sourced from the BEDMAP2 GIS package.

MATLAB scripts to determine strain rates from satellite velocity fields developed by Alley et al. (2018) and used by Adusumilli et al. (2020) were utilised in this project. The scripts are used in conjunction with the newest wide-scale MEaSUREs phase-based velocity products.

4.4.1 MEaSUREs

The MEaSUREs velocity datasets use feature tracking of Landsat-8 and various interferometric and phase-based methods of synthetic aperture radar (SAR) satellite products. Three velocity products from the MEaSUREs Antarctic Velocity Maps have complete coverage of the RIS study sites:

MEaSUREs Phased-Base Antarctica Velocity Map, Version 1 (450m grid) (Mouginot et al., 2019).

The Phase-Based Antarctica Ice Velocity map is the most recent Antarctic velocity product produced for MEaSUREs. It is stated to be ten times more precise than the previous iterations with high precision velocity measurements over 80% of the continent. Multiple satellite products and several analysis techniques for SAR is used to calculate ice velocity.

1. Interferometric phases of two tracks to analyse the ice flow vector (Mouginot et al., 2019).
2. Speckle tracking for both along-track and across-track directions. It informed the phase map velocities of coastal regions (Mouginot et al., 2017; Mouginot et al., 2012; Rignot et al., 2011).
3. The Landsat-8 data was processed using feature tracking across repea pass imagery.

The phase derived velocities were acquired mostly from 2007 -2018. Phase-based velocities provided high accuracy velocity measurements across the low-flow interior ice sheets. The tracking-based measurements were mainly acquired during the years 2013-2017. Tracking based measurements were used across the velocity map for fast-moving ice and coastal areas, including most of the ice shelves.

Most velocities across the RIS are derived from speckle tracking. One central flow band downstream from the KIS included phase-based measurements. The error for ice speed was consistently higher for the tracking-based measurements compared with the phase-based measurements. At latitudes higher than 82.7 degrees S, the error of tracking based speeds increased significantly (Figure 11).

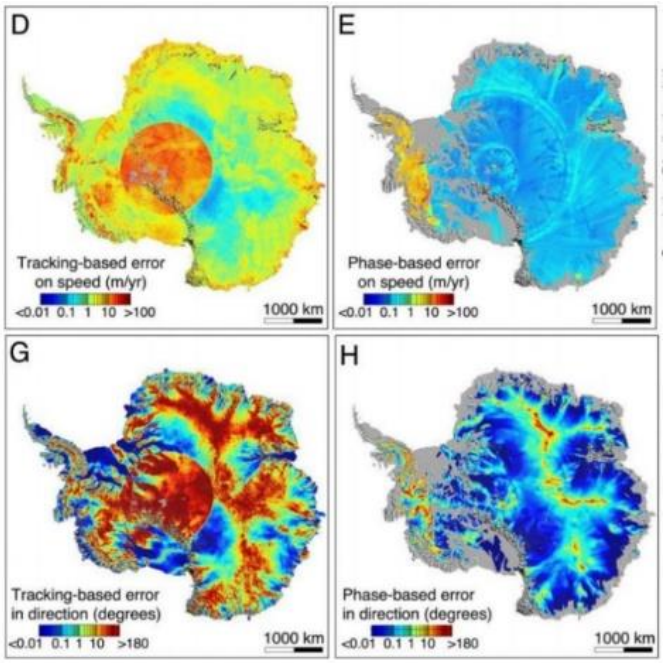

Figure 11. *The measures Phase-based velocity dataset errors from Mouginot et al. (2019).*

MEaSUREs INSAR Based Antarctica Velocity Map, Version 2 (450m grid)

The older MEaSUREs INSAR based velocity map is the original version of the previous phased-based velocity map, featuring the same coverage and resolution but slightly lower accuracies (Figure 12) (Rignot et al., 2017). It provides a comparison of the older velocity fields used by previous remote sensing studies. INSAR velocity error is shown in Figure 12.

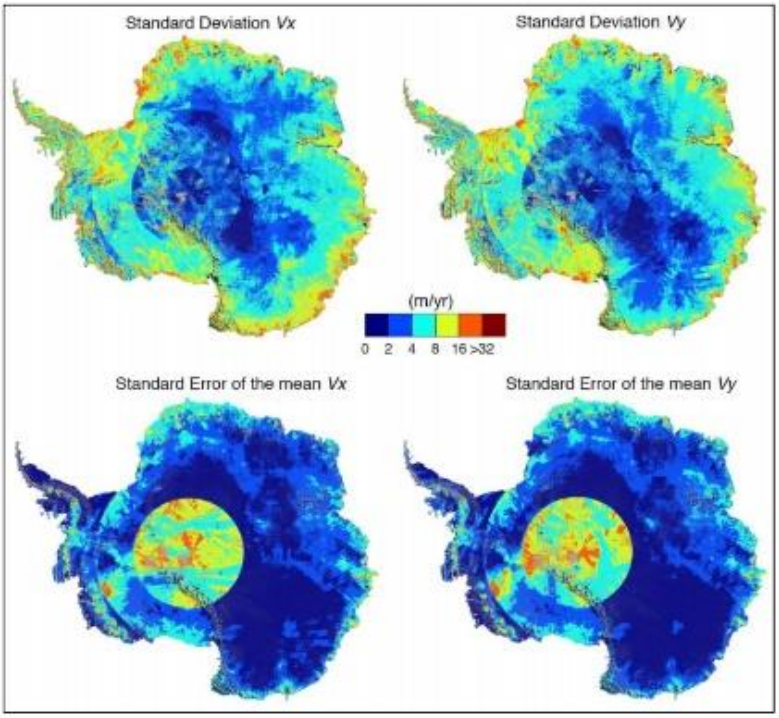

Figure 12. *Standard deviation and standard error of the INSAR measurements (Rignot et al., 2017).*

MEaSUREs Annual Antarctic Ice Velocity Maps 2015, Version 1 (1000 m grid)

MEaSUREs Annual velocity datasets from 2015-2017 were considered to analyse the annual variation of strain rates during the measurement period of the ApRES study. Only the 2015 dataset had complete coverage of all sites. The other annual products displayed very high noise. The 2015 annual velocity hopes to bridge long term mosaic measurements to an annual measurement similar to the ApRES.

The MEaSUREs velocity fields are derived from many repeat measurements, mosaicked together for complete coverage. Measurements south of 82.7 degrees do not have the same consistency of satellite coverage as they rely on polar specific, high-inclination satellites (Figure 13). For a mosaicked image where velocity is measured from differences over repeat passes, fewer measurements result in the higher uncertainty and noise seen in these regions. In these areas of consistently high or low velocities, strains remain well constrained.

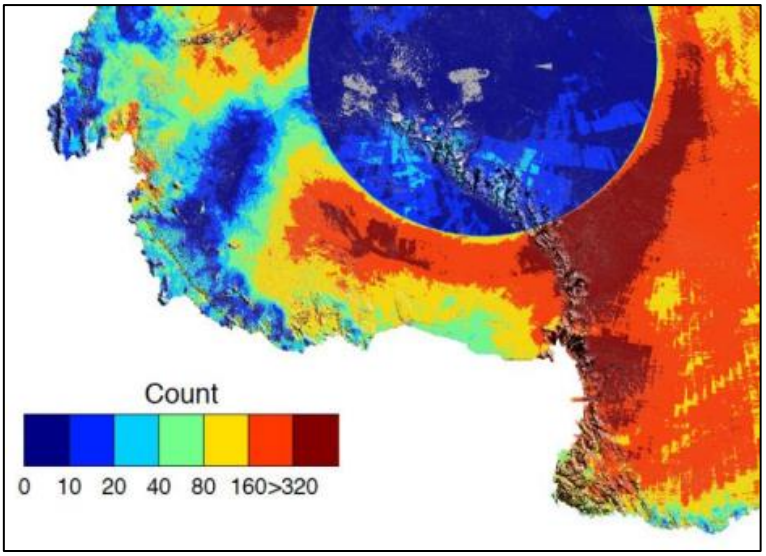

Figure 13. *Number of mosaic measurements across the RIS (INSAR user guide).*

4.4.2 BEDMAP2

The BEDMAP2 dataset includes a compilation of ice sheet and ice shelf thickness and bed elevation. Ice shelf thickness measurements primarily come from satellite and laser altimetry measurements of freeboard and had a constant error of 150m (Griggs & Bamber, 2011). The BEDMAP2 Ice Thickness Grid (Fretwell et al., 2013) was used within the MATLAB strain processing scripts to improve the consistency and extent of the data. BEDMAP2 sub-ice bathymetry elevation was generated from the interpolation of seismic measurements (Le Brocq et al., 2010).

4.5 Satellite Strain Methods

4.5.1 Workflow

The purpose of using satellite velocity maps to calculate strain was twofold. First, to validate the satellite-derived strain rate with the high precision strain measurement of the ApRES. It must be noted that the velocity maps are the compilation of data from many years while the ApRES is evaluating strain over 1 to 2 years. Secondly, where an accurate strain fitting could not be calculated using the ApRES data, the satellite-derived strain rates could be used to inform the processing by manually selecting a user-defined strain rate.

All MEaSUREs velocity datasets were received as NETCDF-4 files with individual x and y velocity components and their associated errors. GDAL was used to translate the files into georeferenced tiff files compatible with the MATLAB scripts. The BEDMAP2 ice thickness product was resampled to match the pixel size and position of each MEaSUREs velocity product used (Figure 14). Both products were then clipped to the RIS extent to save processing times. The MATLAB scripts required exact matching pixel alignments,

georeferencing and extent to calculate strain accurately. The MATLAB scripts produce longitudinal, transverse and shear strain rates across the whole ice shelf area, excluding a 10km buffer around the margins.

Linear stripes are visible across the strain product as a result of image mosaicking, satellite track orientation, ionospheric perturbations and other issues related to the satellite products (Moholdt et al., 2014). This produced strain fields with a high level of noise with much lower precision relative to pRES measurements. The high variation of strain rates occurred over distances less than a few ice shelf thicknesses, which is not expected in the central ice shelf where the stress regime is expected to be smooth and uniform. Therefore, the high strain variability is assumed to be an artefact resulting from the mosaicked velocity maps. A box lowpass filter was applied to reduce the noise using a kernel radius corresponding to 3000 meters or approximately ten ice thicknesses. Assuming the conservation of mass, the strain in the x, y and z dimensions requires a net-zero sum (equation 2.3). Therefore, the vertical strain component can be derived from the negative sum of the horizontal strain products. The vertical strain maintains the measurement artefacts from both horizontal strain maps, but still resolves wide-scale vertical thinning, despite the high noise.

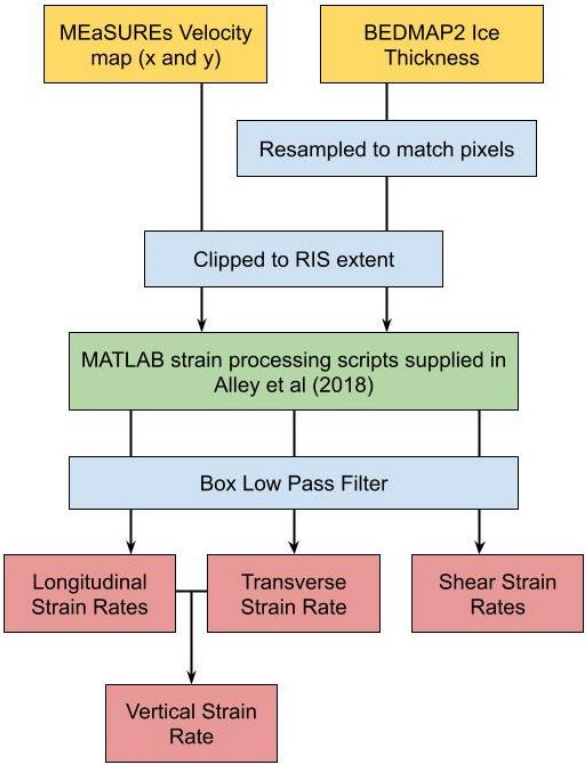

Figure 14. *Workflow for generating strain fields across the RIS. Yellow: Received datasets, Blue: GIS processing, Green: MATLAB scripts, Red: Produced strain maps of the RIS.*

5 Results

The results chapter is divided into two sections. The first section presents the results from the ApRES measurements and inter-annual analysis along the traverse. The second section presents the strain rate results produced using the MEAsUREs satellite velocity field.

5.1 ApRES

The ApRES dataset presented here is the longest continuous ApRES survey from published literature over such a large study area. The 32 sites of the RIS traverse ApRES survey covers 1000km of ice, a vast swathe of the ice shelf, and northern sites have been surveyed for five years continuously. The ApRES measurements cover point locations over a large area. The wide range of glaciological and cavity regimes results in a diverse range of precise radar observations at the point locations across the RIS.

5.1.1 Manual and Automatic Evaluation of Basal Reflection Quality

'Weak' and 'Very Weak' reflections show increased amplitude over a basal zone where attenuation or a diffuse boundary of dielectric properties at the base create the fuzzy interface. 'Strong' basal reflections are interpreted to emerge from an efficient specular reflector between meteoric ice and seawater and indicate a basal melting regime's predominance. Basal reflection strength remains reasonably consistent with each annual measurement, particularly with 'strong' reflection sites (Figure 15). Along the traverse, moderate sites are often found between strong and weak sites, suggesting there may be gradients between these zones. An increase in annual variability is seen in the central regions around T10 to T13, indicating a basal interface closer to equilibrium than the more constant northern and southern sites.

	2015	2015 2nd	2016	2017	2018	2019
T1	Strong	Strong	Strong	Strong	Strong	Strong
T2	Strong	Strong	Strong	Strong	Moderate	Strong
T3	Strong	Strong	Strong	Strong	Weak	Strong
T4	Moderate	Moderate	Moderate	Moderate	Moderate	Weak
T5	Weak	Weak	Weak	Weak	Very Weal	Weak
T6	Weak	Weak	Weak	Weak	Very Weal	Weak
T7	Strong	Strong	No data	Strong	Strong	Strong
T8	Strong	Strong	No data	Moderate	Very Weal	Strong
T9	Strong	Strong	No data	Moderate	Very Weal	Moderate
T10	Moderate	Moderate	No data	Weak	Very Weal	Very weak
T11	Moderate	Moderate	No data	Weak	Very Weal	Very Weal
T12					Weak	Very weak
T13					Moderate	Very Weal
T14					Moderate	Moderate
T15					Moderate	Moderate
T16					Very Weal	Strong
T17					Strong	Strong
T18					Strong	Strong
T19					Moderate	Strong
T20					Moderate	Strong
T21					Strong	Strong

	2018	2019
SCT P1	Strong	Strong
SCT P2	Strong	Strong
SCT P3	Strong	Strong
SCT P4	Strong	Strong
SCT P5	Strong	Strong
SCT P6	Moderate	Moderate
SCT P7	Strong	Strong
SCT P8	Strong	Strong
SCT P9	Strong	Strong
SCT P10	Strong	Strong
SCT P11	Strong	Strong

Figure 15. *Manually classified basal reflection strength for each annual measurement into one of four classes (strong, moderate, weak, very weak).*

The quantitative measure of basal reflection power is shown in Figure 16 as a logarithmic multiplicative power increase from internal reflection amplitude. The average power for each site is included in grey. Moderate and weak reflections appear higher than the quantitative classification expects when the reflection shape has an ambiguous shape despite high amplitude. The average basal reflection power is consistent with most qualitative classifications of reflection strength. The exceptions are some weak sites sitting with a reflection power within the moderate zone (T5 and T6). In this case, the severely diffuse boundary still displays a higher reflection power relative to internal reflections, but the power increase is over a large range.

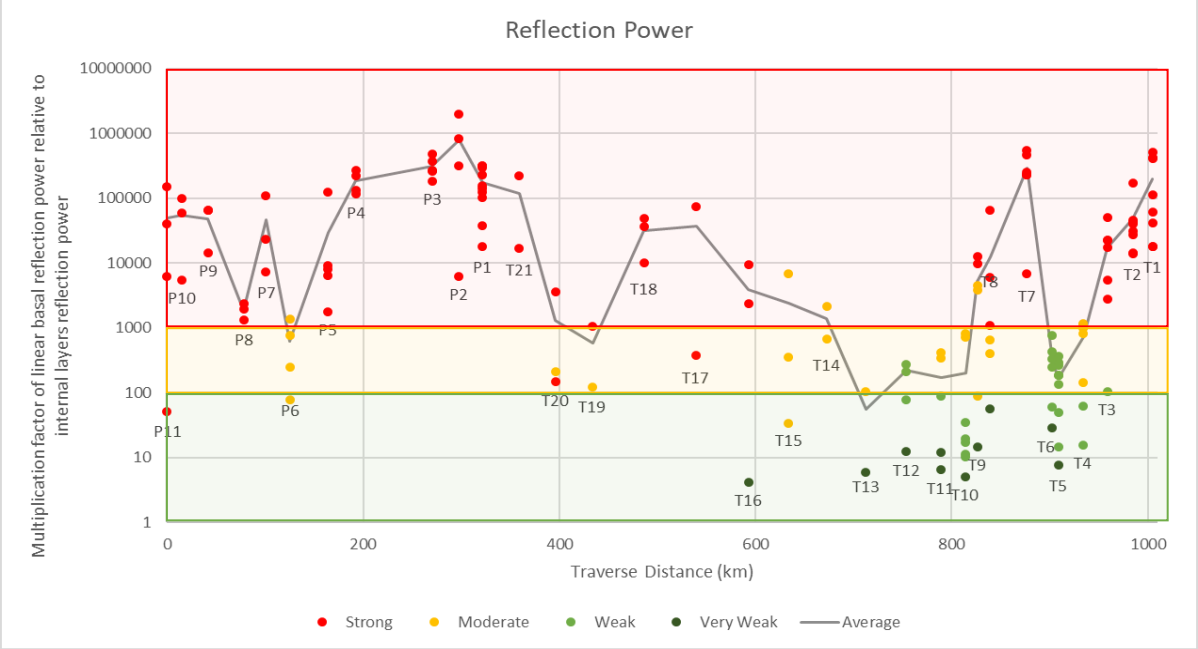

Figure 16. *ApRES site basal reflection power. Variation of the basal peak reflection amplitude relative to the near basal internal reflection power. The measure used is the multiplication factor of linear power increase above the near base internal reflection power. All radar measurements have been included, so some sites have multiple data points per year.*

Basal reflectors at sites at T5, T6 and T12, appear to have a much higher amplitude than expected for weak basal reflections. These sites remain classified as a weak basal reflection as the amplitude increase is spread over a vertical range of 10-50m, with no distinct single basal reflection peak despite a relatively high increase in power over the background reflection (Table 5.).

Some measurements show hardly any basal reflection, particularly from the 2018 season, despite identifying some form of basal reflection in previous seasons. These sites are

categorised as 'Very Weak' reflections and remain included within the amplitude difference chart as weak measurements.

The change in reflection shape is at least partially linked to a malfunction of the ApRES instrument at the start of the 2019 season survey. The previously strong basal reflections at P11 could no longer be detected until a replacement instrument was used. These northern sites of the 2018 traverse with previously strong basal reflection showed a smaller and sharper basal reflection signal. The site with previously weak/diffuse reflections (T5, T6, T10 and T12) showed no distinguishable increased reflection power.

Sites with strong basal reflections have higher accuracy for thickness retrieval. As such, sites with stronger basal reflection strengths have a higher degree of certainty when extracting ice shelf thickness and basal melt rates.

5.1.2 Grounded Ice

Only one ApRES measurement was made on grounded ice during the field measurements, located upstream from the Crary Ice Rise (CIR) at the grounded section of the Siple Coast Traverse (83.40461° S, 163.81497° W). It provides a single point measurement of ice thickness at a remote location and creates a comparison of the grounded reflection signal with the marine interfaces measured in the rest of the study. A 2-step basal reflection is seen, with peaks at firn corrected depths of 570.4 and 583.6 meters (Figure 17).

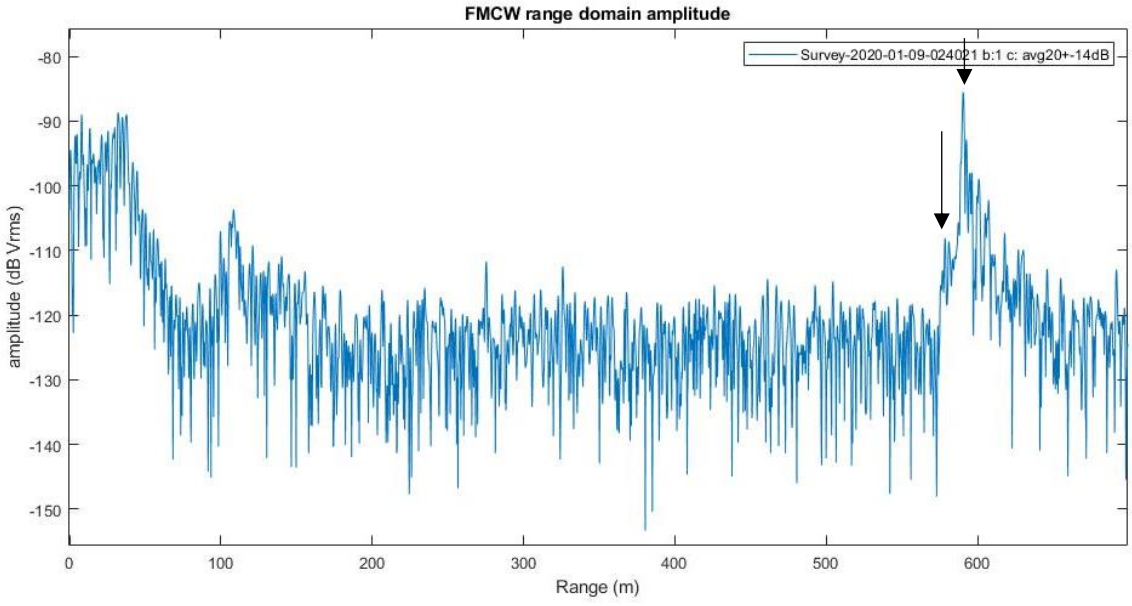

Figure 17. *ApRES measurement on grounded ice from the System Test site.*

5.1.3 Ice Thickness

Ice shelf thickness measurements from ApRES radar measurements are displayed in Table 7 and Figure 18. The lowest measured thicknesses are found at sites T10 to T13 (317 and 330 meters). For sites with strong basal reflections, the thickness error is within the range resolution of the ApRES system (0.43m). The range of basal reflection determines the thickness accuracy for sites with diffuse reflections. Sites T1 to T15 all measure within the 300 – 400m thickness seen across much of the RIS. Ice thickness increases to 641m at site T21 as the survey approaches the interior ice shelf. Sites P1 to P3 featured the highest ice thicknesses measured across the survey approaching the grounding line upstream of the CIR, with a maximum of 695 meters at P3. Across the Siple Coast Embayment, the largest ice thicknesses were observed near the grounding line.

Sites with strong basal reflection show strong agreement with values of the BEDMAP2 ice shelf thickness data set, despite a five-year difference between the release of BEDMAP2 and the collection of the 2019 ApRES measurements.

The Siple Coast traverse sites P1 to P11 closely match the BEDMAP2 thickness pattern across the region, with only slight increased thicknesses in the order of 5-20m. Only P6 with a moderate basal reflection peak revealed a much higher apparent thickness than BEDMAP2. Across the central traverse sites T14 to T21, ApRES thickness closely matches BEDMAP2 within approximately 10 m (Figure 19). Consistent variations from altimetry thicknesses occurred over the northern sites, with lower thicknesses recorded across weak reflection sites T10 to 13 and increased thicknesses measured at the strong reflection sites T1 to 7.

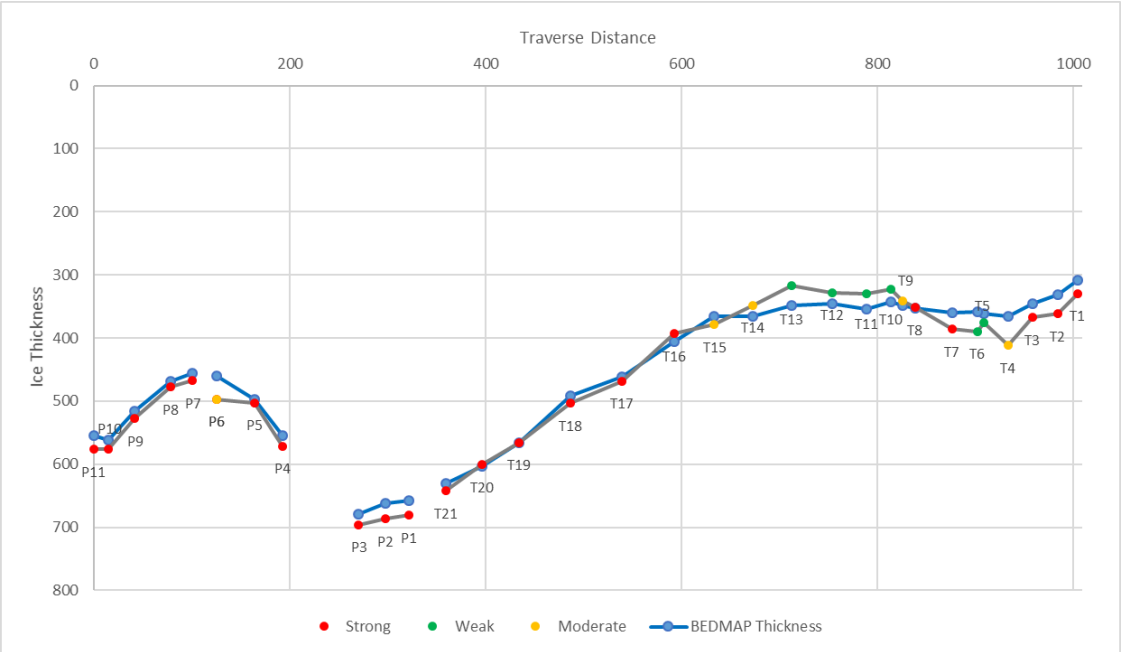

Figure 18. *Ice shelf thickness for 2019 compared with the BEDMAP2 ice thickness product at the same locations.*

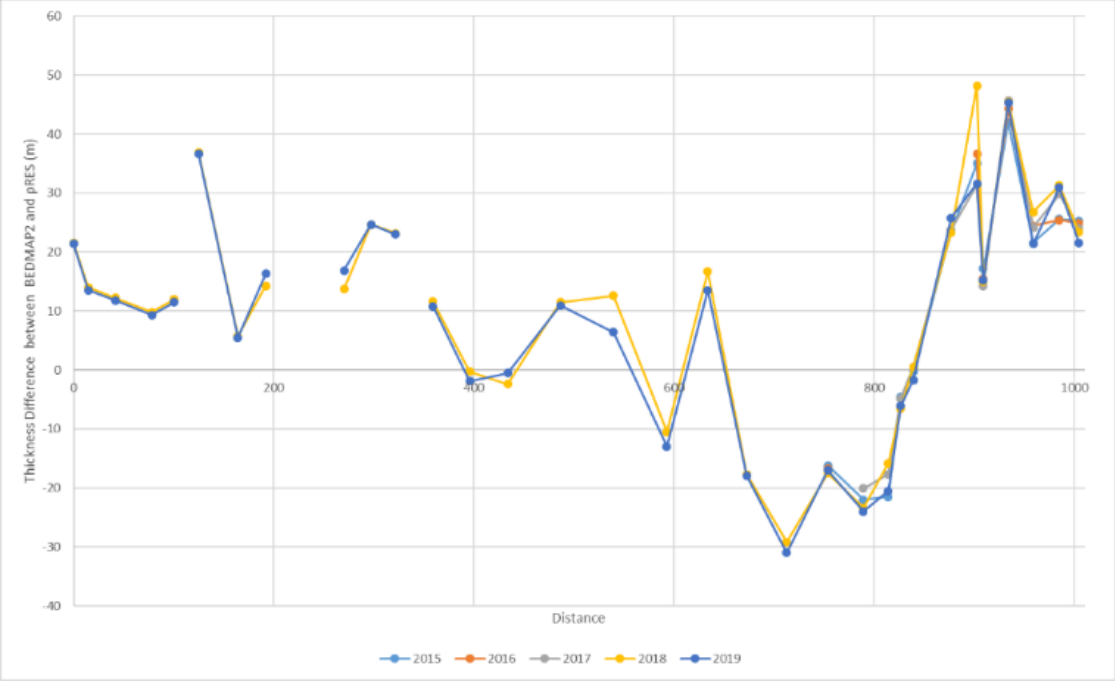

Figure 19. *The variance of ApRES determined ice thickness from BEDMAP2 interpolated thickness; positive values indicate increased thickness of ApRES measurements relative to BEDMAP2.*

5.1.4 Vertical Strain

With one exception, all sites measured negative vertical strain (Figure 20), confirming the expected wide-scale strain thinning across the Ross Ice Shelf away from complex grounding areas. No site showed an error larger than the strain magnitude, so there is high confidence in the strain regimes identified. The small-scale variation of strain rates is likely due to noise in the satellite velocity maps.

Downstream from P11 and P1, ApRES vertical strain rates become steadily more negative with distance from the grounding line and increasing ice velocities.

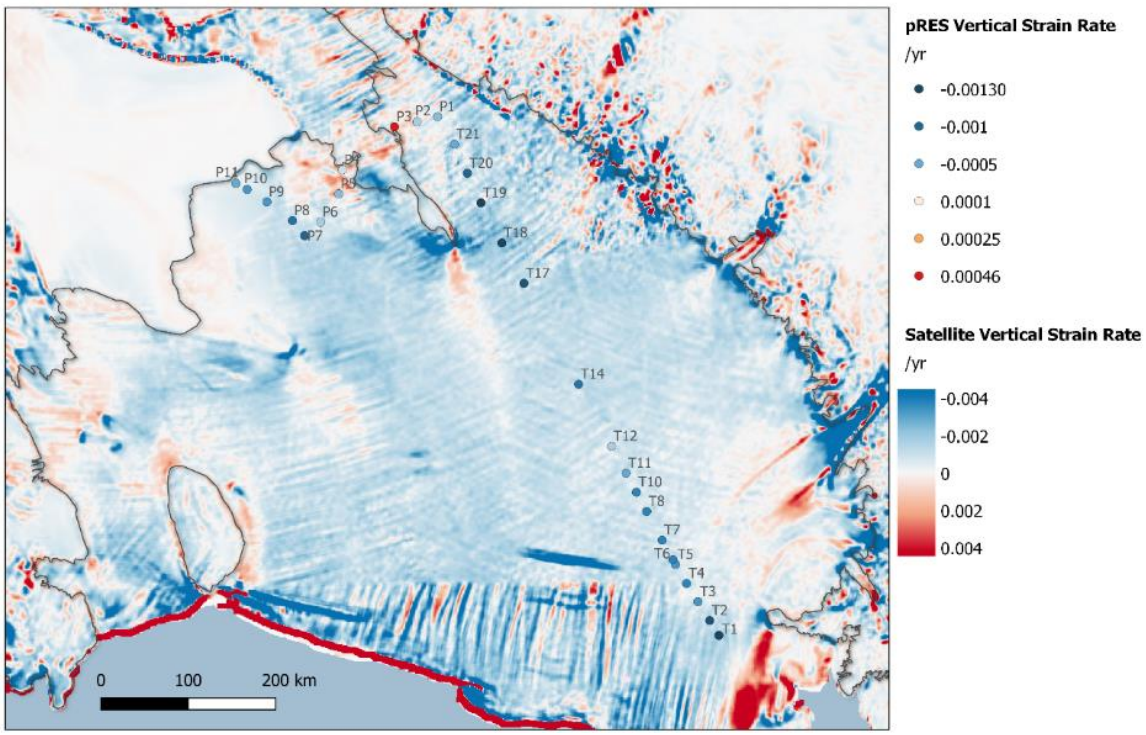

Figure 20. *ApRES vertical strain rates plotted over satellite-derived vertical strain rates.*

The ApRES measurements identified only one location of positive vertical strain at site P3. The site is located upstream of a regrounding zone upstream of the CIR and was the closest site to a grounding zone. Across the northern sites, T12 showed the lowest vertical strain with $\dot{\varepsilon}_z$ = -0.0005 a^{-1} (Figure 21). The site, located at HWD-2, also has the second-highest shear strain rate measured. Sites T4 to T12 reveal slightly lower magnitude but consistent strain rates of approximately $\dot{\varepsilon}_z$ = -0.005 a^{-1}. From T4, a steady increase in the strain thinning is observed as sites move north to a minimum of $\dot{\varepsilon}_z$ = -0.0011 a^{-1} at T1. Both southern transects aligned parallel to flow (T19 to P1 and P7 to P11) also showed increased rates of strain thinning as the ice moved north further from the grounding line. The remaining sites aligned transverse across flow showed variable strain rates.

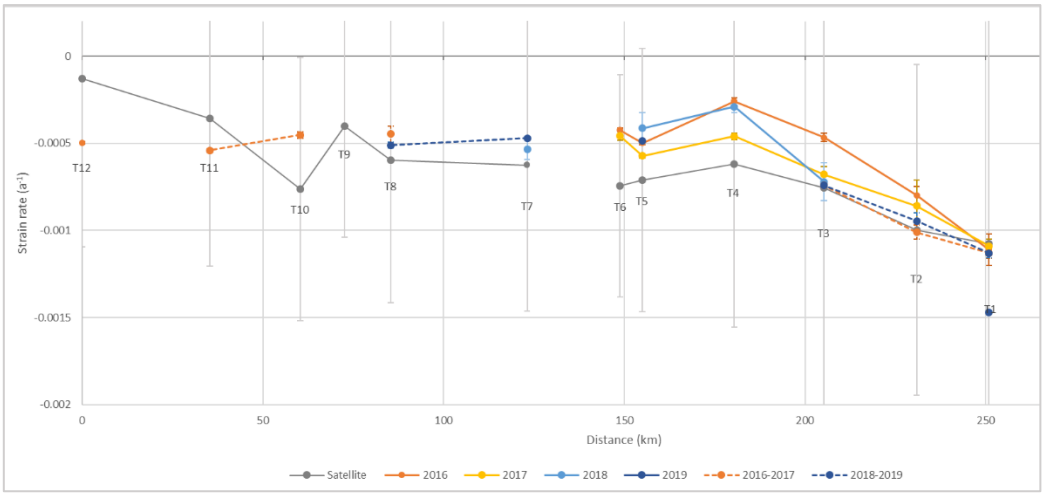

Figure 21. *Annual vertical strain measurements across the northern SPOT sites. The satellite-derived strain rate is shown in grey.*

North of T11, satellite-derived vertical strain rates are consistently lower compared to the ApRES derived values (Figure 21). Site T1 had the most consistent interannual strain rate with vertical thinning of -0.00011 (Figure 22). 2019 was the exception, with higher vertical strain thinning of -0.000147, linked to the lower coherence of the 2018 measurement.

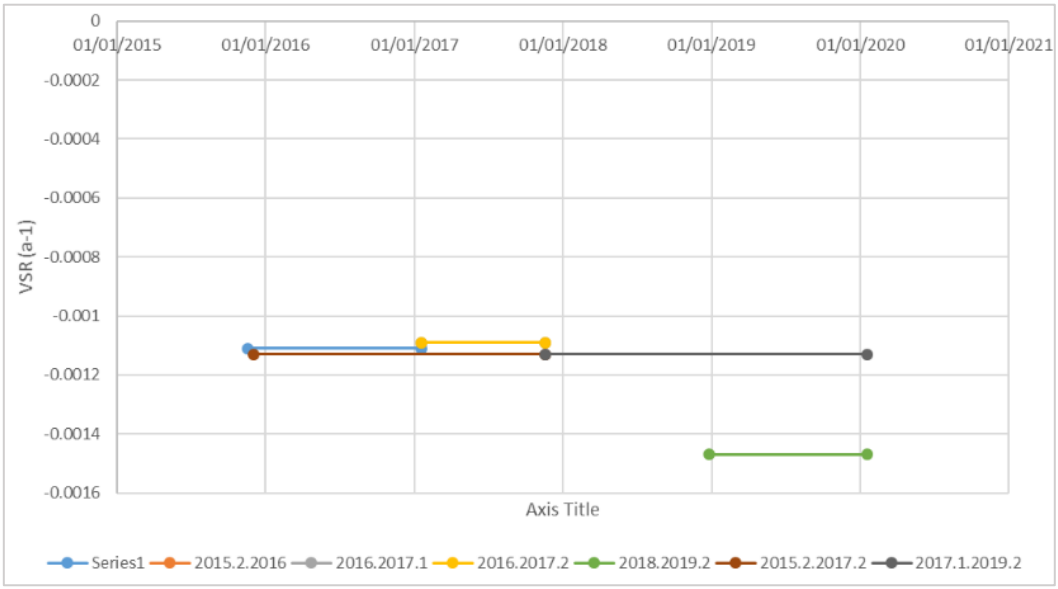

Figure 22. *Site T1 measured vertical strain rates throughout the study period.*

The vertical strain was unable to be measured at four sites in the central RIS (T9, T13, T15 and T16) due to poor coherence and correlations of internal layers between measurements. This poor coherence produced wildly fluctuating strain fittings that could not produce the required number of internal matches to fit a linear model.

5.1.5 Basal Melting

Precise basal melt rates were able to be resolved at 21 of the 32 ApRES sites (Table 7). The amount of basal melting at each location is shown in map view and as a cross-section in Figure 23. At two sites, T19 and T17, likely basal freezing was detected. However, at T19, there was uncertainty about the basal mass balance sign. Weak internal layer correlations and diffuse basal reflection prevented basal melting from being quantified at the remaining sites across the central RIS. Basal reflections that were strong or moderate but measured low or zero basal melting may indicate transient melting with low net mass balance values. The remaining sites with weak or very weak basal reflections are interpreted as undergoing basal freezing processes. Melt rates could also not be evaluated for sites where vertical strain could not be reliably constrained (T9, T15 and T16). The basal reflection range change could not be accurately determined for sites T5 to T6, and T10 to 13, preventing the calculation of basal mass change. Basal melting was converted to mass loss using an ice density of 917 kg m^{-3} (Table 7).

The regions of melt detected along the RIS traverse are grouped and presented as four separate zones based on the melt pattern and strength of the region. The Siple Coast sites (P4 to P11) are separated due to the natural boundary of the CIR and the distinct glaciological regime downstream from the stagnant KIS. Sites across the SPOT are separated into three zones of basal melting, showing distinct melt rates. Sites along the centre of the traverse (T5 to T19) show either weak basal reflections or low melt rates in the order of 0.01 m a^{-1} (Figure 23b). This zone is collectively grouped as the Central Weak Zone. The two regions of higher basal melt rates at the northern and southern ends of the SPOT are referred to as the Northern High Melt Zone and the Southern High Melt Zone.

The error displayed in table 20b is the combination of uncertainty of the linear strain model at the base and the basal range change's uncertainty. The basal range uncertainty was multiple orders of magnitude smaller than the strain fitting error for all sites.

The melt calculations for each site show a similar degree of certainty in the magnitude of basal melting. The average relative error in basal melt rates in the Southern/Northern high melt zones, Siple low melt zone (without P6), and central weak zone is 7%, 16%, and 44%, respectively.

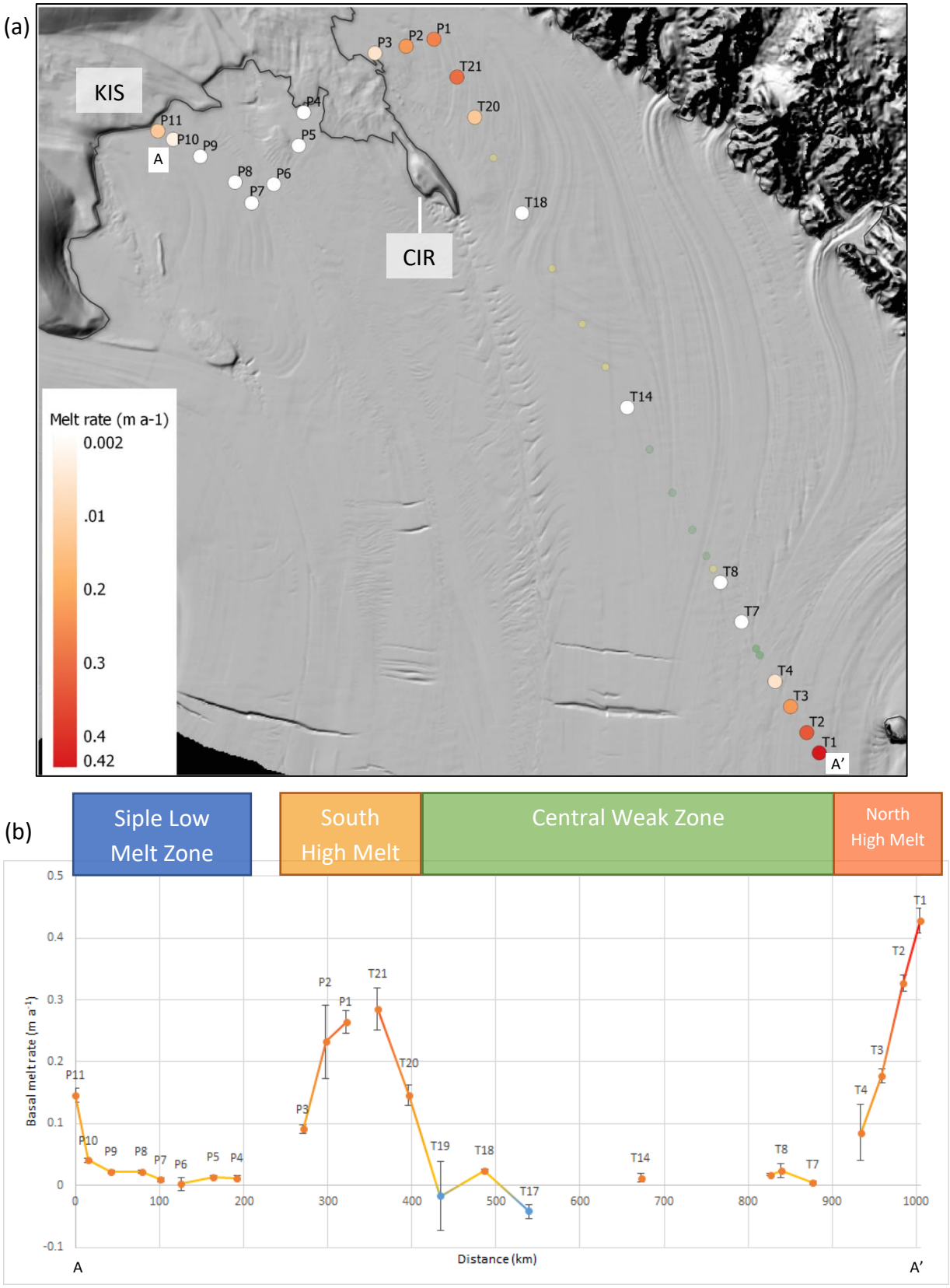

Figure 23. *Basal melt rates across the RIS traverse in (a) map view (b) and by distance along the transect. Error bars indicate ApRES error from the strain model error. Yellow and green markers on the map view indicate site locations where melting could not be quantified. The marker obscures small error bars.*

Table 7. *Ice shelf thickness (firn corrected), vertical strain rate and errors, basal melt rate and errors. Sites marked with a * show the averaged strain and basal melt rates from available measurements up to 4 years.*

Site	ApRES Thickness (m)	ApRES vertical strain rate (a^{-1})	ApRES vertical strain rate error (a^{-1})	Basal melt rate (m a^{-1})	Basal melt rate error (m a^{-1})	Basal mass change rate (kg m^{-2} a^{-1})
T1*	329.5	-1.19E-03	5.29E-05	0.428	0.020	392 ± 18
T2*	361.9	-9.04E-04	8.44E-05	0.328	0.013	300 ± 12
T3*	367.4	-6.70E-04	5.53E-05	0.177	0.011	162 ± 10
T4*	411.3	-3.36E-04	2.62E-05	0.085	0.045	78 ± 42
T5*	376.2	-4.93E-04	5.25E-05			
T6*	389.6	-4.42E-04	1.93E-05			
T7*	385.8	-5.03E-04	4.23E-05	0.005	0.002	4 ± 2
T8*	351.3	-4.79E-04	3.46E-05	0.024	0.012	22 ± 11
T9	341.9	-4.40E-04	1.10E-05	0.017	0.002	16 ± 2
T10	322.5	-4.53E-04	1.94E-05			
T11	330	-5.41E-04	1.15E-05			
T12	328	-4.98E-04	8.41E-06			
T13	317					
T14	348.1	-8.95E-04	3.03E-05	0.012	0.007	11 ± 6
T15	378.5					
T16	393					
T17	468.4	-1.14E-03	3.36E-05	-0.042	0.012	-39 ± 11
T18	502.9	-1.30E-03	6.01E-06	0.024	0.002	22 ± 1
T19	565.5	-1.20E-03	1.22E-04	-0.017	0.056	-16 ± 51
T20	601.1	-1.00E-03	3.55E-05	0.146	0.016	134 ± 15
T21	641.8	-4.76E-04	6.48E-05	0.285	0.034	262 ± 31
P1	681	-3.48E-04	3.42E-05	0.265	0.018	243 ± 16
P2	686.7	-2.47E-04	1.51E-05	0.232	0.007	213 ± 7
P3	695.9	4.62E-04	1.52E-05	0.091	0.007	83 ± 7
P4	571.3	-1.03E-04	8.54E-06	0.012	0.003	11 ± 3
P5	502.5	-3.68E-04	5.13E-06	0.014	0.002	13 ± 1
P6	496.7	-1.71E-04	3.28E-05	0.002	0.011	2 ± 10
P7	467.5	-9.55E-04	1.08E-05	0.009	0.003	8 ± 3
P8	477.3	-8.07E-04	1.08E-05	0.022	0.003	20 ± 3
P9	527.8	-6.68E-04	7.52E-06	0.022	0.002	20 ± 2
P10	575.5	-5.60E-04	9.90E-06	0.040	0.003	37 ± 3
P11	576.4	-4.40E-04	2.86E-05	0.145	0.011	133 ± 10

Siple Low Melt Zone (P4 to P11)

The Siple Coast zone includes eight sites in the Siple Coast embayment, separated from the SPOT by the CIR. Consistent low melt rates of approximately 0.01 m a^{-1} were measured across sites P4-P7, aligned in a transect perpendicular to ice flow.

Melt rates increase slightly from 0.01-0.04 m a^{-1} as sites P7 to P10 progress closer towards the KIS grounding line, correlating with increasing thickness and decreasing vertical strain rates. Relative to the grounding zone, P7 is approximately 110km north, and T10 is 50km north. Site P11 is located 11km north of the KIS grounding zone and measured the highest basal melt rate of 0.14m a^{-1}.

Weak Central Zone (T5 to T19)

Across the weak central zone, it was only possible to measure melt rates at locations with distinct basal reflections. At these locations, sites T7, T8, T9 and T14 observed melt rates less than 0.02 ma^{-1}. At the southern margin of the zone, T17 to T19 featured similar melt rates between -0.04 ma^{-1} and 0.02 ma^{-1}. Weak basal reflections with undetermined basal mass balance were present at the remaining eight sites along T5 to T16, including sites with at least one weak basal reflection. The weak central zone appears to have minimal variations of basal melting and freezing across the central area of the RIS.

South Melt Zone (T20 to P3)

Sites T20 – P3 featured elevated basal melt rates of 0.09 to 0.28 m a^{-1} relative to the central RIS measurements, but still similar to the RIS average of 0.2-0.3 m a^{-1} (Rignot et al., 2013). The zone was situated downstream from the Whillans Ice Stream (WIS) and south of the CIR. T18 and basal melting of 0.02 m a^{-1} with low error. Moving south from T18, melt rates rise significantly from 0.14 m a^{-1} at site T20 to 0.26-0.29 m a^{-1} at T21 to P1. It must be noted site P1 features a 90-degree transect turn with P1-3 aligned perpendicular to ice flow. Basal melt rates decrease to 0.09 m a^{-1} as the transect approaches the grounding zone at site P3.

North Melt Zone (T1 to T4)

Consistent patterns of annual basal melting were measured across sites T1 to T4, the four northernmost sites of the survey across the Byrd Outflow (Figure 24). Low melt rates of 0.005–0.08 m a^{-1} were calculated at site T4 at the edge of the weak central zone. Basal melting steadily increased as the sites continued north towards T1, where the highest melt rates across the traverse were measured. T1 and T2 featured the highest melt rates of all 32 sites with an average of 0.43 and 0.33 m a^{-1} over measurements resolved over the five years.

Sites T1 to T4 have been surveyed consistently for five years allowing multiple years of melt rates to be resolved. Two-year measurement periods between 2015-2017 and 2017-2019 were calculated alongside one-year repeats. Signal clipping in the 2015 measurements

prevents strain fitting of the lower 50m of the ice shelf. Still, the resulting basal melt rates remain consistent with those measured in subsequent years. Sites T1 to T3 saw the highest melt rates over the 2017 measurement period. The 2016 year resolved slightly lower melt rates with the same pattern of increasing melt rates approaching T1, starting with a higher melt rate.

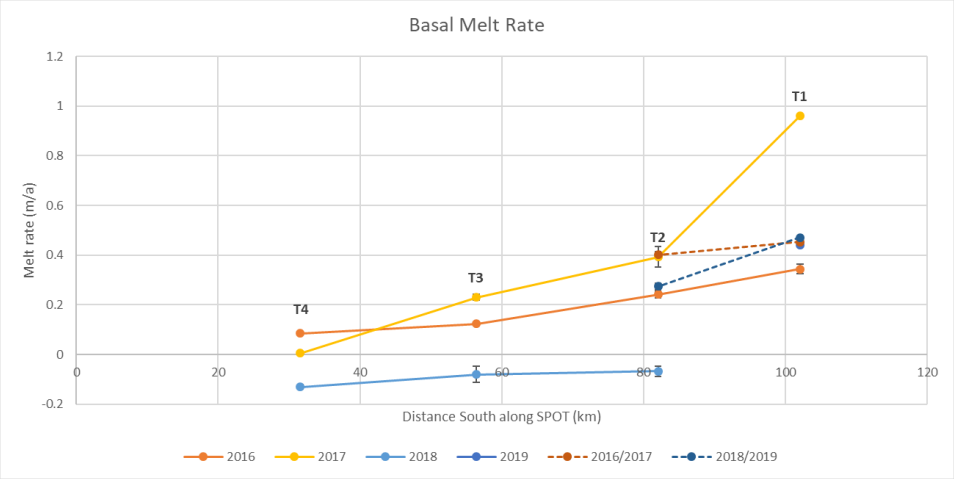

Figure 24. *Annual years of basal melt rates across the northern melt zone.*

The two-year-long measurements of T1 measured consistent melt rates of 0.34-0.37 m a^{-1} over four years of the study (Figure 25). The annual analysis between measurements displayed some variation, with an anomalous melt rate of 0.96 m a^{-1} during the 2016 year. Although this was measured over a shorter 300-day repeat period, and the 2015 year calculated a lower melt rate, this does not average to the two-year measurements. The interannual consistency of T2 to T4 suggests this may be due to half wavelength ambiguity exacerbated by the shorter remeasurement period and not influenced by enhanced mode 3 circulation.

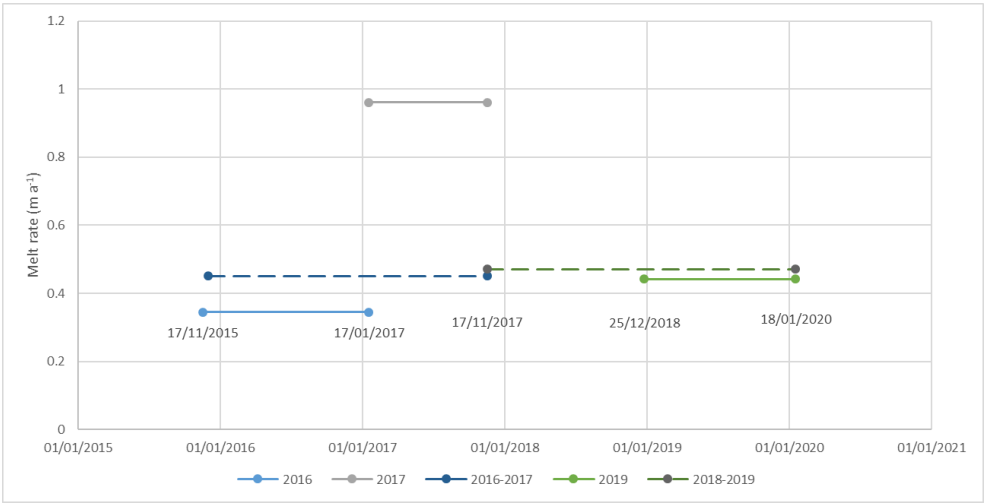

Figure 25. *Interannual basal melt rates at site T1 between measurements.*

T2 measured melt rates between 0.24 and 0.40 m a^{-1} over the study period (Figure 26). The two-year measurements displayed a greater difference over the second repeat, dropping from 0.40 m a^{-1} to 0.27 m a^{-1}. Melt rates utilising the 2018 ApRES data files could not be resolved due to a significant change in the waveform of the basal reflection. At site T3, melt rates decreased from 0.12 m a^{-1} in 2015 to 0.09 m a^{-1} in 2016. Melt rates during 2018-2019 were not able to be calculated due to a significant change in basal reflection of the 2018 season measurement.

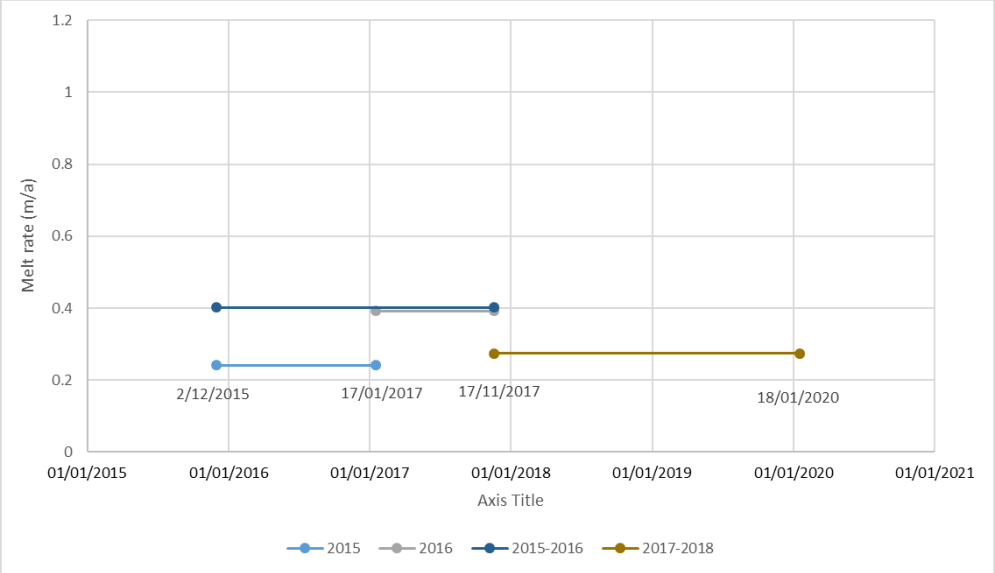

Figure 26. *Interannual basal melt rates at site T2 between measurements.*

5.2 Satellite Velocity Strain Rates

5.2.1 Horizontal Strain

The horizontal and vertical strain components for the RIS region are shown in Figure 27 and Table 8. Longitudinal strain represents strain in the direction of ice velocity, while the transverse strain is strain perpendicular to the flow. Positive values (red) express strain extension in the considered direction, while strain compression is negative (blue). Nearly the entire ice shelf is undergoing longitudinal extension. This is expected from gravity-driven ice shelf spreading (Cuffey and Patterson, 2010). Only five ApRES sites recorded negative satellite-derived longitudinal strain (P2-P5 and T20). Locations undergoing longitudinal strain compression are identified upstream of regrounding points, ice rumples and directly downstream of narrow glacier outflows.

Transverse strain rates across the RIS generally show a reversed trend of the longitudinal strain. The highest areas of transverse strain correlate with the highest regions of longitudinal strain, although with slightly lower magnitudes. This is not true for all sites, with sites T1, T2, T16-T19 and P2 showing both longitudinal and transverse strain extension.

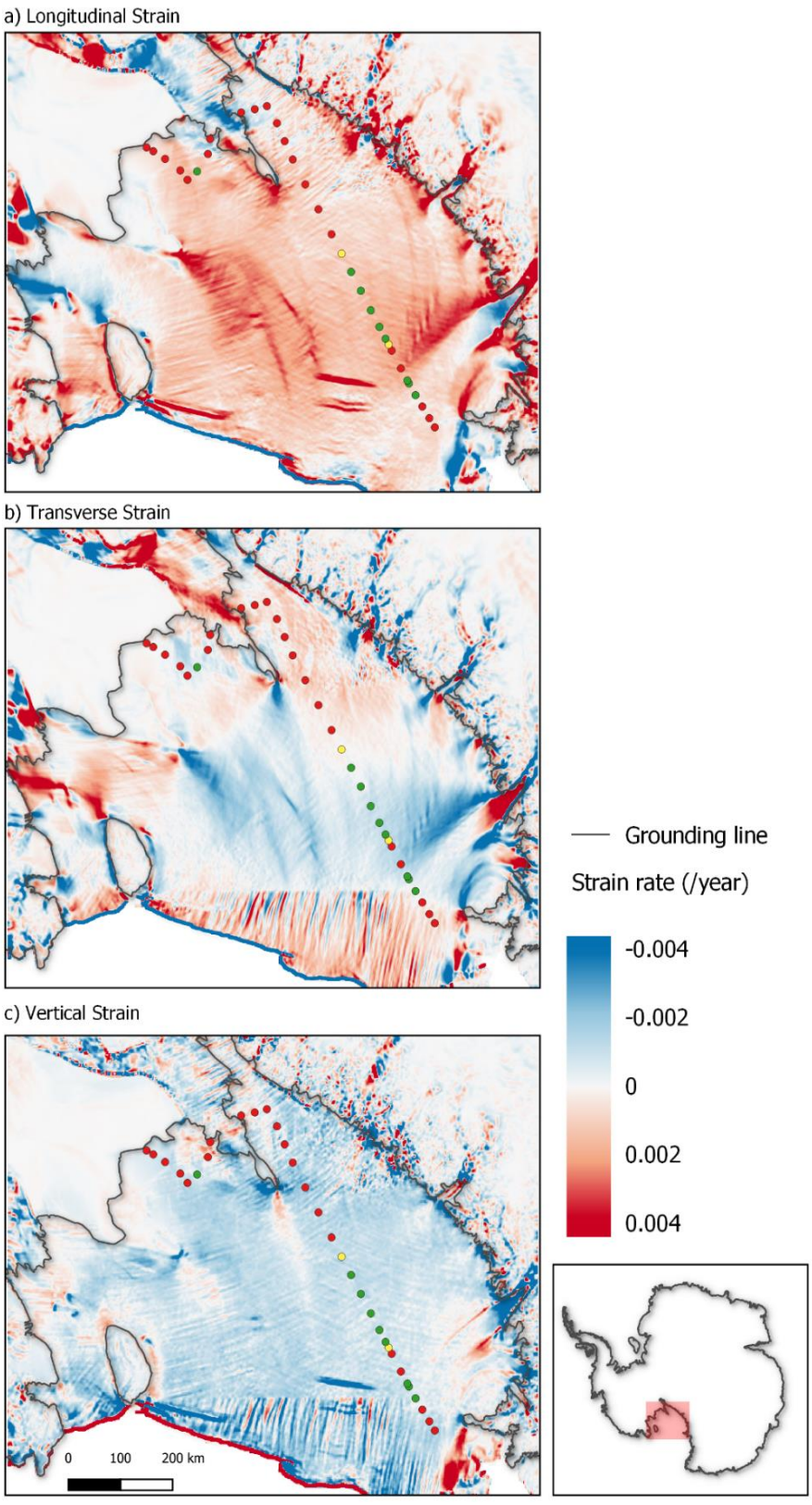

Figure 27. (a)*Transverse, (b) longitudinal, and (c) vertical strain rates derived from the MEaSUREs Phase-Based Velocity product. Strain thinning appears blue, while strain extension is red. A low-pass box filter with a kernel of 3000m was applied to all products. ApRES sites are displayed with the basal reflection strength categories: Strong (red), Moderate (yellow), Weak (Green).*

Table 8. *Strain rates derived from the MEaSUREs Phase-Based Velocity map for each ApRES site.*

Site	Longitudinal Strain Rate (a^{-1}	Transverse Strain Rate (a^{-1})	Vertical Strain Rate (a^{-1})	Shear Strain Rate (a^{-1})
T1	0.00080	0.00039	-0.00119	-0.00055
T2	0.00032	0.00060	-0.00091	-0.00071
T3	0.00062	-0.00006	-0.00051	-0.00012
T4	0.00059	-0.00035	-0.00024	0.00051
T5	0.00142	-0.00056	-0.00085	0.00099
T6	0.00157	-0.00071	-0.00080	0.00119
T7	0.00199	-0.00127	-0.00072	0.00037
T8	0.00162	-0.00098	-0.00064	0.00031
T9	0.00168	-0.00120	-0.00044	0.00020
T10	0.00177	-0.00098	-0.00081	0.00006
T11	0.00132	-0.00106	-0.00017	-0.00051
T12	0.00128	-0.00105	-0.00005	-0.00130
T13	0.00158	-0.00031	-0.00127	-0.00063
T14	0.00107	-0.00013	-0.00096	-0.00074
T15	0.00117	-0.00002	-0.00116	-0.00047
T16	0.00074	0.00010	-0.00087	-0.00043
T17	0.00042	0.00058	-0.00106	0.00036
T18	0.00134	0.00069	-0.00206	0.00013
T19	0.00002	0.00064	-0.00066	-0.00040
T20	-0.00003	-0.00004	-0.00012	0.00025
T21	0.00058	-0.00021	-0.00027	-0.00047
P1	0.00029	0.00066	-0.00095	-0.00013
P2	-0.00071	-0.00006	0.00091	0.00025
P3	-0.00151	0.00104	0.00057	0.00161
P4	-0.00097	-0.00015	0.00072	0.00025
P5	-0.00041	-0.00014	0.00048	0.00059
P6	0.00103	-0.00016	-0.00082	0.00106
P7	0.00140	-0.00028	-0.00110	0.00084
P8	0.00089	-0.00071	-0.00018	0.00060
P9	0.00091	-0.00009	-0.00082	0.00008
P10	0.00055	-0.00002	-0.00055	0.00012
P11	0.00016	-0.00003	-0.00011	0.00038

The transverse strain is observed to be strongly divergent (positive) directly past the grounding zone onto the ocean as the constrained WIS and Byrd glacier spreads out and becomes free floating. Regions of ice convergence perpendicular flow (negative transverse strain) are seen downstream from the CIR and Steershead Ice Rise. A large area of strong negative transverse and positive longitudinal strain rates is seen in the southern margin of

the Byrd Glacier outflow. Outflows from the Transantarctic Mountains converging with the large Byrd outflow created a region of elevated strain rates that continues downstream to approach T7.

Strain rates across the stagnant KIS are close to 0. The lowest velocities on the RIS are upstream from the Steershead Ice Rise and downstream of the KIS. Strain rates remain very close to zero across this area, with very low magnitudes of horizontal compression and vertical thickening compared to the rest of the RIS. Directly downstream from the stagnant KIS across the SCT sites, low rates of longitudinal extension and vertical thinning magnitudes continue.

Measurement artefacts can be seen across the imagery as linear features and high noise areas of both positive and negative strain. SAR imagery is acquired from side view and both spatial resolution and sensitivity to deformation varies in flight- and radar look direction. Although artefacts are present across the entire study area, two significant regions are identified. The first is the calving front, an area of increased transverse strain variability aligned with the flow is present, with a clear linear boundary to the south. Noise is increased across the ice shelf region south of site T18, particularly near the Transantarctic Mountains, influencing remote sensing basal melt estimates. Strong longitudinal extension in bands perpendicular to ice flow appear very similar to the linear artifacts but represent extension crevasses. Large extension crevasses are differentiable as they are higher in magnitude and aligned perpendicular to flow, on a different angle to the satellite track artifacts.

5.2.2 Vertical Strain

The majority of the ice shelf is thinning vertically as the ice undergoes dynamic spreading onto the ocean (Figure 27 and Table 8). 28 of the ApRES sites across the traverse observed strain thinning. Four sites, P2-P5, observed strain thickening near the grounded section of the traverse. The lowest strain thinning was found at T12 with -0.00005 a^{-1}.

Bands of ice shelf thickening are present downstream from glacier outlet margins and ice rises where convergence thickening occurs at suture zones. The most prominent suture/convergence zones include those downstream of the CIR, Steershead ice rise, and the Byrd outflow margins. Ice rises, ice rumples, and grounding zones are also sites of strain thickening, seen at the Siple coast pinning points and upstream of White Island and Black Island near the start of the traverse.

The region downstream of the KIS features observable low rates of strain thinning with very low-velocity rates.

5.2.3 Satellite Strain Product Comparison

The vertical strain results from the various MEaSUREs data products agree with each other in sign and magnitude as the MEaSUREs datasets use similar methods and data products to acquire their velocity fields. As strain is derived from the velocity derivative, minor variations in the velocity field can significantly impact the calculated strain rates. The standard deviations error from values within the 3km radius of the smoothing kernel show a higher degree of uncertainty with error bars often extending into both positive and negative strain.

The satellite-derived products show the highest variance across the area of sites T18 to P5 (Figure 28). These sites were in areas of high noise and measurement artifacts resulting from reduced satellite acquisition at high latitudes. This is combined with more complex regimes in ice dynamics at sites P2-P5 with higher proximity to grounding zones. While the KIS sites (P7-11) are still at high latitudes where data acquisition is reduced, the low-velocity zone results in a less absolute error, even though the proportional error of ice velocities will remain high.

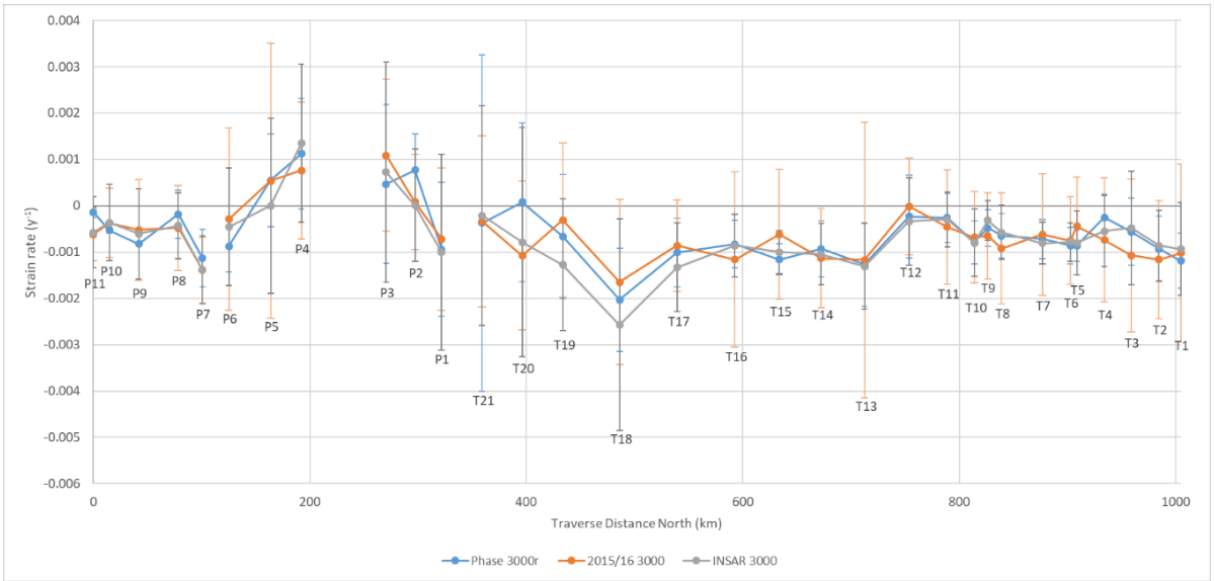

Figure 28. *Vertical strain rates derived from different MEaSUREs velocity products using the same processing methods. Only datasets with complete coverage of the RIS were included: Measures Phase-Based, INSAR and 2015 Annual Velocity. Error bars represent the standard deviation of the strain rates from the 3000m radius surrounding the point.*

Strain rates from the 2015 annual velocity data contained the highest error at most sites due to a shorter acquisition period and fewer images to determine the ice velocity. The longer acquisition period averages of the satellite datasets create more reliable averaged velocity data, but low interannual variation is expected. The 2015 annual velocity field was the only yearly measurement with complete spatial coverage of the ice shelf. The 2014 and 2016 datasets did not include coverage of sites T18 to T21 and P1 to P11 and featured larger noise artifacts, so they were excluded from the study.

5.2.4 ApRES to Satellite Product Comparison

The MEaSUREs satellite-derived strain rates displayed strong agreement with the ApRES measurements of vertical strain across most of the traverse, and radar-derived strain rates are well within the satellite-derived error bars (Figure 29 and Figure 30). The error was estimated using the standard deviation of strain values within the 3000m radius of the lowpass filter. The close correlation of the two datasets suggests the satellite error may be overestimated by the the standard deviation.

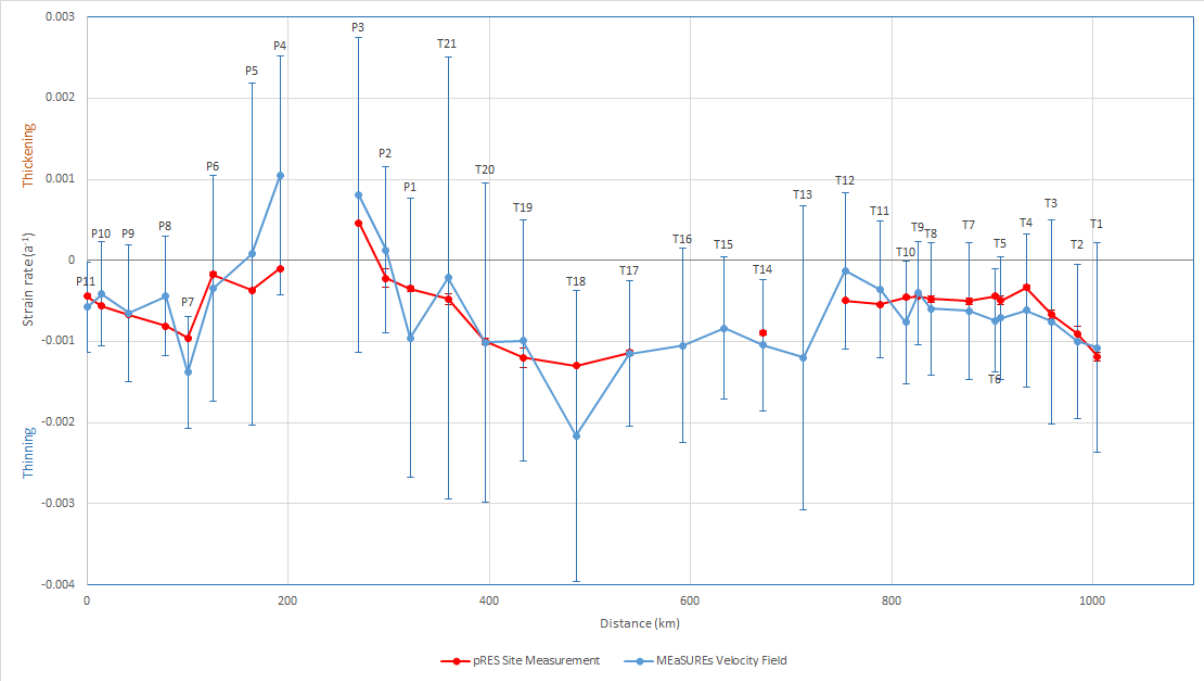

Figure 29. *Vertical strain rates determined by ApRES and satellite-derived velocity fields at each site plotted against the traverse distance. Satellite error bars represent the standard deviation of the strain rates from the 3000m radius surrounding the point. ApRES error bars are from the strain model error.*

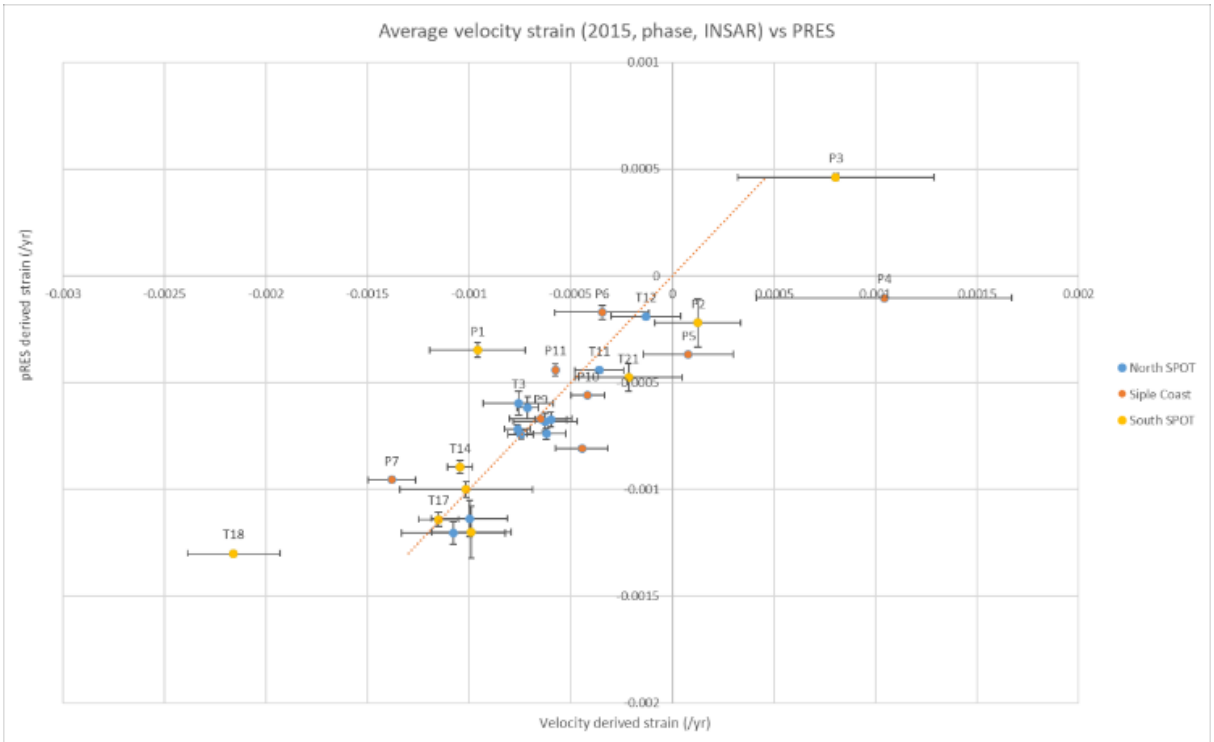

Figure 30. *Correlation between ApRES and satellite observed vertical strain rates. The orange line represents the 1:1 line. Velocity derived strain rate errors represent the standard deviation of the low-pass filtered data in a 3x3 km box around the ApRES site.*

The first is sites P2,4 and 5, near the CIR upstream grounding zone, determined strain thinning at locations where satellite measurements determined strain thickening. This region of satellite strain thickening was also present in Das et al. (2020) and with a lower magnitude and regional extent in Moholdt et al. (2014). Despite incorrectly correlating the direction of vertical strain across these regions, the ApRES measurements were within the error bounds of the satellite, and both vertical strain rates agreed that the magnitude was close to zero. Both measurements identified P4 as a site of strain thickening.

The second area with a major difference between the two datasets is at T18. While both datasets measured the highest strain thinning rate, the satellite strain estimated nearly double the strain thinning rate as the ApRES site. However, the ApRES measurement at T18 had a perfectly linear strain fitting and a very low error.

5.2.5 Shear Strain Rates

Regional shear strain is displayed in Figure 31, with right-lateral shear as positive values and left-lateral shear as negative values. The highest shear strain within the study extent occurs at the lateral margins of grounded glaciers and ice streams. Ice shelf shear strain is relatively low in comparison. The shear strain rate at each ApRES site is displayed in Figure 31. The

highest shear strain rates occurred at sites T5, T6, T12, P3 and P6. P3 is the site with the highest value of shear strain situated close to the grounded ice at the lateral margin of ice diverging around the CIR. The remaining sites are situated at the margins of glacial outflows.

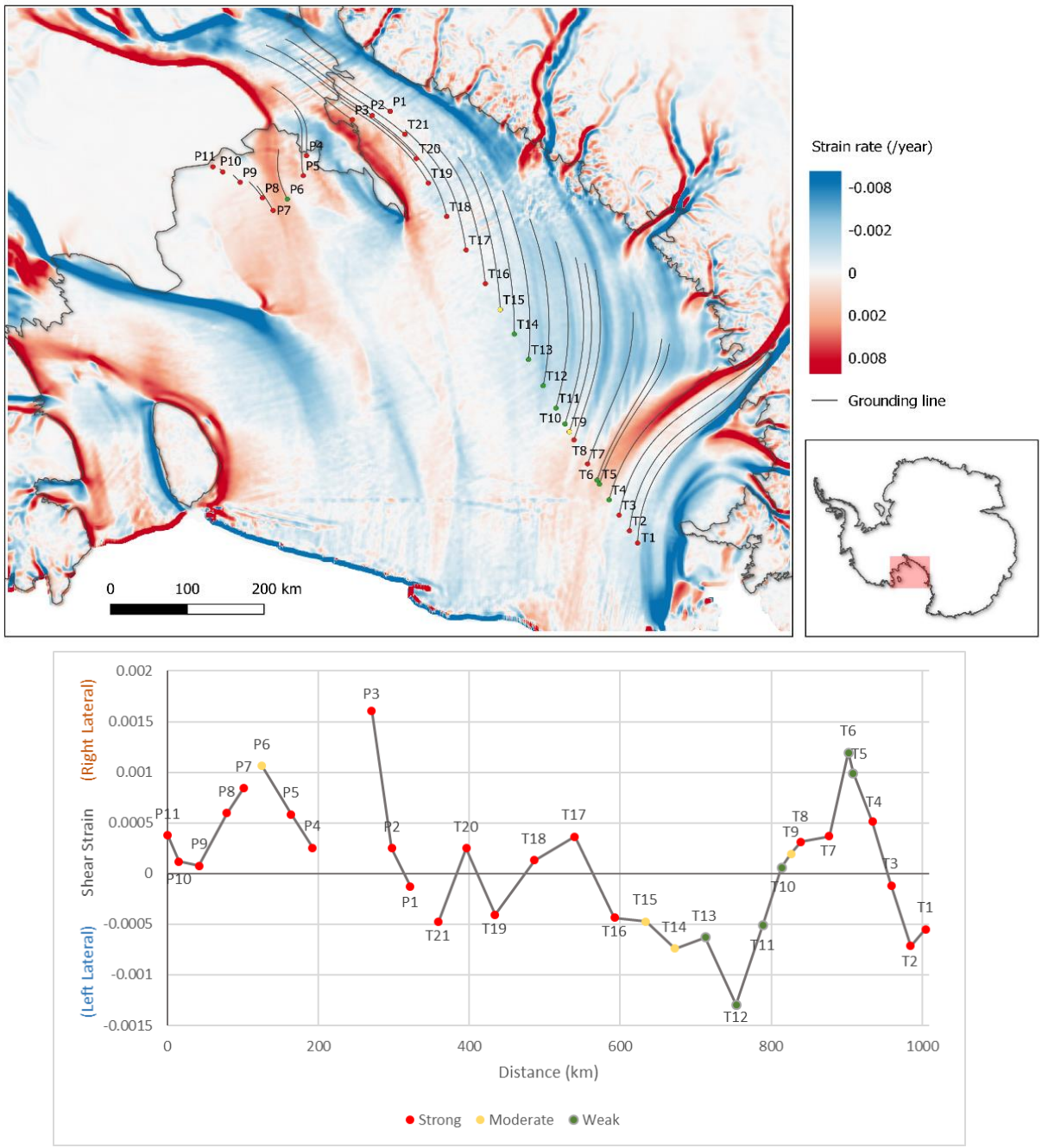

Figure 31. *Shear strain rates across the RIS from MEaSUREs Phase-Based Velocity Map (above). The cross section of sites along the traverse plotted against distance (below).*

High shear strain rates can be seen at the margins of glacier/ice stream outflows and continue downstream of the outflow margins with significantly different velocities from the surrounding ice or outlets. Long bands of shear strain are present across the Western RIS, where numerous small glacier outflows with varying velocities are adjacent to each other. The higher proportion of left-lateral shear zones on the east RIS comes from ice rotating north after exiting the neck behind the Crary Ice Rise. This large outflow predominantly from the WIS rotates EAIS glacier outlets eastward after leaving the grounding zone. This appears as short zones of high right-lateral shear on the true right of the outflow. The linear bands of shear stress decrease in magnitude as they approach the ice shelf's centre as ice shelf stresses and ice velocity homogenise. Shear strain is very close to zero for areas distant from grounded ice in the central regions of the ice shelf and the calving front. The SPOT is located consistently to the north of the bands of increased shear strain. The McMurdo Shear Zone to the north of T1 contains the traverse's most significant crevasse region and requires engineering work to maintain the road.

6 Discussion

The spatial pattern of the basal mass balance across the RIS has been previously estimated from either oceanographic modelling (Timmermann et al., 2017) or satellite data analysis under steady state (Rignot et al., 2013) and non-steady state assumptions (Moholdt et al., 2014). The former is limited by the lack of direct cavity observations to validate results. The latter requires an accumulation map as input from other sources. In this chapter the findings from this new ApRES analysis are discussed in reference to these previous results. Also discussed are the radar waveforms from earlier results, in order to draw conclusions about the internal structure of the ice shelf and the potential variability of the basal mass balance of the RIS.

6.1 Basal Reflection Characteristics

The spatial and temporal variability of basal melting and freezing at the Ross Ice Shelf is not well known. It is known that the marine ice layer is thin and melt rates in the central regions are expected to be relatively low. The unintrusive ApRES basal reflections strength is used to interpret the interface occurring at the ice shelf base. Strong basal reflections are created by consistent basal melting due to the high dielectric contrast of the meteoric ice to ocean mediums. The weak and diffuse basal reflections indicative of marine ice or debris scattering are present across the central SPOT traverse on ice from EAIS glaciers. The spatial distribution of weak reflections closely correlates to the low radar reflection coefficients measured for the first time more than 40 years ago (Figure 32)(Neal, 1979) and more recently with the ROSETTA survey (Tinto et al., 2019). The link to EAIS outlet glaciers may indicate a correlation with entrained sediment and meteoric ice thickness variations between the various ice sources. Some of these areas are also regions with preferential basal freezing.

Most sites remained either consistently strong or weak in reflected radar amplitude over continuous years. Sites that showed the most variability were the moderate sites between regions of strong and weak reflection waveforms (T8 to T9, and T13 to T15). Reflection change may be attributed to changes in basal morphology or temporal variations in cavity circulation. As radar waves cannot penetrate more than a few meters into seawater due to the high conductivity, the reflections seen in radar profiles following the basal reflection are caused by off-nadir structures and multiples of the radar signal. The reflection amplitudes will decay following the basal reflection peak and were not used in the analysis. A double peak directly after the basal reflection was interpreted as off-nadir reflections near the radar footprint, for example, due to a strong reflector such as crevasse. The regions of strong basal reflections include much of the north and south SPOT and the SCT, where wide ice streams of a more homogenous structure enter the ice shelf and mode 1 melting is occurring near the grounding zones.

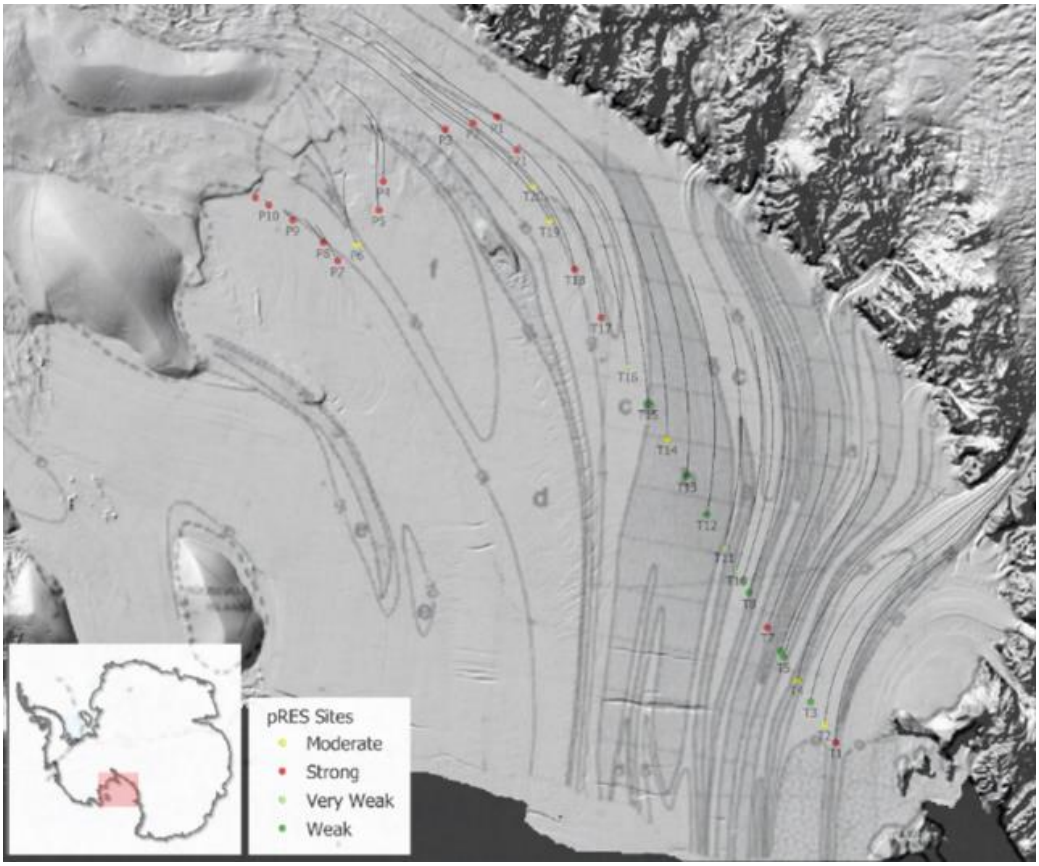

Figure 32. *ApRES basal reflection strength (as Fig. 6) plotted with radar reflection coefficient from 1970's airborne observations. Dark grey areas have lower reflectivity (adapted from, 1979).*

6.2 Ice Shelf Thickness

Accurate measurements of ice shelf thickness change improve the understanding of total ice shelf mass changes. Changes to ice shelf mass are important for predicting changes to the backpressure exerted on the grounded ice sheet, particularly in the case of the marine grounded WAIS. Point thickness measurements from ApRES are not spatially extensive, but they do provide precise measurements of entire ice column thickness with fewer corrections required than satellite freeboard measurements. Therefore, they can be used to validate wider databases of ice shelf thickness, such as BEDMAP2, alongside airborne RES, seismic and altimetry measurements. Validations from borehole measurements are rare and expensive and potentially not representative.

ApRES ice shelf thickness closely matched the trend of the BEDMAP2 record of ice shelf thickness interpolated from satellite altimetry (Griggs & Bamber, 2011) and found consistently thicker ice across most sites except those underlaid by marine ice or basal debris (Figure 3). This difference was most notable over the northern and southern areas where basal melting was present. The measured Siple Coast sites downstream from the KIS

showed consistently higher thickness compared to BEDMAP2, with the highest thickness increase at the location closest to the grounding line (P11). While T8 and T9 matched BEDMAP2 well with strong basal reflections, higher thicknesses were measured at the northern sites across T1 to T7. Interannual variability was highest for sites with diffuse and unclear basal reflection amplitude peaks such as T6, T10 and T11. Sites with strong basal reflections displayed much less variation across measurements. Sites T2 and T3 showed higher interannual variability compared to BEDMAP2, despite consistent ApRES thickness measurements within 1m each year.

As these ApRES measurements were made 5-10 years after the satellite altimetry measurements, they may show changes over the last decade. However, incorrect assumptions of uniform ice shelf density may also cause this variation. Overestimating the bulk density of ice would result in smaller freeboard to thickness conversion for BEDMAP2. Overestimating bulk density of firn densities would result in slower wave speed (Equation 4.3) and an overestimation of ApRES thicknesses given the same TWT (Equation 4.4). Better understanding of bulk ice and firn densities would reduce this uncertainty (Ryan, 2016). BEDMAP2 measurements have been interpolated across the RIS area, so they will not have the same precision as ApRES at the field sites.

The region of lower ApRES thickness at sites weak basal reflections T9 to T14 means the basal reflection measurements are likely picked above the true ice base. For weak reflection locations the highest amplitude peak across the basal reflection range was used to estimate the ice thickness. This interpretation comes with larger uncertainties than the measurement error and is likely to underestimate the true ice shelf thickness. The reduced thickness is attributed to increased scattering of radar energy above the basal layers from higher conductivity and attenuation of basal debris and possible marine ice, creating a peak amplitude above the true base. The extent of reduced thicknesses across six sites suggests similar processes are occurring across the sites.

At T12, a 70m unit of basal debris in bubble-poor ice has been observed in the HWD-2 borehole (Stevens et al., 2020). The upper interface was a sharp but irregular boundary not parallel with the surface. However, when analysing the ApRES radar profiles using the directly observed pressure depth measurement of 370m, no single basal reflection signal could be identified. The basal reflection signal was masked by higher attenuation and reflections of the basal debris.

The three sites located in glacier margins and suture zones (P6, T4 to T6) all displayed significantly higher thicknesses than the BEDMAP2 dataset. The highest deviations from BEDMAP2 occurred at sites T4 and P6. The ambiguous 'moderate' basal reflections of these sites may indicate a complex basal roughness or the strong reflections from off-nadir basal topology, resulting in the appearance of elevated ice thicknesses. In this instance, melt rates calculated at these sites may be measuring melting in crevasse structures and not a flat base. A uniform firn correction 7m was used across the radar sites to account for lower

densities of firn. The higher thicknesses measured relative to altimetry methods would be improved by more knowledge of spatial variability of ice shelf bulk densities and firn compaction processes. For altimetry measurements, improved knowledge of the earth geoid would also improve the altimetry freeboard thickness measurements.

6.3 Basal Melting Regimes

The traverse survey includes a vast area, covering many different glaciological origins and oceanic influences, often with 30km between measurement points. This distance makes linking direct or linear relationships between sites tenuous where there is known glaciological heterogeneity. However, for interpreting the large-scale trends and processes across the RIS, simple linear trends between sites have been included to clarify changes between sites. Geographic regions have been grouped to analyse local processes driving the regional melt pattern.

Siple low melt zone

Melt rates across the Siple Coast low melt zone are low in view of the strong ApRES basal reflections across these sites. Strong basal peaks and correlations of internal layers support the precision of the ~0.01m a^{-1} melt rates measured. The pattern of low melt rates across the region, with an exponential increase of melt rates towards the KIS grounding line, supports the current understanding that low basal melting dominates the eastern RIS area, with calving being the major contributor of mass loss (Rignot et al., 2013).

Upstream of P11, summer basal melt rates increased exponentially with the approach towards the grounding line, reaching an order of magnitude higher than the RIS area average and those measured at P11 (H. *Horgan, pers. comm.*). Summer ApRES melt rates 4 km upstream from P11 were 0.1-0.2 m a^{-1}. The similar magnitudes suggest summer melt rates closely approximate the annual melt rate and have minimal seasonal variability within this region. Low influx across the KIS grounding line does not balance strain thinning, surface accumulation and basal melting. Low basal melt rates across the Siple Coast may be a response from the ongoing ice shelf thinning (Figure 23). Surface expression of ice thinning across the grounding zone from reduced flux is present in elevation models as an increase in slope parallel with the grounding zone (Howat et al., 2019). With the assumption of steady-state conditions or approaching steady-state conditions, lower basal melt rates are expected. Any significant melting will be reduced to a narrow band along the grounding line.

Melt rates slightly above 0.01m a^{-1} were measured at sites P4 to P5. Sites P4 to P6 are aligned perpendicular to flow over a complex ice dynamics region with variable strain rates close to zero. P4 and P5 are located at regions of elevated bathymetry near the grounding zone, with an interpolated cavity depth of less than 5m (

Figure 5a) (Fretwell et al., 2013; Tinto et al., 2019). The moderate basal reflection at P6 is situated in the suture zone downstream of a prominent headland. While the change in the basal reflection was able to be determined, the basal melt rate calculated was very close to zero and smaller than the error. The melt rates at P11 are an order of magnitude higher than at P4, despite similar ice thicknesses (~550m), cavity thicknesses (1-5m) and distance from the grounding zone. P4, however, has a much higher ice velocity and is more complex. Both sites display similar cavity thicknesses at their locations, and improved bathymetry models show that P11 has a more open cavity to the north (Tinto et al., 2019). Small cavity thicknesses with flat bathymetry of several tens of meters have been proposed to undergo tidal mixing that lowers basal melting rates compared to a stratified water column (Holland et al., 2003). However, borehole measurements around the WISSARD determined a stratified water column within 5km of the grounding line and 10 m depth (Begeman et al., 2018). Compared to most grounding zones, these remain low melt rates barely above the RIS wide average of 0.2-0.3 m a^{-1}. HSSW descending into the ice shelf cavity is considered the major contributor to basal melt at grounding lines as mode 1 melting (Jacobs et al., 1979; MacAyeal, 1984). HSSW flow is mainly confined to the western RIS (EAIS side) cavity, prevented from intruding into the eastern cavity by the elevated bathymetry and smaller cavity depth (Tinto et al., 2019). The isolation of the cavity from the outside ocean and tidal mixing are thought to cause the consistent low melt rates across the Siple Coast area.

Southern high melt zone

The southern SPOT is a remote region with few ground-based measurements. Sites T20 to P3 are located on ice contained between the CIR and the Transantarctic mountains. The grounded ice on each side slightly limits the amount of gravity-driven spreading until the ice passes the CIR. Locations T18 to P3 originated from the WIS with very similar flow paths to the modern velocity field (Figure 6), and sites T19 to P1 have similar cavity depth of 100m.

The melt rates at sites T20 to P3 were slightly higher than the 0.1-0.2m a^{-1} average RIS melt rate. These were higher than anticipated for an area away from a grounding zone, and the strong basal reflection signals inform a melt signal. Melt rates increased away from the grounding zone at P3, towards the embayment centre at site P1, ~50 km from the coast. Increasing melt rates away from the grounding line was also observed along a 20 km transect inside a small embayment 60 km to the south of site P3 (Begeman et al., 2018). Melt rates at sites T21 to T18 decreased to the north as ice reduced in thickness. Vertical strain thinning rates continue to increase in the same direction, contributing to an increasing proportion of ice-shelf thinning. Increased base elevation causes pressure melt temperature to increase and further reduce melt rates (Jenkins & Doake, 1991). Cold ISW from melting and mixing in the upper cavity would explain the decrease in melt rates.

The difficulties of melt calculations at thick sites come from the vertical strain determination and basal range change at depth. The ice column thickness (600-700m) and annual measurement period meant correlation of internal layers for a linear strain fitting was

possible to 300-400m depth at most sites. Basal thickness changes greater than the radar wavelength resulted in half-wavelength ambiguity when determining precise basal thickness changes. For example, P1 produced two different observed thickness changes of 0.25m and 0.5m. This difference in observed thickness range change resulted in melt rates of -0.03m a^{-1} and 0.28m $a^{-1,}$ respectively. The raw basal range without phase-sensitive techniques supported the 0.5m basal range change. Shorter periods of repeat measurement to accurately determine the strain rate at sites with 600-700m ice thickness would improve the understanding of this area.

Basal mass balance rates had higher spatial and magnitude variability south of the CIR, with bands of higher melt rates and freezing rates than the RIS centre (Moholdt et al., 2014; Rignot et al., 2013). The wide-scale and multi-year remote sensing observations did not identify the exact extent of the 0.2-0.3 m a^{-1} basal melt rates of the Southern Spot Melt Zone. However, basal mass balance error started at 200 kg m^{-2} a^{-1} (Moholdt et al., 2014; Rignot et al., 2013). Only T21 exceeded this value, with a basal melt rate of 262 kg m^{-2} a^{-1}. While this may indicate a regional shift in melting regime and oceanic conditions between the study periods, it is proposed that the higher variability basal melting and freezing may resolve to lower melt rates over a wider area. Spatial resolution is not thought to play a part as the point locations show consistent melting patterns, unlike the patchy distribution of the satellite studies. The higher noise and variability of strain rates across the southern ice shelf may contribute to some of the increased variability of basal melt rates. Surface accumulation rate is the other key assumption within these studies proposed to explain this variability.

The ApRES determined a significant increase in vertical strain thinning rates from T21 towards a maximum at T18. The variance in divergence rates from Moholdt et al. (2014) may result in overestimating strain thinning rates and underestimating the melting component. Transient dynamic changes in ice shelf thickness do not impact shorter-term studies that directly measure strain change. The multi-decadal studies recognise this as a potential source of inaccuracy, causing an area of apparent high melt area near T17 to T18 (Figure 33)(Das et al., 2020). Nearby ApRES measurements did not find evidence of basal melts higher than 0.02m a^{-1} in this area over 2018-2019.

Weak central zone

Across the Central SPOT, two different basal characteristics have been identified. Strong/moderate reflections with low melt rates ~0.01-0.02m a^{-1}, or weak and diffuse basal reflection ranges. These strong basal reflections zones with low basal melting were limited to sites T7 to T9 and south of site T16. Here basal reflections increased from moderate to strong while maintaining low melt rates seen across this region. Across this southern zone, moderate reflections become consistent with thicknesses below 400m and weak basal reflections appearing at ~350m (Fretwell et al., 2013).

Two zones featuring weak basal interfaces across the central section (T5 to T6 and T10 to T16) were interpreted as the result of accreted marine ice or basal debris from Transantarctic Mountain glacier outlets. While internal layers could still be used to interpret the strain thinning at these sites, the weak basal reflection signature prevented the identification of basal changes required to calculate melt rates. The high attenuation of marine ice makes differentiating any changes to the marine layer difficult and basal freezing rates or thicknesses cannot be interpreted from these radar measurements. With marine ice and basal debris creating very similar radar waveforms, it is difficult to determine if the basal mass balance is positive or negative for sites in this region. It is interpreted to have either an unquantified amount of marine freezing with low basal melt rates in the order of 0.01 m a-1 or ephemeral variations between both regimes as determined by oceanographic data HWD-2 (T12) (Stevens et al., 2020).

Validation of ApRES basal mass balance at site T12 with HWD-2 borehole measurements was not possible due to the 60m layer of basal debris. No single basal reflection showed significant characteristics that would isolate the basal interface. The HWD-2 borehole revealed a complex basal condition that included a layer of marine ice several centimetres thick underlying a thick layer of basal debris. The CTD measurements at the base indicated a melting regime. The ApRES measurements across the Central SPOT reflection zone supports the current understanding of very low basal melt rates or basal freezing across vast regions of the central RIS.

North high melt zone

The pattern of annual melt rates across sites T1 to T3 during four years of measurement show reliable interannual basal melting. The sites located on the Byrd Glacier outflow are discharging ice at the highest velocities across the ice shelf and the shortest residence time on the ice shelf.

Sites T1 to T3 are located near the edge of a melt region linked to the seasonal inflow of AASW produced by solar-heated surface water in the Ross Sea polynya (Rignot et al., 2013; Stewart et al., 2019). The AASW is modelled to intrude as far south as Mina Bluff (Tinto et al., 2019), with influences of basal melting reducing exponentially south towards the T1 site (Stewart et al., 2019), where the closest summer melt rates measured 30km north of T1 remained over 1 ma^{-1}. While modelled AASW flow did not extend to cover sites T1 to T3 (Tinto et al., 2019), elevated melt rates extending across the Bryd Outflow have been estimated from remote sensing methods (Figure 33, Figure 34 and Figure 35)(Das et al., 2020; Rignot et al., 2013). As the ApRES thickness measurements found increasing thickness from T1 to T3 (Figure 18) and decreasing melt rates, this may represent the furthest influence of Mode 1 melting.

The temporal melt variability appears to be relatively consistent, but no site with multi-year measurements was able to resolve the melt rate for all individual years. The two-year-long

analysis covered missing data points, and as a longer-term average made determining interannual variability difficult. Where multi-year analysis was possible, melt rates generally remained consistent within 0.1-0.2 m a^{-1}. The significant outlier is T1 in 2017, where a significantly higher thickness change was observed. The divergence of this measurement from long term two-year measurement and the pattern of slightly elevated melts for other sites suggests it may be an overestimation of an elevated melt year.

6.3.1 Comparison to Large-scale Data Sets and Models

Annual survey measurements of site locations give a beneficial intermediate temporal resolution of melt rates, excluding seasonal variability (where applicable in the northern region) while allowing analysis of interannual variability and comparison with long term studies. Across the 1000 km, only a few sites (T21 to P2 and T1 to T2) in localised melt zones exceeded the 0.1-0.2 m a^{-1} average basal melt rate for the RIS (Depoorter et al., 2013; Moholdt et al., 2014). Basal melt rates across the central RIS were at least an order of magnitude lower than the ice shelf wide average found in other studies. Spatial patterns of basal melting were also consistent with oceanic models with regions of low basal melt rates or freezing across the central region of the RIS and much higher melt rates south of Ross Island and near the WIS grounding line south of the CIR (Timmermann et al., 2017). However, basal melt rates appear to be overestimated by up to 1m in the northern sites T1 to T3.

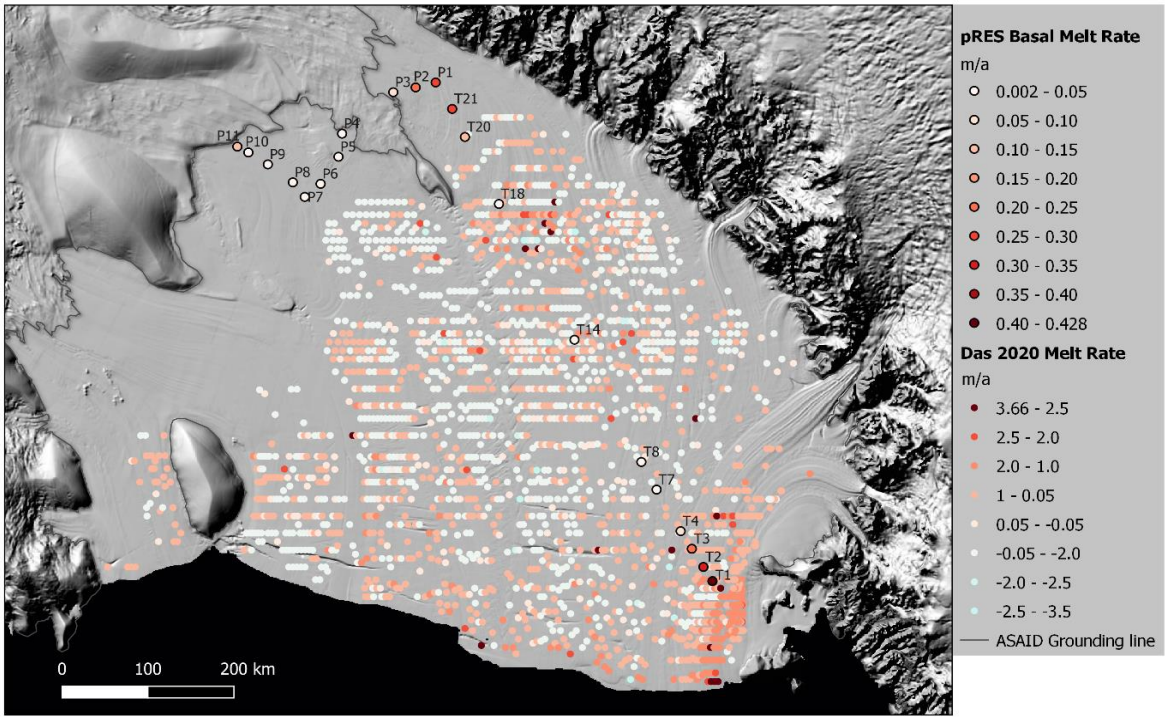

Figure 33. *Comparison ApRES measurements with widescale, multi-decadal melt rates from Das et al. (2020).*

(a)

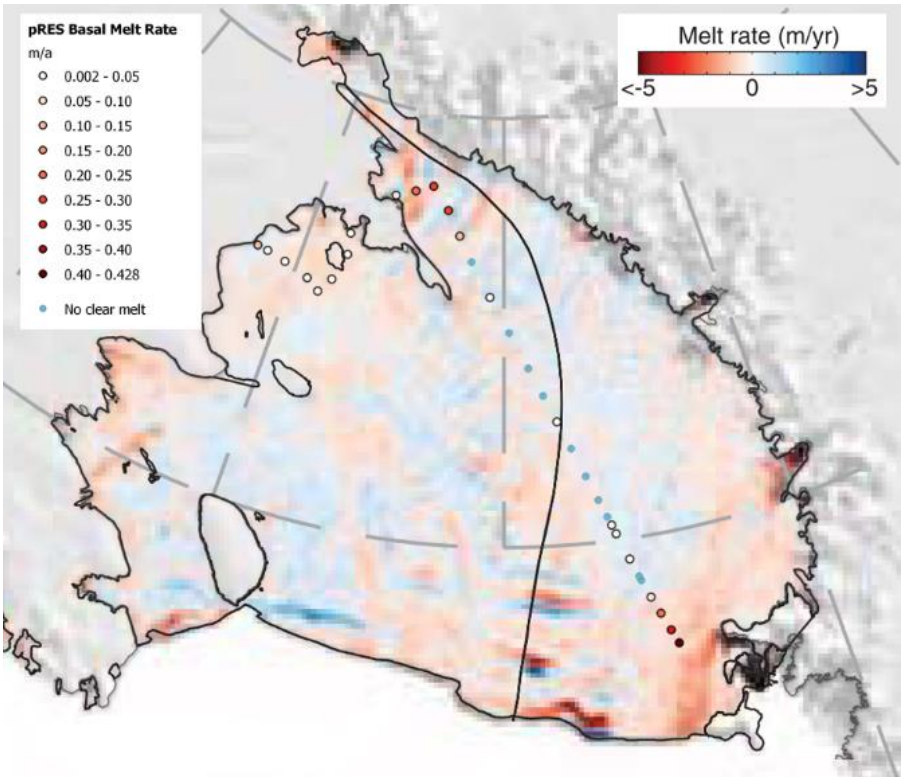

(b)

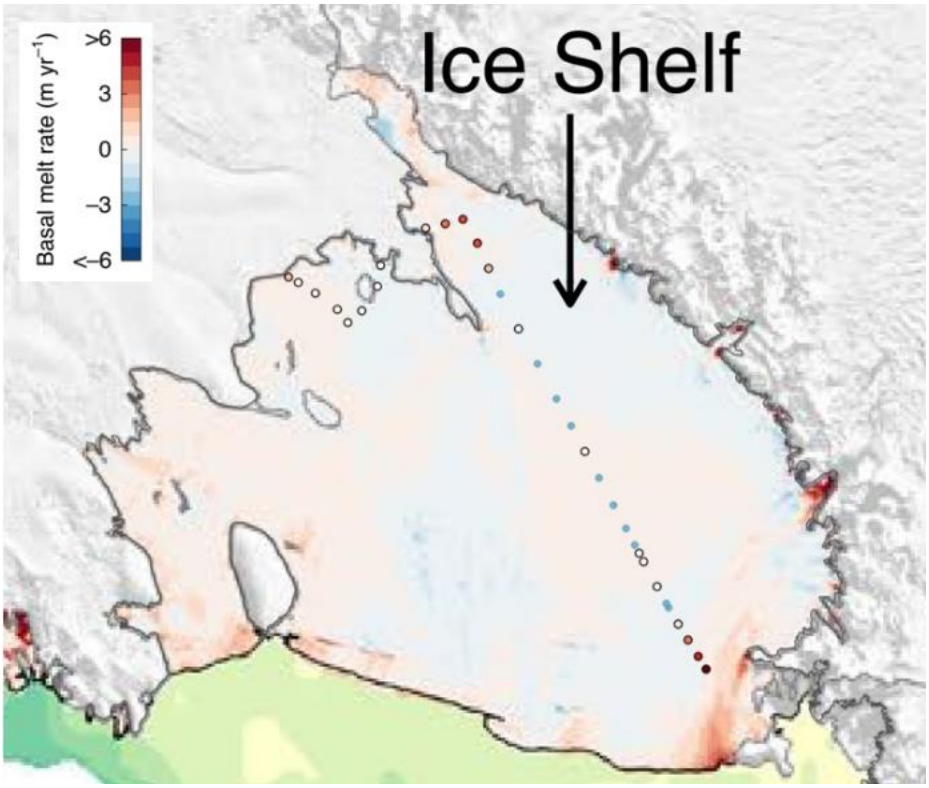

Figure 34. *ApRES comparison with RIS Basal Melting adopted from (a) Rignot et al. (2013) and (b) Adusumilli et al. (2020).*

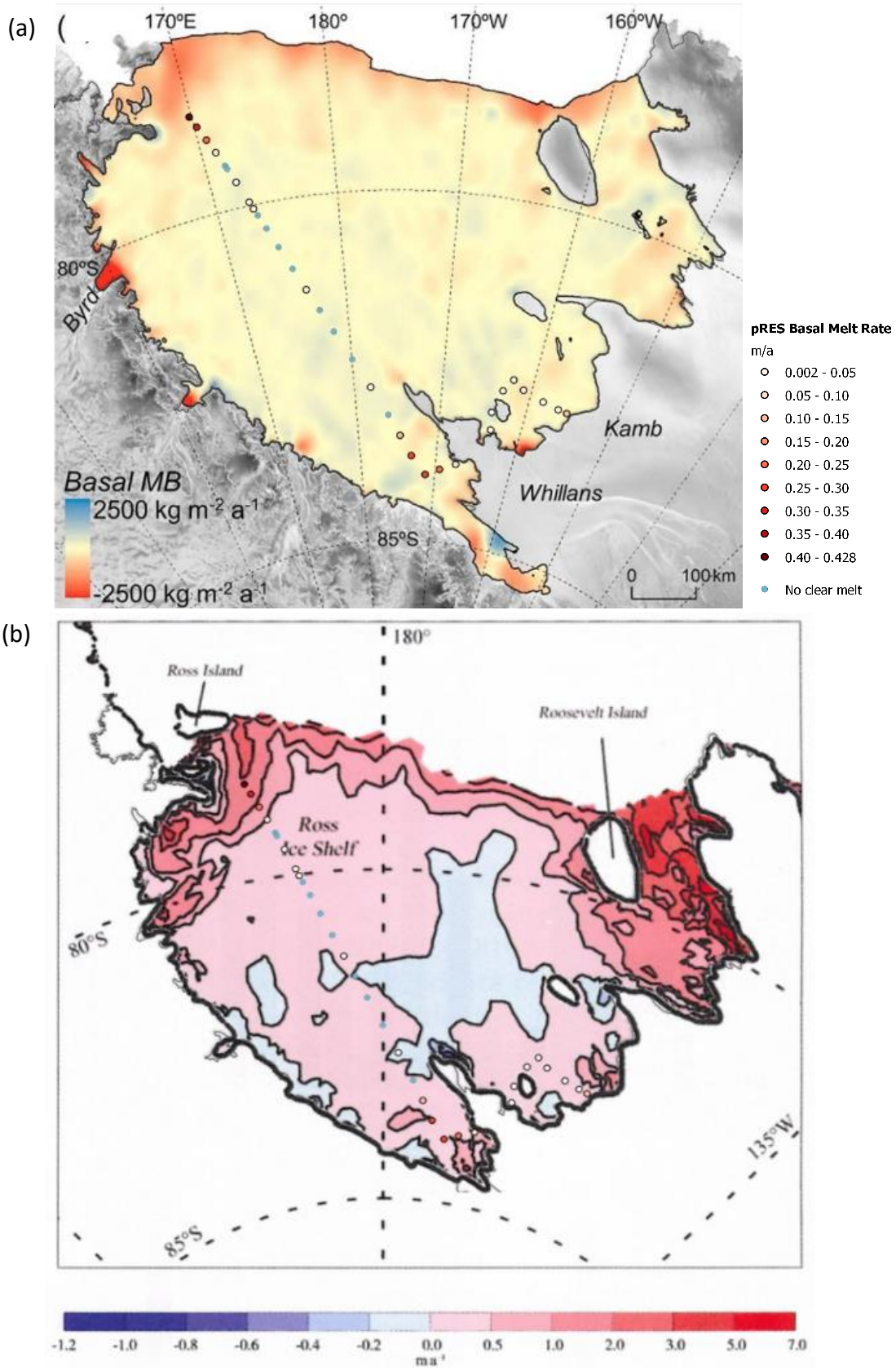

Figure 35. *ApRES comparison with RIS Basal Melting adopted from (a) Moholdt et al. (2014) and (b) Timmermann et al. (2017).*

The agreement of low magnitude annual measurements across the central regions with long-term remote sensing studies supports the current understanding that the RIS is close to steady-state conditions (Depoorter et al., 2013; Moholdt et al., 2014). As most ApRES measurements only have two years of measurements the annual variability and trends of interior melt rates cannot be resolved. Until future surveys are completed, they remain a precise baseline for analysing future variability, resolving basal melt within ocean cavity models, and supporting remote sensing studies overlapping with this acquisition period. As the results concur with steady-state expectations of low melt rates with small amounts of basal freezing across the central section of the RIS, the central RIS is determined to still be maintaining steady-state conditions. The spatial extent of these ApRES measurements provides a baseline for assessing future changes to melting regimes and cavity processes across the RIS. These could manifest through changes to the basal melting rates of the central region or ISW production, changing the spatial distribution of marine ice.

The low melt rates across the Siple Coast Zone illustrate the lower basal melt loss across the eastern RIS and larger regions of basal freezing due to the bathymetry restraints and higher proportional calving mass loss (Rignot et al., 2013; Tinto et al., 2019).

6.4 Large-Scale Vertical Strain Distribution

ApRES vertical strain rates have been directly compared to strain values derived using the MEaSUREs dataset and other studies of vertical strain to determine their accuracy (Figure 36). Despite some variation in the southern areas, ApRES strain rates are in good agreement of satellite strain despite the challenge of detecting precise velocity rates of change over a vast, featureless area.

Surveying such a wide extent of the RIS for vertical strain rates presents the opportunity to compare with vertical strain rates derived from horizontal divergence across the entire RIS. Such products are used for estimating basal melt rates from satellite altimetry when combined with surface mass balance from climate models or steady-state assumptions (Das et al., 2020; Moholdt et al., 2014; Rignot et al., 2013). While the most recent MEaSUREs velocity product had the best individual correlation to the ApRES data, the average product provided the best overall correlation with the dataset. Site T18 featured the highest strain thinning rate of both datasets, but also the highest variance between them. At T18, the satellite velocity measurement was on the border of two separate satellite acquisition areas, which may have overestimated the strain thinning. At T4 and T5 close to the grounding zone, satellite-derived strain estimated strain thickening, while ApRES strain recorded strain thinning. This suggest satellite strain is not well defined around this complex grounding zone upstream from the CIR that may explain some of the variation in basal melt estimates across this area.

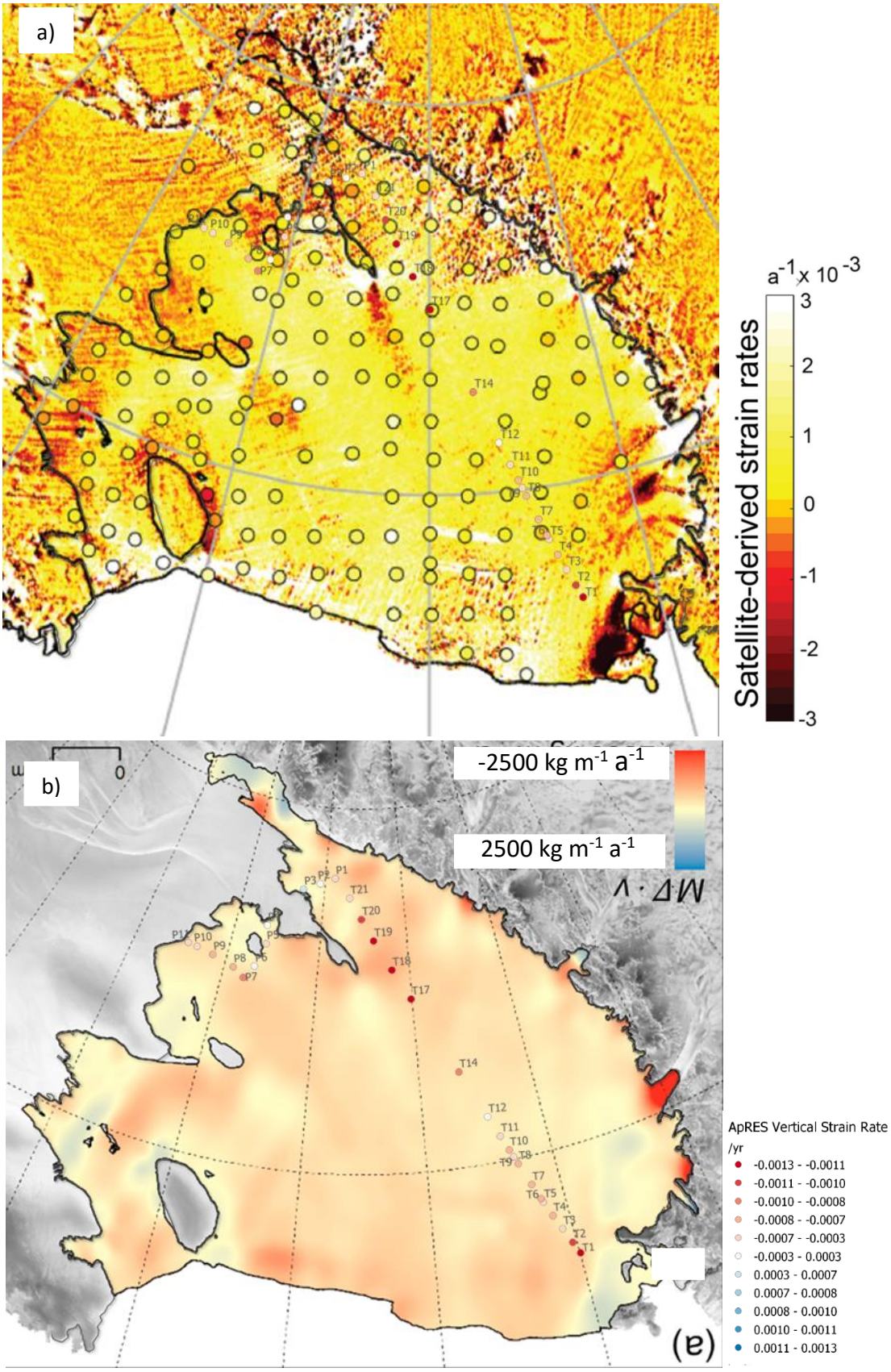

Figure 36. *ApRES vertical strain comparison with RIS vertical strain adopted from (a) Das et al. (2020) and (b) Moholdt et al. (2014).*

The good correlation between MEaSUREs derived strain rates and ground based ApRES measurements gives greater confidence in the accuracy of other satellite studies of vertical strain and basal melting. This study only looked at deformation below the firn transition boundary. A future study of ApRES measurements to include the firn compaction rates acting alongside the strain thinning in the upper layers would provide additional validation. Spatial variability of accumulation rates remains the major uncertainty for satellite observed basal melting results.

6.5 Satellite-Derived Horizontal Shear

While the shear strain is not required directly for vertical strain rate calculation, it is used to interpret the present and historic internal deformation within the vertical column of the ice shelf ApRES sites. High shear strain rates are a potential cause of incoherence of internal layers over time, particularly for the continental meteoric ice units. Lateral shear strains are not expected to tilt the horizontally deposited LMI for the application of the ApRES detecting internal layers. Lateral shearing of horizontal units may alter the thickness or fabric of the internal layers. It is hypothesised that the tilting of the layer orientation should be minor and not alter the signal of vertical strain too much.

The continental meteoric ice unit has a more complex internal deformation history from topographic stresses of grounded ice streams or glaciers. When combined with the vertical strain thinning of ice shelf extension, additional horizontal shear strain is expected to increase the error of the vertical strain estimates of the ApRES application.

Most bands of shear strain from the differential flux of the EAIS outlet glaciers appear to end upstream of the SPOT logistics route. This likely results from the logistics planning to take the most direct route from McMurdo Crevasse Zone to the Leverett Glacier, which happens to avoid crevasse zones resulting from shearing ice. As most ApRES sites are positioned in zones of very low shear strain, it is not anticipated to impact the interpretation of the modern dynamics of the ice column. However, understanding shear strain rates and deformation history of ice has still been considered when interpreting the ApRES measurements. The 450m resolution of the velocity product may underestimate the highest strain rates located at the shear margins with grounded ice. They do provide a suitable resolution for applications in the central ice shelf where shear strain rates are lower from large scale flow regimes.

This method of strain thinning calculation assumes all velocity deformation is plastic, with no mechanical failure or fracturing. This assumption is suitable for this study in the central region but will include fracturing as total strain where shear zones or rifts are present. The extension crevasse systems near the calving front appear as strong linear bands of vertical thinning and longitudinal extension rates perpendicular to the ice velocity. These crevasse features are visible on the REMA base map (Figure 27). It is incorrect to define the crevasse features as undergoing strain changes as extension fracturing of the ice shelf is exhibiting

mechanical failure of the ice. The rate of change will remain conserved - the larger the apparent strain extension is, the faster the fracture is extending in the direction of flow. The series of extension fractures show different thicknesses of longitudinal extension, decreasing as the fracture approaches the coast, indicating this strain field is measuring the higher growth rate of the newer fractures.

7 Summary and Outlook

Ice shelves are the most vulnerable part of the ice sheet system to environmental changes and warming oceans. The extent and thickness of the ice shelf play a role in regulating the flow of grounded ice into the ocean through buttressing, preventing the acceleration of sea-level rise. Oceans absorb most of the heat from atmospheric warming and ice shelves will be the most responsive part of the ice sheet to environmental changes within the Southern Ocean. Antarctica's ice shelf cavities remain mostly unexplored with very few direct measurements. Geophysical surveys enable accurate glaciological measurements of the ice shelf to interpret the impact of environmental processes.

The ApRES instrument provides unprecedented precise measurements, however, the time required for each measurement limits the device to surveying point locations. The limit of effective single ApRES repeat measurements was found to be effective up to 2 years apart and the shorter year-long measurement period allow examination of interannual variability. This makes ApRES excellent for precise point measurements of strain and basal melting to validate the reliability of wide-scale remote sensing analysis. Remote sensing studies have lower precision, longer acquisition periods and require many corrections that introduce uncertainties to be validated. However, they are able to measure massive extents of ice shelf and determine overall ice sheet system mass balance trends.

Precise ApRES measurements of the ice shelf base have never been used before to measure the central RIS or across such an extensive transect of any Ice Shelf. This study confirmed the low rates of basal melting across the western RIS interior with interspersed regions of thin marine ice and debris reported by other studies, but never resolved to this level of precision. Basal melting increased in magnitude to the north, from approximately 0 to 0.5m a^{-1} over 70km. This shows the southern extent of AASW circulation and mode 3 melting around the Ross Island area. Melt rates increased up to 0.3 m a^{-1} along the SPOT to the south of the CIR. Few measurements exist across this southern region as logistics support and satellite orbitals rarely extend this far south. Basal melt rates in the order of 0.01-0.04 m a^{-1} were observed across the Siple Coast, supporting observations of lower basal melt rates in the western RIS. While our results could interpret where marine ice is likely to be present, our analysis could not quantify the rates of basal mass freezing, leaving an opportunity for future research.

Annual ApRES measurements have been proven to effectively calculate basal melt rates across ice shelves with small thickness changes and low deformation rates. Most sites with two-year measurement periods returned accurate melt rates and strain fitting. Sites with high deformations showed a poorer correlation of internal layers, suggesting that two-year measurement periods are the limit of accurate melt processing for the strain rates across the RIS. Vertical strain rates are a key component when estimating mass balance change

from total thickness changes and satellite imagery. ApRES vertical strain rates from internal layer deformation showed strong consistency with satellite-derived strain rates, further strengthening the certainty of satellite-derived basal mass balance methods. ApRES measurements did have lower spatial variation of basal melting than remote sensing observations, suggesting there is still some remaining uncertainty or seasonal variation in these measurements.

The measured basal melt rates appeared consistent or lower than most satellite estimates and ice shelf averages. This suggests no observable change in basal melt rates underneath the central RIS, and the RIS is currently remaining close to steady state. This dataset of ApRES measurements provides a precise baseline for determining future changes of cavity circulation and melting.

While this study covers a substantial section of the RIS with new measurements, it is limited to a single transect. The SPOT sites cover most of the western RIS, and most outlet flows from the EAIS. The SCT sites provide coverage near the grounding line of the eastern RIS but do not provide any data on the large central areas of the eastern RIS. Previous studies have discussed different cavity processes and increased basal freezing across the eastern RIS (Adusumilli et al., 2020; Rignot et al., 2013; Tinto et al., 2019). ApRES cannot quantify basal freezing rates, so is only able to provide ground validation and constraining widescale studies across freezing areas. Future ApRES measurements of deep field traverses and expeditions across the eastern RIS could provide a new understanding of basal mass balance into these unexplored areas.

The significant uncertainty for ongoing studies of the RIS remains the accumulation variability. Sparse measurements over small timeframes create uncertainty when determining wide-scale basal melting and mass balance trends. Continued ground measurements and atmospheric modelling will be required to understand the extent of ice shelf thickness changes, particularly in a changing climate. ApRES may also provide a solution using the reverse methodology for basal thickness change above the firn transition. By marking ApRES sites with flags or stakes at the repeat measurement site, surface accumulation rates could be determined, with firn layer movements showing information of compaction rates.

8 References

Adusumilli, S., Fricker, H. A., Medley, B., & Padman, L. (2020). Interannual variations in meltwater input to the Southern Ocean from Antarctic ice shelves. *Nature Geoscience, 13*(9), 616-620. https://doi.org/10.1038/s41561-020-0616-z

Agosta, C., Amory, C., Kittel, C., Orsi, A., Favier, V., Gallée, H., van den Broeke, M. R., Lenaerts, J. T. M., van Wessem, J. M., van de Berg, W. J., & Fettweis, X. (2019). Estimation of the Antarctic surface mass balance using the regional climate model MAR (1979–2015) and identification of dominant processes. *The Cryosphere, 13*(1), 281-296. https://doi.org/10.5194/tc-13-281-2019

Alley, K. E., Scambos, T. A., Anderson, R. S., Rajaram, H., Pope, A., & Haran, T. M. (2018). Continent-wide estimates of Antarctic strain rates from Landsat 8-derived velocity grids. *Journal of Glaciology, 64*(244), 321-332. https://doi.org/10.1017/jog.2018.23

Alley, R. B., & Bindschadler, R. A. (2001). The West Antarctic Ice Sheet and Sea-Level Change. In *The West Antarctic Ice Sheet: Behavior and Environment* (pp. 1-11). https://doi.org/https://doi.org/10.1029/AR077p0001

Arnold, M. (2016). Surface mass balance of the Ross Ice Shelf from stable water isotopes, ground penetrating radar, and back trajectory analyses.

Arzeno, I. B., Beardsley, R. C., Limeburner, R., Owens, B., Padman, L., Springer, S. R., Stewart, C. L., & Williams, M. J. M. (2014, 2014/07/01). Ocean variability contributing to basal melt rate near the ice front of Ross Ice Shelf, Antarctica. *Journal of Geophysical Research: Oceans, 119*(7), 4214-4233. https://doi.org/10.1002/2014JC009792

Assmann, K., Hellmer, H. H., & Beckmann, A. (2003). Seasonal variation in circulation and water mass distribution on the Ross Sea continental shelf. *Antarctic Science, 15*(1), 3-11. https://doi.org/10.1017/S0954102003001007

Begeman, C. B., Tulaczyk, S. M., Marsh, O. J., Mikucki, J. A., Stanton, T. P., Hodson, T. O., Siegfried, M. R., Powell, R. D., Christianson, K., & King, M. A. (2018). Ocean Stratification and Low Melt Rates at the Ross Ice Shelf Grounding Zone. *Journal of Geophysical Research: Oceans, 123*(10), 7438-7452. https://doi.org/https://doi.org/10.1029/2018JC013987

Bindschadler, R. (2006). The environment and evolution of the West Antarctic ice sheet: setting the stage. *Philosophical Transactions of the Royal Society A: Mathematical, Physical and Engineering Sciences, 364*(1844), 1583-1605.

Bindschadler, R., Choi, H., Wichlacz, A., Bingham, R., Bohlander, J., Brunt, K., Corr, H., Drews, R., Fricker, H., Hall, M., Hindmarsh, R., Kohler, J., Padman, L., Rack, W., Rotschky, G., Urbini, S., Vornberger, P., & Young, N. (2011). Getting around Antarctica: new high-resolution mappings of the grounded and freely-floating boundaries of the Antarctic ice sheet created for the International Polar Year. *The Cryosphere, 5*(3), 569-588. https://doi.org/10.5194/tc-5-569-2011

Bindschadler, R. A., Nowicki, S., Abe-Ouchi, A., Aschwanden, A., Choi, H., Fastook, J., Granzow, G., Greve, R., Gutowski, G., Herzfeld, U., Jackson, C., Johnson, J., Khroulev, C., Levermann, A., Lipscomb, W. H., Martin, M. A., Morlighem, M., Parizek, B. R., Pollard, D., Price, S. F., Ren, D., Saito, F., Sato, T., Seddik, H., Seroussi, H., Takahashi, K., Walker, R., & Wang, W. L. (2013).

Ice-sheet model sensitivities to environmental forcing and their use in projecting future sea level (the SeaRISE project). *Journal of Glaciology, 59*(214), 195-224. https://doi.org/10.3189/2013JoG12J125

Bindschadler, R. A., Roberts, E. P., & Iken, A. (1990). Age of Crary Ice Rise, Antarctica, determined from temperature-depth profiles. *Annals of Glaciology, 14*, 13-16.

Boned, C., Lagourette, B., & Clausse, M. (1979). Dielectric Behaviour of Ice Microcrystals: A Study Versus Temperature. *Journal of Glaciology, 22*(86), 145-154. https://doi.org/10.3189/S002214300001412X

Brennan, P. V., Lok, L. B., Nicholls, K., & Corr, H. (2014, Aug 2014-09-06). Phase-sensitive FMCW radar system for high-precision Antarctic ice shelf profile monitoring. *IET Radar, Sonar & Navigation, 8*(7), 776-786.

Clough, J. W., & Hansen, B. L. (1979). The Ross Ice Shelf Project. *Science, 203*(4379), 433-434. http://www.jstor.org.ezproxy.canterbury.ac.nz/stable/1747124

Crary, A. P., Robinson, E. S., Bennett, H. F., & Boyd Jr., W. W. (1962). Glaciological regime of the Ross Ice Shelf. *Journal of Geophysical Research (1896-1977), 67*(7), 2791-2807. https://doi.org/https://doi.org/10.1029/JZ067i007p02791

Craven, M., Allison, I., Fricker, H. A., & Warner, R. (2009). Properties of a marine ice layer under the Amery Ice Shelf, East Antarctica. *Journal of Glaciology, 55*(192), 717-728.

Cuffey, K. M., & Paterson, W. S. B. (2010). *The Physics of glaciers (4th ed)*. Butterworth-Heinemann/Elsevier.

Das, I., Padman, L., Bell, R. E., Fricker, H. A., Tinto, K. J., Hulbe, C. L., Siddoway, C. S., Dhakal, T., Frearson, N. P., Mosbeux, C., Cordero, S. I., & Siegfried, M. R. (2020). Multi-decadal basal melt rates and structure of the Ross Ice Shelf, Antarctica using airborne ice penetrating radar. *Journal of Geophysical Research: Earth Surface, n/a*(n/a), e2019JF005241. https://doi.org/10.1029/2019jf005241

Depoorter, M. A., Bamber, J. L., Griggs, J. A., Lenaerts, J. T. M., Ligtenberg, S. R. M., van den Broeke, M. R., & Moholdt, G. (2013, 2013/10/01). Calving fluxes and basal melt rates of Antarctic ice shelves. *Nature, 502*(7469), 89-92. https://doi.org/10.1038/nature12567

Dinniman, M. S., Asay-Davis, X. S., Galton-Fenzi, B. K., Holland, P. R., Jenkins, A., & Timmermann, R. (2016). Modeling ice shelf/ocean interaction in Antarctica: A review. *Oceanography, 29*(4), 144-153.

Dinniman, M. S., Klinck, J. M., & Smith Jr, W. O. (2011). A model study of Circumpolar Deep Water on the West Antarctic Peninsula and Ross Sea continental shelves. *Deep Sea Research Part II: Topical Studies in Oceanography, 58*(13-16), 1508-1523.

Dowdeswell, J. A., & Evans, S. (2004, 2004/08/27). Investigations of the form and flow of ice sheets and glaciers using radio-echo sounding. *Reports on Progress in Physics, 67*(10), 1821-1861. https://doi.org/10.1088/0034-4885/67/10/r03

Dupont, T. K., & Alley, R. B. (2005). Assessment of the importance of ice-shelf buttressing to ice-sheet flow. *Geophysical Research Letters, 32*(4). https://doi.org/doi:10.1029/2004GL022024

Dutrieux, P., Stewart, C., Jenkins, A., Nicholls, K. W., Corr, H. F. J., Rignot, E., & Steffen, K. (2014). Basal terraces on melting ice shelves. *Geophysical Research Letters, 41*(15), 5506-5513. https://doi.org/https://doi.org/10.1002/2014GL060618

Fretwell, P., Pritchard, H. D., Vaughan, D. G., Bamber, J. L., Barrand, N. E., Bell, R., Bianchi, C., Bingham, R., Blankenship, D. D., & Casassa, G. (2013). Bedmap2: improved ice bed, surface and thickness datasets for Antarctica. *The Cryosphere, 7*(1), 375-393.

Fujita, S., & Mae, S. (1993). Relation between ice sheet internal radio-echo reflections and ice fabric at Mizuho Station, Antarctica. *Annals of Glaciology, 17*, 269-275.

Fujita, S., Matsuoka, T., Ishida, T., Matsuoka, K., & Mae, S. (2000). A summary of the complex dielectric permittivity of ice in the megahertz range and its applications for radar sounding of polar ice sheets. Physics of ice core records,

Griggs, J. A., & Bamber, J. L. (2011). Antarctic ice-shelf thickness from satellite radar altimetry. *Journal of Glaciology, 57*(203), 485-498. https://doi.org/10.3189/002214311796905659

Grosfeld, K., Gerdes, R., & Determann, J. (1997, 1997/07/15). Thermohaline circulation and interaction between ice shelf cavities and the adjacent open ocean [https://doi.org/10.1029/97JC00891]. *Journal of Geophysical Research: Oceans, 102*(C7), 15595-15610. https://doi.org/https://doi.org/10.1029/97JC00891

Haas, C., Langhorne, P. J., Rack, W., Leonard, G. H., Brett, G. M., Price, D., Beckers, J. F., & Gough, A. J. (2021). Airborne mapping of the sub-ice platelet layer under fast ice in McMurdo Sound, Antarctica. *The Cryosphere, 15*(1), 247-264. https://doi.org/10.5194/tc-15-247-2021

Hellmer, H. H. (2004). Impact of Antarctic ice shelf basal melting on sea ice and deep ocean properties. *Geophysical Research Letters, 31*(10). https://doi.org/https://doi.org/10.1029/2004GL019506

Hellmer, H. H., & Jacobs, S. S. (1995). Seasonal circulation under the eastern Ross Ice Shelf, Antarctica. *Journal of Geophysical Research: Oceans, 100*(C6), 10873-10885. https://doi.org/https://doi.org/10.1029/95JC00753

Hodson, T., Gooch, D. L., & Stuart, G. W. (1997). Structures within the surge front at Bakaninbreen, Svalbard, using ground-penetrating radar. *Annals of Glaciology, 24*, 122-129. https://doi.org/10.3189/S0260305500012040

Holland, D. M., Jacobs, S. S., & Jenkins, A. (2003). Modelling the ocean circulation beneath the Ross Ice Shelf. *Antarctic Science, 15*(1), 13.

Hooke, R. L. (2019). *Principles of glacier mechanics*. Cambridge university press.

Horgan, H. J., Walker, R. T., Anandakrishnan, S., & Alley, R. B. (2011, 2011/02/01). Surface elevation changes at the front of the Ross Ice Shelf: Implications for basal melting [https://doi.org/10.1029/2010JC006192]. *Journal of Geophysical Research: Oceans, 116*(C2). https://doi.org/https://doi.org/10.1029/2010JC006192

Howat, I. M., Porter, C., Smith, B. E., Noh, M. J., & Morin, P. (2019). The Reference Elevation Model of Antarctica. *The Cryosphere, 13*(2), 665-674. https://doi.org/10.5194/tc-13-665-2019

Hulbe, C., & Fahnestock, M. (2007). Century-scale discharge stagnation and reactivation of the Ross ice streams, West Antarctica. *Journal of Geophysical Research: Earth Surface, 112*(F3). https://doi.org/https://doi.org/10.1029/2006JF000603

Hulbe, C. L., Scambos, T. A., Lee, C.-K., Bohlander, J., & Haran, T. (2013). Recent changes in the flow of the Ross Ice Shelf, West Antarctica. *Earth and Planetary Science Letters, 376*, 54-62.

Hulbe, C. L., Scambos, T. A., Youngberg, T., & Lamb, A. K. (2008, 2008/08/01/). Patterns of glacier response to disintegration of the Larsen B ice shelf, Antarctic Peninsula. *Global and Planetary Change, 63*(1), 1-8. https://doi.org/https://doi.org/10.1016/j.gloplacha.2008.04.001

IPCC. (2014). *Climate change 2013: the physical science basis: Working Group I contribution to the Fifth assessment report of the Intergovernmental Panel on Climate Change*. Cambridge university press.

Jacobs, S. S., Gordon, A. L., & Ardai, J. L. (1979). Circulation and Melting Beneath the Ross Ice Shelf. *Science, 203*(4379), 439-443. https://doi.org/10.1126/science.203.4379.439

Jacobs, S. S., Helmer, H. H., Doake, C. S. M., Jenkins, A., & Frolich, R. M. (1992). Melting of ice shelves and the mass balance of Antarctica. *Journal of Glaciology, 38*(130), 375-387. https://doi.org/10.3189/S0022143000002252

Jansen, D., Luckman, A., Kulessa, B., Holland, P. R., & King, E. C. (2013). Marine ice formation in a suture zone on the Larsen C Ice Shelf and its influence on ice shelf dynamics. *Journal of Geophysical Research: Earth Surface, 118*(3), 1628-1640. https://doi.org/10.1002/jgrf.20120

Jenkins, A., Corr, H. F. J., Nicholls, K. W., Stewart, C. L., & Doake, C. S. M. (2006). Interactions between ice and ocean observed with phase-sensitive radar near an Antarctic ice-shelf grounding line. *Journal of Glaciology, 52*(178), 325-346. https://doi.org/10.3189/172756506781828502

Jenkins, A., & Doake, C. S. M. (1991). Ice-ocean interaction on Ronne Ice Shelf, Antarctica. *96*(C1), 791-813. https://doi.org/doi:10.1029/90JC01952

Johari, G. P., & Charette, P. A. (1979). The Permittivity and Attenuation in Polycrystalline and Single-Crystal Ice Ih at 35 and 60 MHz. *Journal of Glaciology, 14*(71), 293-303. https://doi.org/10.3189/S002214300002178X

Jol, H. M. (2008). *Ground penetrating radar theory and applications*. elsevier.

Jordan, J. R., Holland, P. R., Jenkins, A., Piggott, M. D., & Kimura, S. (2014). Modeling ice-ocean interaction in ice-shelf crevasses. *Journal of Geophysical Research: Oceans, 119*(2), 995-1008. https://doi.org/https://doi.org/10.1002/2013JC009208

Jordan, T. M., Schroeder, D. M., Elsworth, C. W., & Siegfried, M. R. (2020). Estimation of ice fabric within Whillans Ice Stream using polarimetric phase-sensitive radar sounding. *Annals of Glaciology, 61*(81), 74-83.

Joughin, I., & Padman, L. (2003). Melting and freezing beneath Filchner-Ronne Ice Shelf, Antarctica. *Geophysical Research Letters, 30*(9). https://doi.org/10.1029/2003gl016941

Joughin, I., & Vaughan, D. G. (2004). Marine ice beneath the Filchner–Ronne Ice Shelf, Antarctica: a comparison of estimated thickness distributions. *Annals of Glaciology, 39*, 511-517.

Kovacs, A., Gow, A. J., & Morey, R. M. (1995, 1995/05/01/). The in-situ dielectric constant of polar firn revisited. *Cold Regions Science and Technology, 23*(3), 245-256. https://doi.org/https://doi.org/10.1016/0165-232X(94)00016-Q

Kruetzmann, N. C., Rack, W., McDonald, A. J., & George, S. E. (2011). Snow accumulation and compaction derived from GPR data near Ross Island, Antarctica. *Cryosphere, 5*(2), 391-404. https://doi.org/10.5194/tc-5-391-2011

Kulessa, B., Booth, A. D., O'Leary, M., McGrath, D., King, E. C., Luckman, A. J., Holland, P. R., Jansen, D., Bevan, S. L., & Thompson, S. S. (2019). Seawater softening of suture zones inhibits fracture propagation in Antarctic ice shelves. *Nature Communications, 10*(1), 1-12.

Langhorne, P., Hughes, K., Gough, A., Smith, I., Williams, M., Robinson, N., Stevens, C., Rack, W., Price, D., & Leonard, G. (2015). Observed platelet ice distributions in Antarctic sea ice: An index for ocean ‐ ice shelf heat flux. *Geophysical Research Letters, 42*(13), 5442-5451.

Le Brocq, A. M., Payne, A. J., & Vieli, A. (2010). An improved Antarctic dataset for high resolution numerical ice sheet models (ALBMAP v1). *Earth Syst. Sci. Data, 2*(2), 247-260. https://doi.org/10.5194/essd-2-247-2010

Legrand, M., & Mayewski, P. (1997). Glaciochemistry of polar ice cores: A review. *Reviews of Geophysics, 35*(3), 219-243. https://doi.org/https://doi.org/10.1029/96RG03527

Li, J., & Zwally, H. J. (2004). Modeling the density variation in the shallow firn layer. *Annals of Glaciology, 38*, 309-313. https://doi.org/10.3189/172756404781814988

Liu, Y., Moore, J. C., Cheng, X., Gladstone, R. M., Bassis, J. N., Liu, H., Wen, J., & Hui, F. (2015). Ocean-driven thinning enhances iceberg calving and retreat of Antarctic ice shelves. *Proceedings of the National Academy of Sciences of the United States of America, 112*(11), 3263-3268. https://doi.org/10.1073/pnas.1415137112

MacAyeal, D. R. (1984, 1984/01/20). Thermohaline circulation below the Ross Ice Shelf: A consequence of tidally induced vertical mixing and basal melting. *Journal of Geophysical Research: Oceans, 89*(C1), 597-606. https://doi.org/10.1029/JC089iC01p00597

Marsh, O. J., Fricker, H. A., Siegfried, M. R., Christianson, K., Nicholls, K. W., Corr, H. F. J., & Catania, G. (2016). High basal melting forming a channel at the grounding line of Ross Ice Shelf, Antarctica. *Geophysical Research Letters, 43*(1), 250-255. https://doi.org/10.1002/2015GL066612

Matsuoka, K., Hindmarsh, R. C. A., Moholdt, G., Bentley, M. J., Pritchard, H. D., Brown, J., Conway, H., Drews, R., Durand, G., Goldberg, D., Hattermann, T., Kingslake, J., Lenaerts, J. T. M., Martín, C., Mulvaney, R., Nicholls, K. W., Pattyn, F., Ross, N., Scambos, T., & Whitehouse, P. L. (2015, 2015/11/01/). Antarctic ice rises and rumples: Their properties and significance for ice-sheet dynamics and evolution. *Earth-Science Reviews, 150*, 724-745. https://doi.org/https://doi.org/10.1016/j.earscirev.2015.09.004

Mercer, J. H. (1978). West Antarctic ice sheet and CO 2 greenhouse effect: A threat of disaster. *Nature, 271*(5643), 321-325.

Moholdt, G., & Matsuoka, K. (2015). Inventory of Antarctic ice rises and rumples (Version 1). *Tromsø, Norway: Norwegian Polar Institute*.

Moholdt, G., Padman, L., & Fricker, H. A. (2014). Basal mass budget of Ross and Filchner-Ronne ice shelves, Antarctica, derived from Lagrangian analysis of ICESat altimetry. *Journal of Geophysical Research: Earth Surface, 119*(11), 2361-2380. https://doi.org/10.1002/2014jf003171

Mouginot, J., Rignot, E., & Scheuchl, B. (2019, 2019/08/28). Continent-Wide, Interferometric SAR Phase, Mapping of Antarctic Ice Velocity [https://doi.org/10.1029/2019GL083826]. *Geophysical Research Letters, 46*(16), 9710-9718. https://doi.org/https://doi.org/10.1029/2019GL083826

Mouginot, J., Rignot, E., Scheuchl, B., & Millan, R. (2017). Comprehensive annual ice sheet velocity mapping using Landsat-8, Sentinel-1, and RADARSAT-2 data. *Remote Sensing, 9*(4), 364.

Mouginot, J., Scheuchl, B., & Rignot, E. (2012). Mapping of ice motion in Antarctica using synthetic-aperture radar data. *Remote Sensing, 4*(9), 2753-2767.

Naish, T., Powell, R., Levy, R., Wilson, G., Scherer, R., Talarico, F., Krissek, L., Niessen, F., Pompilio, M., & Wilson, T. (2009). Obliquity-paced Pliocene West Antarctic ice sheet oscillations. *Nature, 458*(7236), 322-328.

Neal, C. S. (1979). The Dynamics of the Ross Ice Shelf Revealed by Radio Echo-Sounding. *Journal of Glaciology, 24*(90), 295-307. https://doi.org/10.3189/S0022143000014817

Neckel, N., Drews, R., Rack, W., & Steinhage, D. (2012). Basal melting at the Ekström Ice Shelf, Antarctica, estimated from mass flux divergence. *Annals of Glaciology, 53*(60), 294-302. https://doi.org/10.3189/2012AoG60A167

Oerter, H., Kipfstuhl, J., Determann, J., Miller, H., Wagenbach, D., Minikin, A., & Graft, W. (1992, 1992/07/01). Evidence for basal marine ice in the Filchner–Ronne ice shelf. *Nature, 358*(6385), 399-401. https://doi.org/10.1038/358399a0

Padman, L., Siegfried, M. R., & Fricker, H. A. (2018). Ocean tide influences on the Antarctic and Greenland ice sheets. *Reviews of Geophysics, 56*(1), 142-184.

Paolo, F. S., Fricker, H. A., & Padman, L. (2015). Volume loss from Antarctic ice shelves is accelerating. *Science, 348*(6232), 327-331. https://science.sciencemag.org/content/sci/348/6232/327.full.pdf

Petty, A. A., Feltham, D. L., & Holland, P. R. (2013). Impact of atmospheric forcing on Antarctic continental shelf water masses. *Journal of Physical Oceanography, 43*(5), 920-940.

Plewes, L. A., & Hubbard, B. (2001, 2001/06/01). A review of the use of radio-echo sounding in glaciology. *Progress in Physical Geography: Earth and Environment, 25*(2), 203-236. https://doi.org/10.1177/030913330102500203

Price, S., Bindschadler, R., Hulbe, C. L., & Joughin, I. R. (2001, 03/01). Post-stagnation behavior in the upstream regions of Ice Stream C, West Antarctica. *Journal of Glaciology, 47*, 283-294. https://doi.org/10.3189/172756501781832232

Rack, W., & Rott, H. (2004). Pattern of retreat and disintegration of the Larsen B ice shelf, Antarctic Peninsula. *Annals of Glaciology, 39*, 505-510. https://doi.org/10.3189/172756404781814005

Ragle, R. H., Blair, R. G., & Persson, L. E. (1964). Ice Core Studies of Ward Hunt Ice Shelf, 1960. *Journal of Glaciology, 5*(37), 39-59. https://doi.org/10.3189/S0022143000028562

Reese, R., Gudmundsson, G. H., Levermann, A., & Winkelmann, R. (2018, 2018/01/01). The far reach of ice-shelf thinning in Antarctica. *Nature Climate Change, 8*(1), 53-57. https://doi.org/10.1038/s41558-017-0020-x

Retzlaff, R., & Bentley, C. R. (1993). Timing of stagnation of Ice Stream C, West Antarctica, from short-pulse radar studies of buried surface crevasses. *Journal of Glaciology, 39*(133), 553-561. https://doi.org/10.3189/S0022143000016440

Rignot, E., Casassa, G., Gogineni, P., Krabill, W., Rivera, A., & Thomas, R. (2004). Accelerated ice discharge from the Antarctic Peninsula following the collapse of Larsen B ice shelf. *Geophysical Research Letters, 31*(18). https://doi.org/10.1029/2004gl020697

Rignot, E., Jacobs, S., Mouginot, J., & Scheuchl, B. (2013). Ice-Shelf Melting Around Antarctica. *Science, 341*(6143), 266-270. https://doi.org/10.1126/science.1235798

Rignot, E., Mouginot, J., & Scheuchl, B. (2011). Ice flow of the Antarctic ice sheet. *Science, 333*(6048), 1427-1430. https://science.sciencemag.org/content/333/6048/1427.long

Rignot, E., Mouginot, J., & Scheuchl, B. (2017). MEaSUREs InSAR-based Antarctica ice velocity map, Version 2. *Boulder, Colorado USA. NASA National Snow and Ice Data Center Distributed Active Archive Center. doi, 10*, D7GK8F5J8M8R.

Rignot, E., Mouginot, J., Scheuchl, B., van den Broeke, M., van Wessem, M. J., & Morlighem, M. (2019). Four decades of Antarctic Ice Sheet mass balance from 1979–2017. *Proceedings of the National Academy of Sciences, 116*(4), 1095-1103. https://doi.org/10.1073/pnas.1812883116

Robin, G. D. Q., Evans, S., Bailey, J. T., & Bullard, E. C. (1969). Interpretation of radio echo sounding in polar ice sheets. *Philosophical Transactions of the Royal Society of London. Series A, Mathematical and Physical Sciences, 265*(1166), 437-505. https://doi.org/doi:10.1098/rsta.1969.0063

Rott, H., Rack, W., Skvarca, P., & Angelis, H. D. (2002). Northern Larsen Ice Shelf, Antarctica: further retreat after collapse. *Annals of Glaciology, 34*, 277-282. https://doi.org/10.3189/172756402781817716

Ryan, M. R. (2016). *Characteristics of the Ross and Southern McMurdo ice shelves as revealed from ground-based radar surveys: a thesis submitted in partial fulfilment of the requirements for the degree of Master of Science in Environmental Science, Gateway Antarctica, University of Canterbury*
http://canterbury.summon.serialssolutions.com/2.0.0/link/0/eLvHCXMwfV1Lb8IwDLaGdpngwLRNwMbk_YBOJaWkPezEQ7twQRy4obROxQGK1AK_H7vqoKsE50TO23bsfF8APPXtOjWdEHiG94Y3CiJt2KSGyuo4Cq3rR747IlUDvcLfp50FMqbexH1ewd2PkviY1g1JoArv42p1eUIoQirmY9aG5qSS9n6GB5u-wGb8nysZ9wmyN4YLNlvI93ssfrezWYrzeC5E3shnGvON3Z4sV8hRyJdYvRMKRAQFnpGSI1aJMDNkMsyP2YkX6hW-ZtPl-Ne59m5dRm3W5SjUG7SMtJYeCkwcdQDJ-gENwqF2-XoWxp4h9imSWDyJSOtk0IXebYG9e4Xv8MQOQRli-IDHhI-A7Vdn77OY0DO6G5F8

Schmeltz, M., Rignot, E., & MacAyeal, D. R. (2001). Ephemeral grounding as a signal of ice-shelf change. *Journal of Glaciology, 47*(156), 71-77.

Schroeder, D. M., Bingham, R. G., Blankenship, D. D., Christianson, K., Eisen, O., Flowers, G. E., Karlsson, N. B., Koutnik, M. R., Paden, J. D., & Siegert, M. J. (2020). Five decades of radioglaciology. *Annals of Glaciology, 61*(81), 1-13. https://doi.org/10.1017/aog.2020.11

Smith, B. M. E., & Evans, S. (1972). Radio Echo Sounding: Absorption and Scattering by Water Inclusion and Ice Lenses. *Journal of Glaciology, 11*(61), 133-146. https://doi.org/10.3189/S0022143000022541

Stevens, C., Hulbe, C., Brewer, M., Stewart, C., Robinson, N., Ohneiser, C., & Jendersie, S. (2020). Ocean mixing and heat transport processes observed under the Ross Ice Shelf control its basal melting. *Proceedings of the National Academy of Sciences, 117*(29), 16799-16804. https://doi.org/10.1073/pnas.1910760117

Stewart, C. L., Christoffersen, P., Nicholls, K. W., Williams, M. J. M., & Dowdeswell, J. A. (2019, 2019/06/01). Basal melting of Ross Ice Shelf from solar heat absorption in an ice-front polynya. *Nature Geoscience, 12*(6), 435-440. https://doi.org/10.1038/s41561-019-0356-0

Timmermann, R., Brocq, A. L., Deen, T., Domack, E., Dutrieux, P., Galton-Fenzi, B., Hellmer, H., Humbert, A., Jansen, D., & Jenkins, A. (2010). A consistent data set of Antarctic ice sheet topography, cavity geometry, and global bathymetry. *Earth System Science Data, 2*(2), 261-273.

Timmermann, R., Wang, Q., & Hellmer, H. H. (2017). Ice-shelf basal melting in a global finite-element sea-ice/ice-shelf/ocean model. *Annals of Glaciology, 53*(60), 303-314. https://doi.org/10.3189/2012AoG60A156

Tinto, K. J., Padman, L., Siddoway, C. S., Springer, S. R., Fricker, H. A., Das, I., Caratori Tontini, F., Porter, D. F., Frearson, N. P., Howard, S. L., Siegfried, M. R., Mosbeux, C., Becker, M. K., Bertinato, C., Boghosian, A., Brady, N., Burton, B. L., Chu, W., Cordero, S. I., Dhakal, T., Dong, L., Gustafson, C. D., Keeshin, S., Locke, C., Lockett, A., O'Brien, G., Spergel, J. J., Starke, S. E., Tankersley, M., Wearing, M. G., & Bell, R. E. (2019, 2019/06/01). Ross Ice Shelf response to climate driven by the tectonic imprint on seafloor bathymetry. *Nature Geoscience, 12*(6), 441-449. https://doi.org/10.1038/s41561-019-0370-2

van den Broeke, M. (2008, 2008/05/01). Depth and Density of the Antarctic Firn Layer. *Arctic, Antarctic, and Alpine Research, 40*(2), 432-438. https://doi.org/10.1657/1523-0430(07-021)[BROEKE]2.0.CO;2

Vaughan, D. G. (1995). Tidal flexure at ice shelf margins. *Journal of Geophysical Research: Solid Earth, 100*(B4), 6213-6224. https://doi.org/https://doi.org/10.1029/94JB02467

Waite, A. H., & Schmidt, S. J. (1962). Gross Errors in Height Indication from Pulsed Radar Altimeters Operating over Thick Ice or Snow. *Proceedings of the IRE, 50*(6), 1515-1520. https://doi.org/10.1109/JRPROC.1962.288195

Zotikov, I. A., Zagorodnov, V. S., & Raikovsky, J. V. (1980). Core drilling through the Ross Ice Shelf (Antarctica) confirmed basal freezing. *Science, 207*(4438), 1463-1465. https://science.sciencemag.org/content/207/4438/1463.long

Appendix A. ApRES Dataset Additional Information

Appendix A.2: *Timeline and number of measurements taken during each season*

Year	Researcher(s)	Logistics	Sites measured
2015	Michelle Ryan Wolfgang Rack	HWD-2 Traverse	T1-12, 1-9 HWD
2016	Michelle Ryan	HWD-2 Traverse	T1-12
2017	Adrian MacDonald Kelly Gragg Martin Forbes	Helicopter	T1-7
2018	Daniel Price	HWD-1 Traverse	T1-21, P1-11
2019	Daniel Price	HWD-1 Traverse	T1-21, P1-11, System test
2020	James	HWD-1 Traverse	T1-21, P1-11

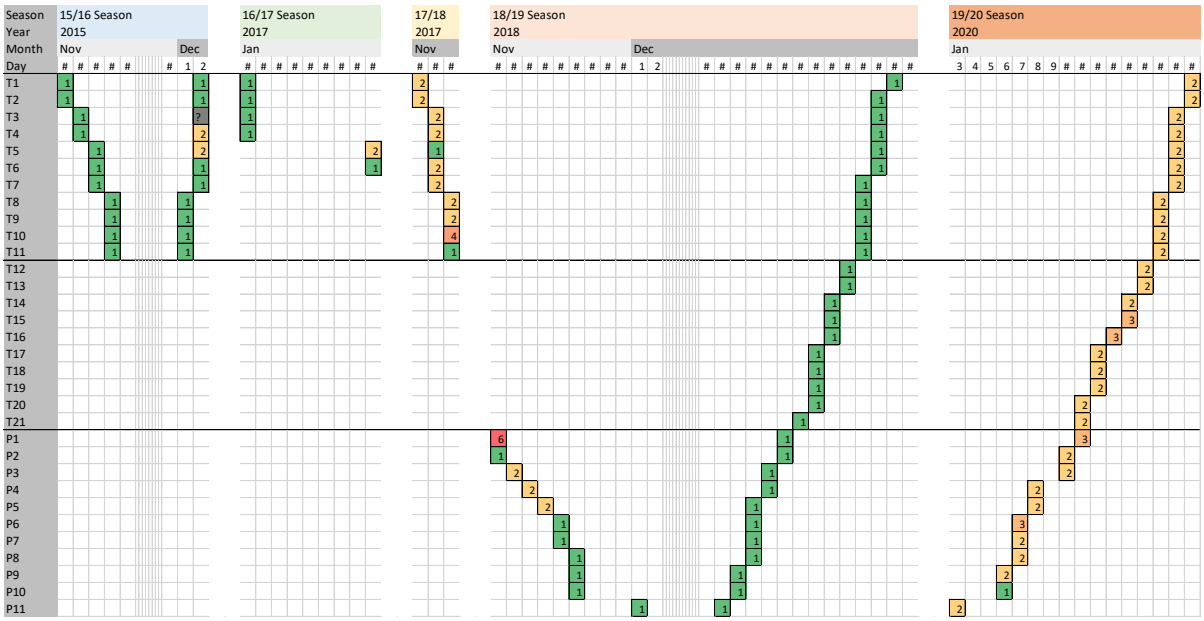

Appendix A.1: *Timeline and number of measurements taken during each season.*

Appendix B. Site Measurement Settings and Amplitude Profiles

Year denotes the Antarctic Season the measurement was taken during.

T1

Antarctic Season	**Latitude**	**Longitude**	**Attenuation** (AVG)	**Gain** (dB)	**Basal reflection uncorrected** (m)	**Reflection strength**	**Basal reflection power** (dB increase)
2015.1	-78.5867	169.8297	31	-6	339.3	Strong	46
2015.2			31	-6	339.3	Strong	48
2016	-78.5810	169.8341	15	0	338.9	Strong	57
2017.1	-78.5761	169.8419	31	-6	338	Strong	56
2017.2			31	-6	338	Strong	56
2018	-78.5704	169.8487	31	-6	337.4	Strong	43
2019.1	-78.5650	169.8586	31	-4	336.5	Strong	43
2019.2			20	6	336.5	Strong	51

2015

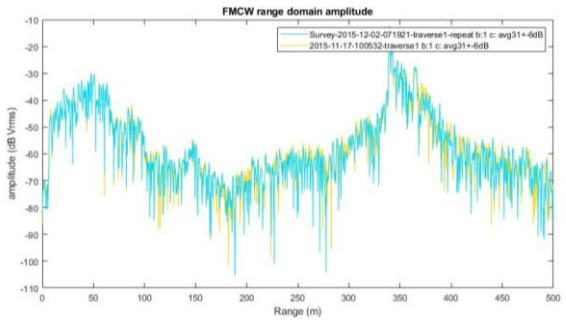

2016

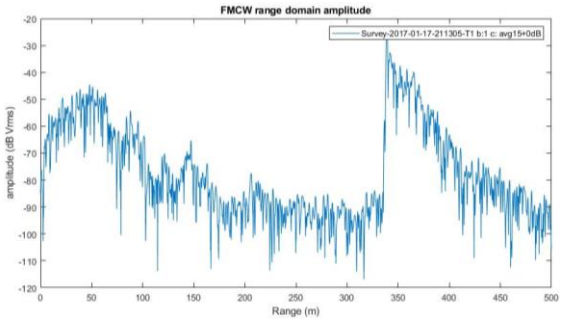

2017

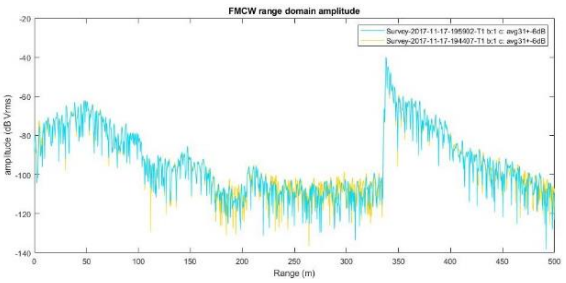

2018

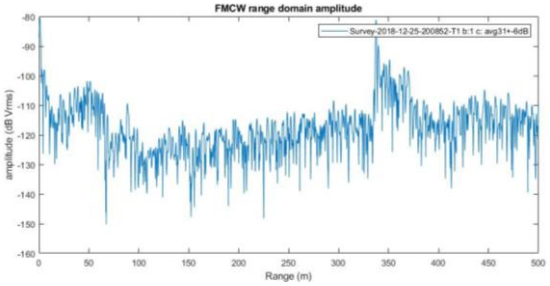

2019

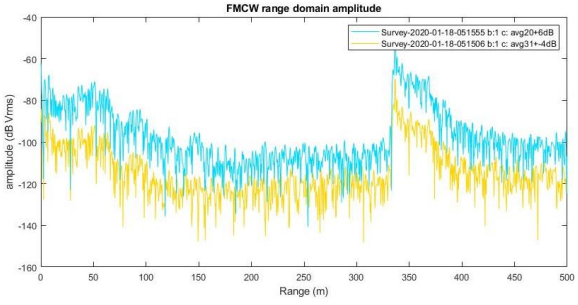

T2

Antarctic Season	Latitude	Longitude	Attenuation (AVG)	Gain (dB)	Basal reflection uncorrected (m)	Reflection strength	Basal reflection power (dB increase)
2015.1	-78.7539	170.1632	31	-6	370.8	Strong	46
2015.2			31	-6	370.6	Strong	46
2016	-78.7480	170.1725	31	-6	370.4	Strong	52
2017.1	-78.7431	170.1800	31	-6	369.8	Strong	47
2017.2			31	-6	369.8	Strong	44
2018	-78.7372	170.1890	31	-6	369.3	Moderate	45
2019.1	-78.7313	170.1966	31	-4	368.9	Strong	41
2019.2			20	6	368.9	Strong	42

2015

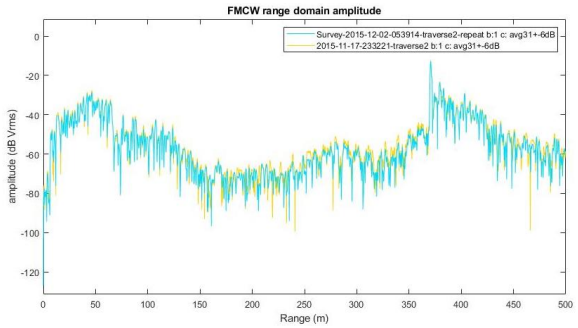

2016

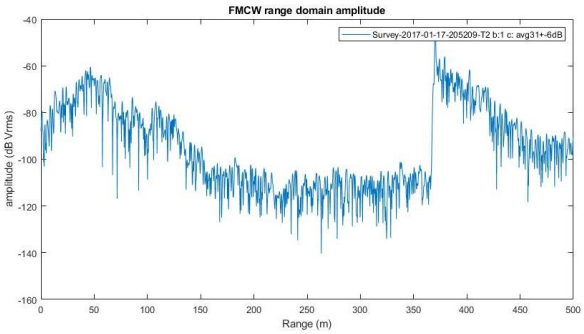

2017

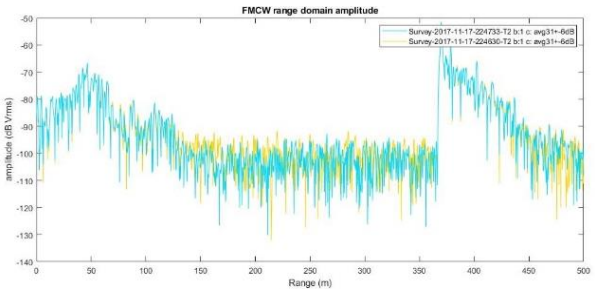

2018

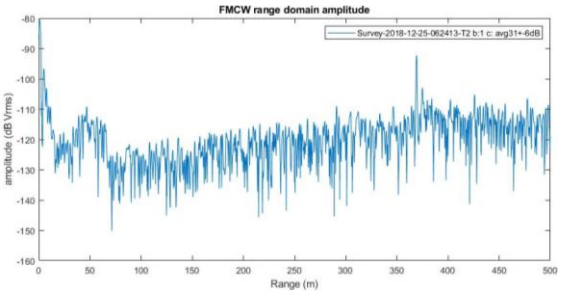

2019

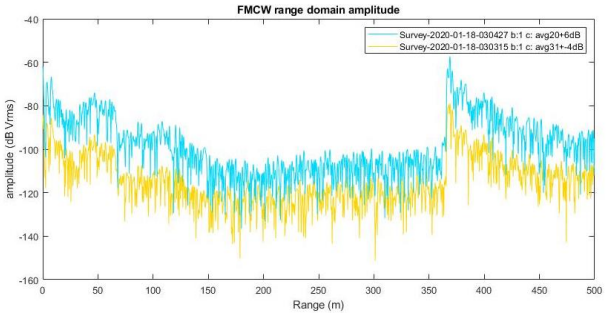

T3

Year	Latitude	Longitude	Attenuation (AVG)	Gain (dB)	Basal reflection uncorrected (m)	Reflection strength	Basal reflection power (dB increase)
2015	-78.9671	170.6004	31	-6	377.6	Strong	47
2016	-78.9609	170.6105	31	-6	377.4	Strong	42
2017.1	-78.9561	170.6231	31	-6	377.2	Strong	44
2017.2			31	-6	377.2	Strong	43
2018	-78.9499	170.6353	31	-6	376.8	Weak	21
2019.1	-78.9440	170.6456	31	-4	374.9	Strong	37
2019.2			20	6	374.4	Strong	34

2015

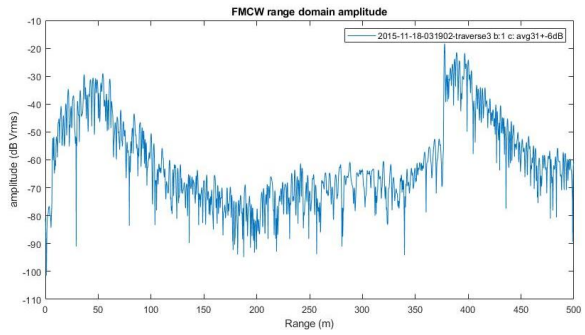

2016

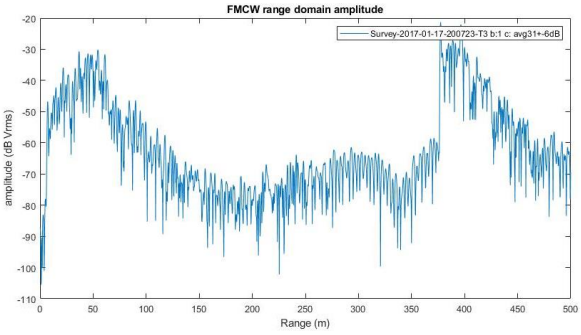

2017

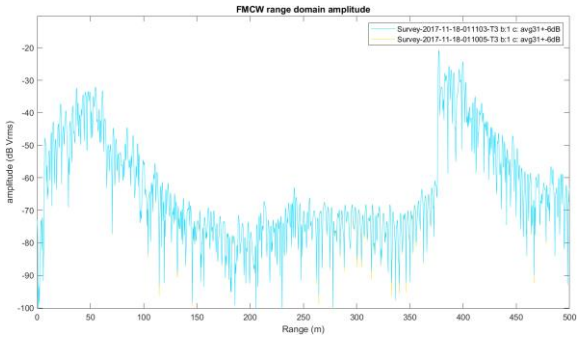

2018

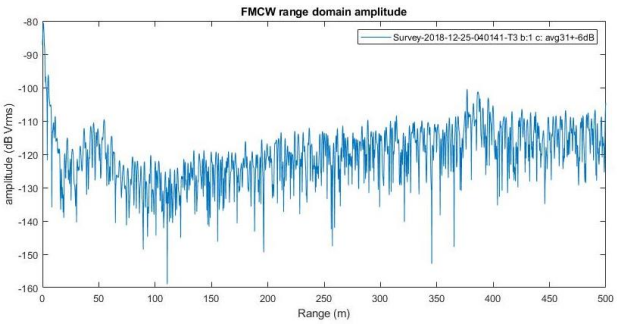

2019

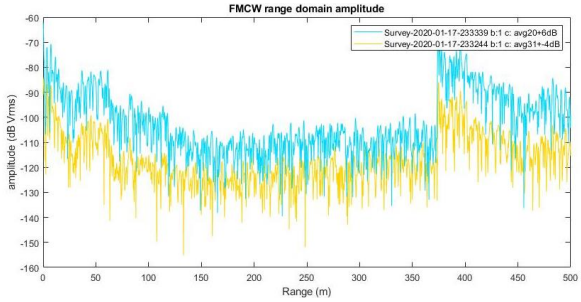

T4

Year	Latitude	Longitude	Attenuation (AVG)	Gain (dB)	Basal reflection uncorrected (m)	Reflection strength	Basal reflection power (dB increase)
2015.1	-79.1733	171.0369	31	-6	417	Moderate	30
2015.2			31	-6	417	Moderate	31
2015.3			31	-6	418.5	Moderate	29
2016	-79.1673	171.0504	31	-6	418.3	Moderate	30
2017.1	-79.1616	171.0656	31	-6	418.7	Moderate	30
2017.2			31	-6	418.7	Moderate	31
2018	-79.1554	171.0808	31	-6	418.5	Moderate	22
2019.1	-79.1494	171.0950	31	-4	418.3	Weak	12
2019.2			20	6	418.3	Weak	18

2015

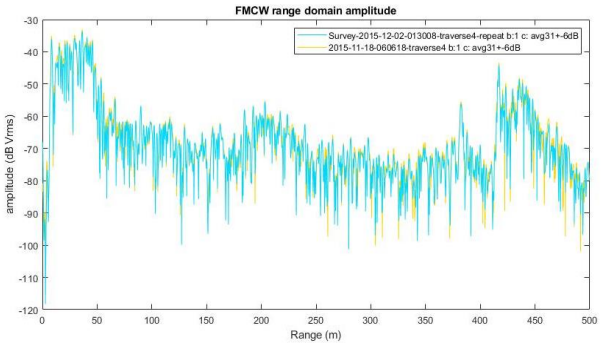

2016

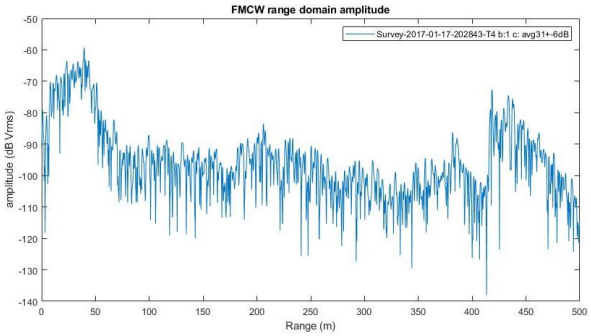

2017

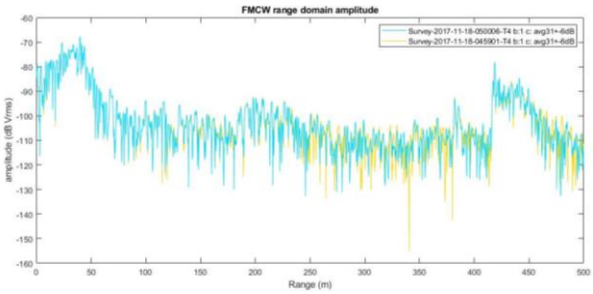

2018

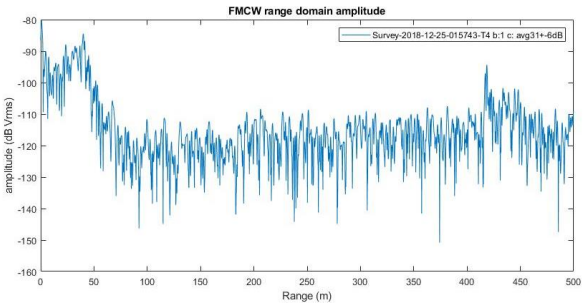

2019

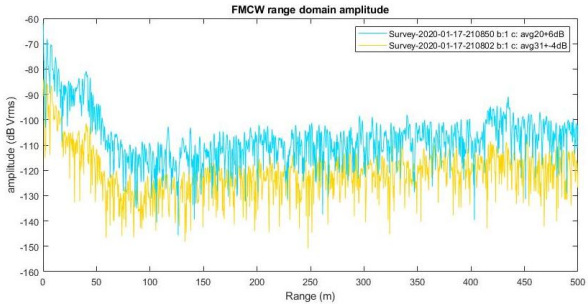

T5

Year	Latitude	Longitude	Attenuation (AVG)	Gain (dB)	Basal reflection uncorrected (m)	Reflection strength	Basal reflection power (dB increase)
2015.1	-79.3847	171.4796	30	0	380.8	Weak	26
2015.2			31	-6	383.2	Weak	25
2015.3			30	0	383	Weak	24
2016.1	-79.3786	171.4941	31	-6	381.5	Weak	23
2016.2			30	0	381.5	Weak	21
2017	-79.3735	171.5111	31	-6	381.3	Weak	23
2018	-79.3667	171.5279	31	0	383	Very Weak	9
2019.1	-79.3612	171.5416	31	-4	381.7	Weak	17
2019.2			30	-4	383.2	Weak	12

2015

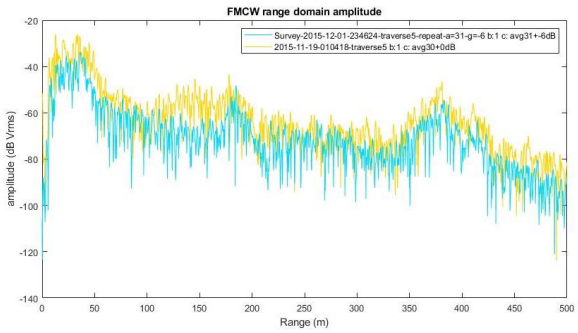

2016

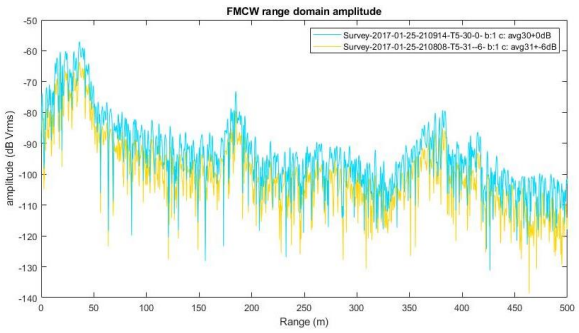

2017

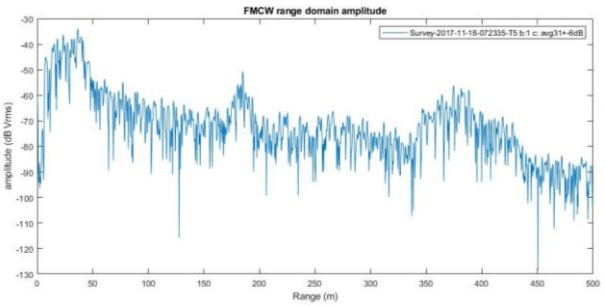

2018

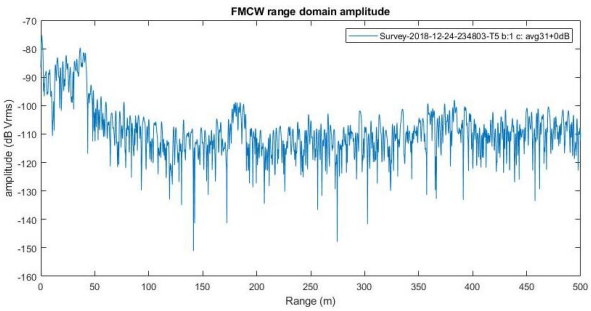

2019

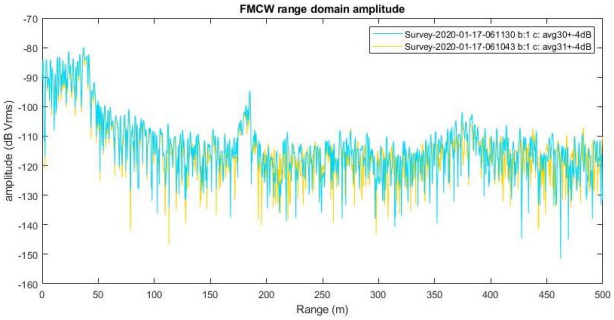

T6

Year	Latitude	Longitude	Attenuation (AVG)	Gain (dB)	Basal reflection uncorrected (m)	Reflection strength	Basal reflection power (dB increase)
2015.1	-79.4364	171.5800	31	-6	406	Weak	29
2015.2			31	-6	409.6	Weak	25
2016	-79.4302	171.5967	31	-6	410.6	Weak	26
2017.1	-79.4252	171.6114	31	-6		Weak	
2017.2			31	-6	400.4	Weak	24
2018	-79.4189	171.6303	31	0	413.2	Very Weak	15
2019	-79.4129	171.6460	31	-4	396.6	Weak	18

2015

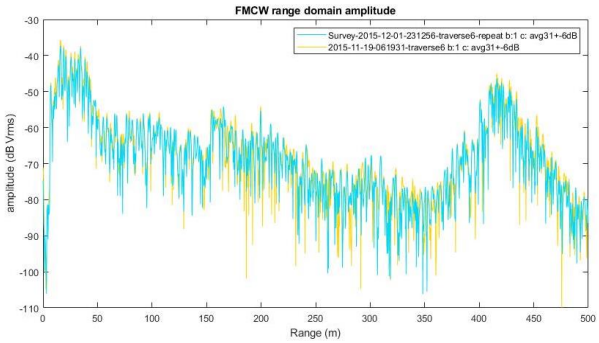

2016

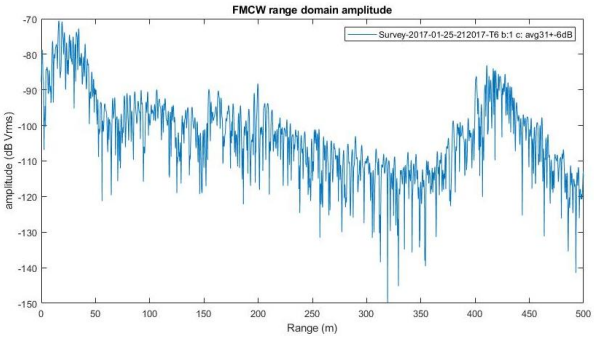

2017

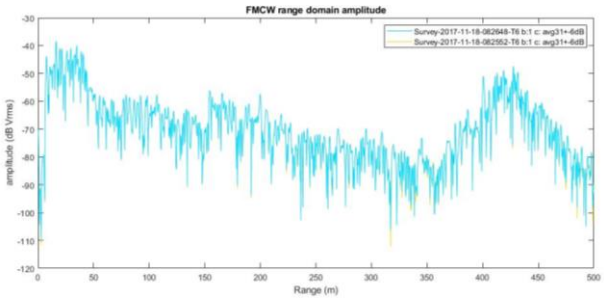

2018

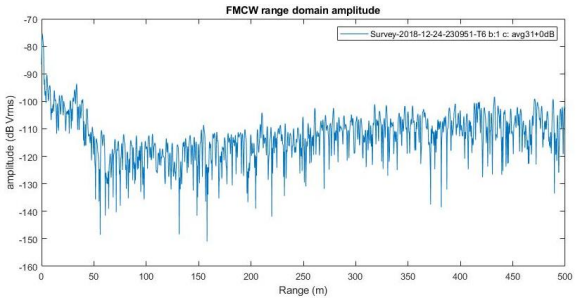

2019

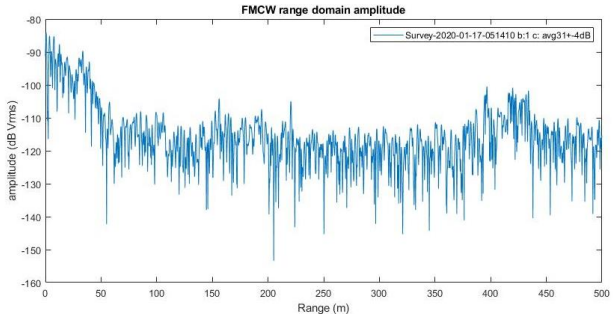

T7

Year	Latitude	Longitude	Attenuation (AVG)	Gain (dB)	Basal reflection uncorrected (m)	Reflection strength	Basal reflection power (dB increase)
2015.1	-79.6513	172.0281	31	-6	392.5	Strong	57
2015.2			31	-6	392.5	Strong	57
2017.2	-79.6404	172.0596	31	-6	392.8	Strong	54
2018	-79.6345	172.0764	31	0	392.3	Strong	38
2019	-79.6286	172.0922	31	-4	392.3	Strong	54
2017.1			31	0	392.8	Strong	54

2015

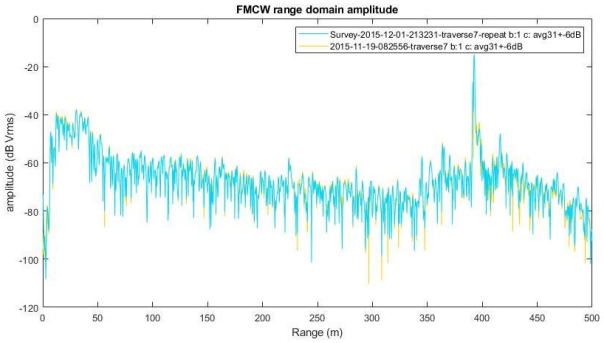

2016 – No measurement

2017

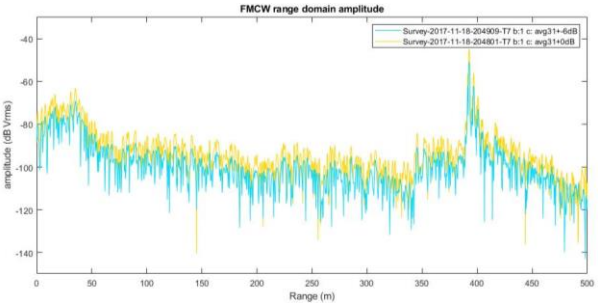

2018

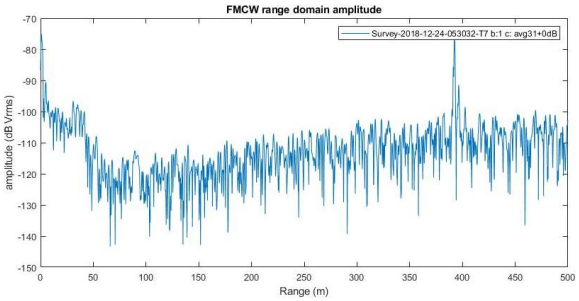

2019

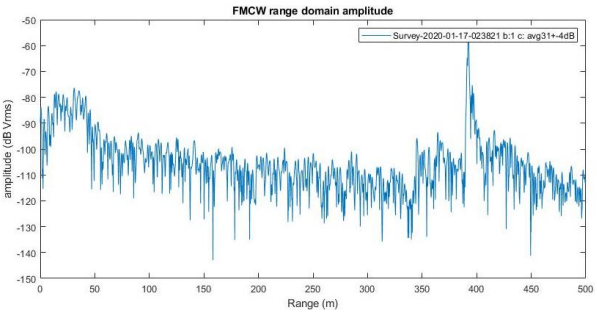

T8

Year	Latitude	Longitude	Attenuation (AVG)	Gain (dB)	Basal reflection uncorrected (m)	Reflection strength	Basal reflection power (dB increase)
2015.1	-79.9660	172.7056	28	0	358.7	Strong	48
2015.2			28	0	358.7	Strong	38
2017.1	-79.9556	172.7342	28	0	358.5	Moderate	28
2017.2			28	0	358.5	Moderate	26
2018	-79.9501	172.7494	28	0	358.5	Very Weak	17
2019	-79.9446	172.7640	28	-4	358.3	Strong	30

2015

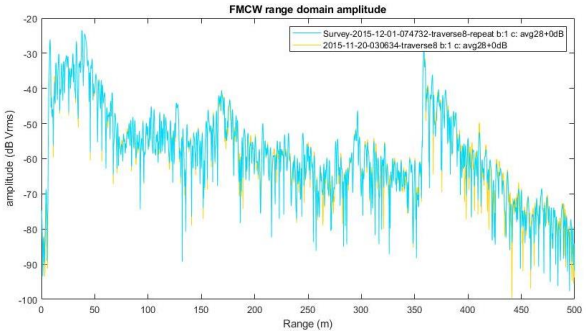

2016 – No measurement

2017

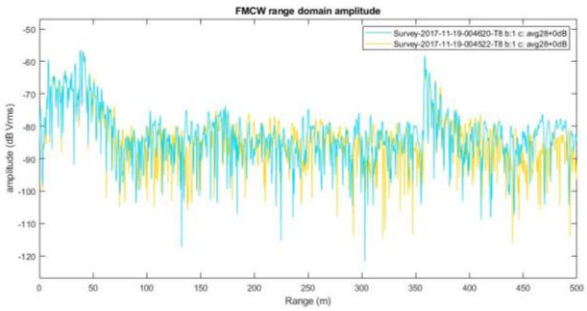

2018

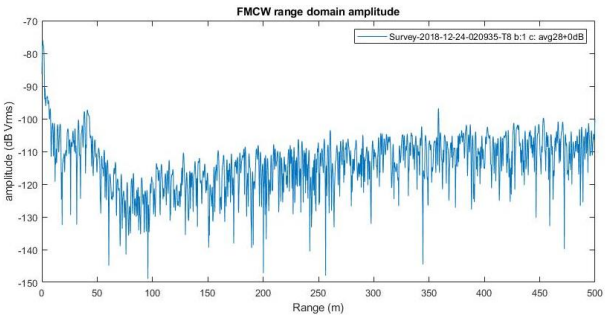

2019

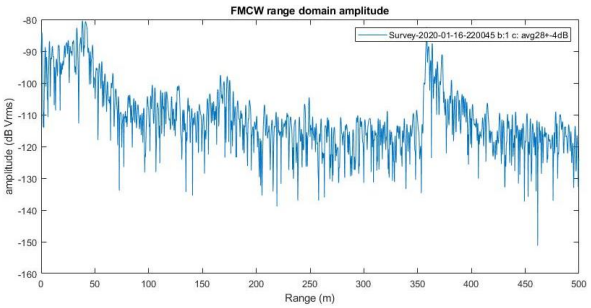

T9

Year	Latitude	Longitude	Attenuation (AVG)	Gain (dB)	Basal reflection uncorrected (m)	Reflection strength	Basal reflection power (dB increase)
2015.1	-80.0726	172.9431	28	0	351.4	Strong	40
2015.2			28	0	351.4	Strong	41
2017.1	-80.0624	172.9701	28	0	351.2	Moderate	37
2017.2			28	0	351.2	Moderate	36
2018	-80.0569	172.9848	28	0	348.5	Very Weak	12
2019	-80.0517	172.9985	28	-4	348.9	Moderate	20

2015

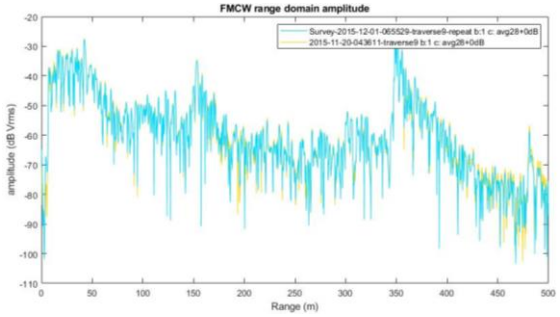

2016 – No measurement

2017

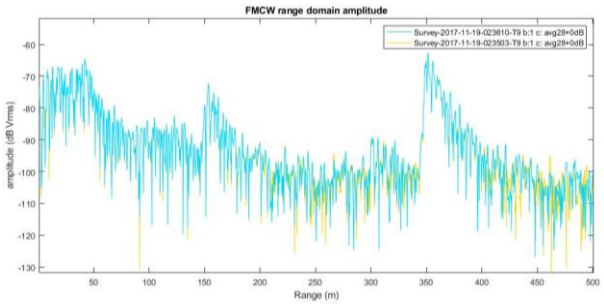

2018

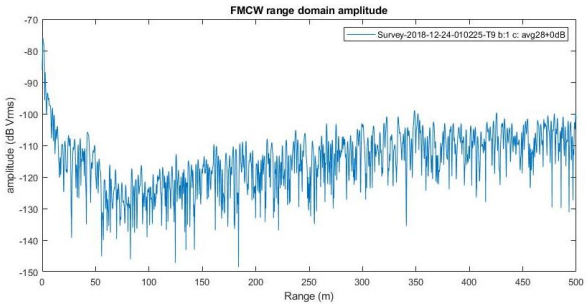

2019

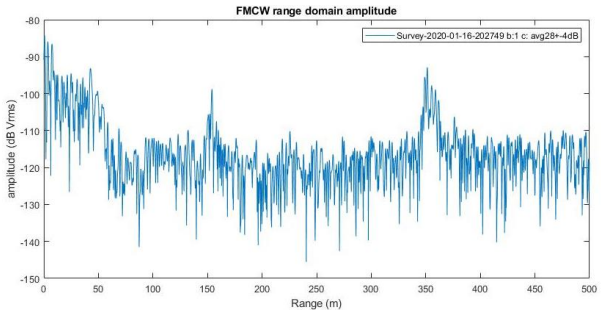

T10

Year	Latitude	Longitude	Attenuation (AVG)	Gain (dB)	Basal reflection uncorrected (m)	Reflection strength	Basal reflection power (dB increase)
2015.1	-80.1754	173.1777	28	0	329.5	Moderate	29
2015.2			28	0	329.5	Moderate	29
2017	-80.1654	173.2033	28	0	329.3	Weak	15
2017.1			28	0	328.4	Weak	13
2017.2			28	6	328.3	Weak	11
2017.3			28	6	329.3	Weak	12
2018	-80.1599	173.2172	28	0	331.2	Very Weak	7
2019	-80.1545	173.2292	28	-4	329.5	Very Weak	10

2015

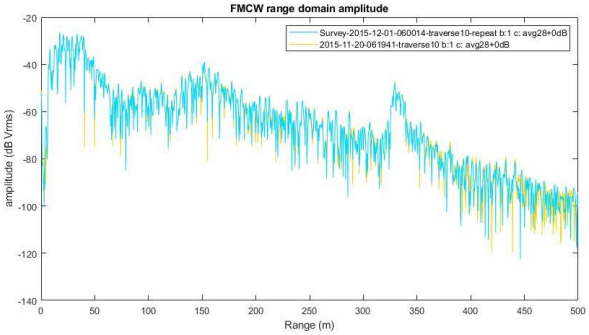

2016 – No measurement

2017

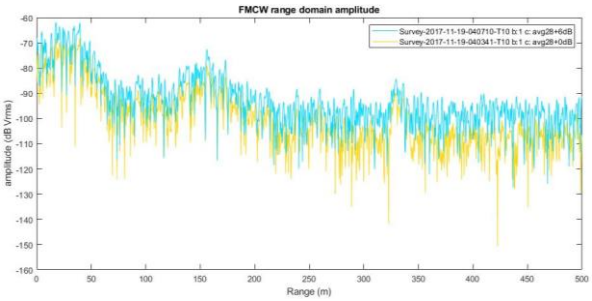

2018

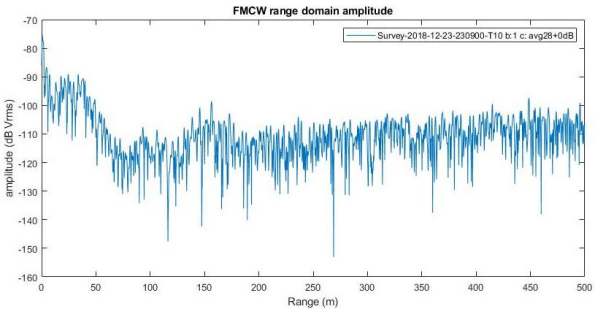

2019

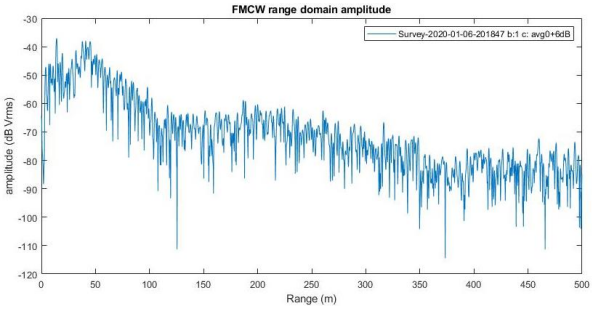

T11

Year	Latitude	Longitude	Attenuation (AVG)	Gain (dB)	Basal reflection uncorrected (m)	Reflection strength	Basal reflection power (dB increase)
2015.1	-80.3835	173.6721	28	0	338	Moderate	26
2015.2			28	0	338	Moderate	25
2017	-80.3736	173.6948	28	0	339.9	Weak	19
2018	-80.3682	173.7072	28	0	337.6	Weak	11
2019.1	-80.3628	173.7183	28	-4	337	Weak	8

2015

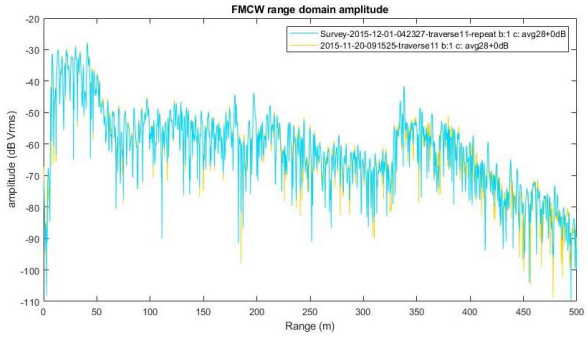

2016 – No measurement

2017

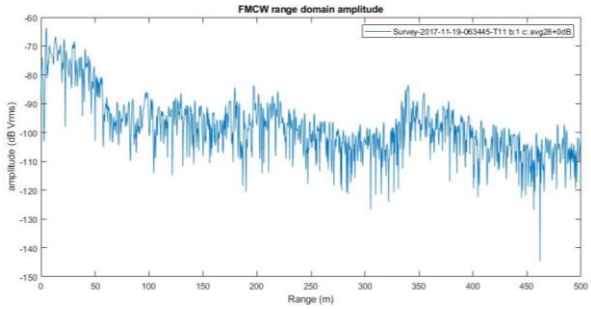

2018

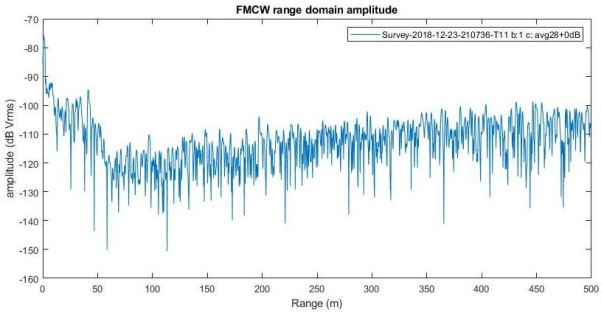

2019

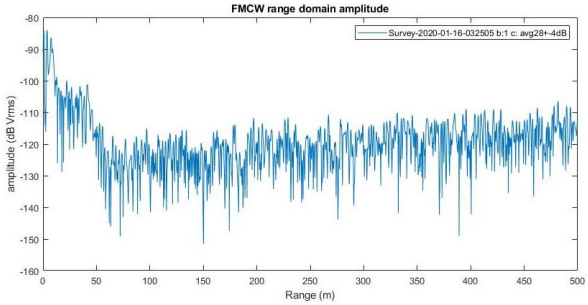

T12

Year	Latitude	Longitude	Attenuation (AVG)	Gain (dB)	Basal reflection uncorrected (m)	Reflection strength	Basal reflection power (dB increase)
2015.1	-80.6746	174.4044	28	0	333.8		27
2015.2			28	0	333.8		23
2016	-80.6696	174.4136	28	0	333.3		24
2018	-80.6601	174.4334	28	0	333.5	Weak	19
2019.1	-80.6552	174.4444	ERROR			Weak	
2019.2			28	-4	335	Very Weak	11

2015

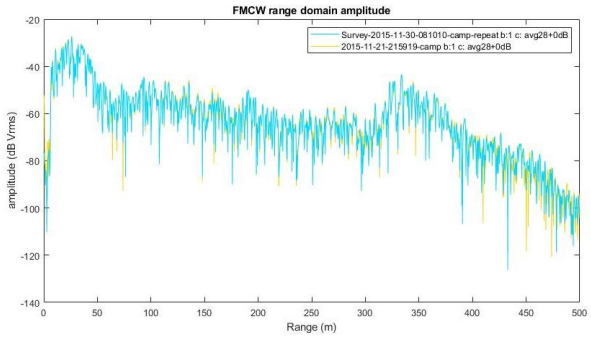

2016

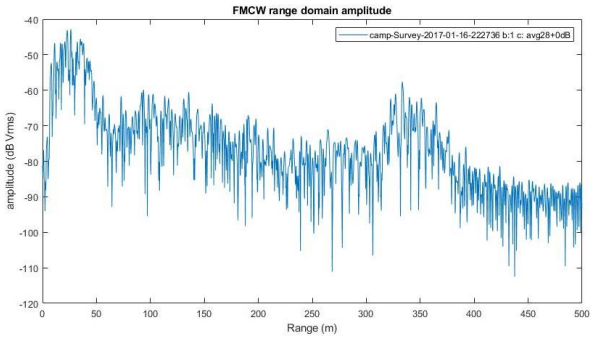

2017 – No measurement

2018

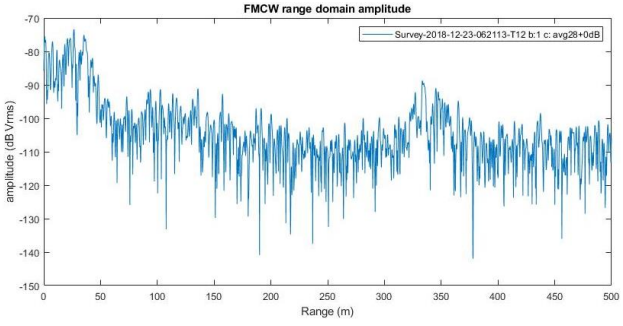

2019

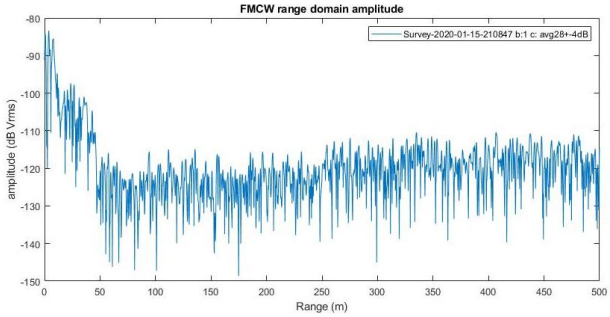

T13

Year	Latitude	Longitude	Attenuation (AVG)	Gain (dB)	Basal reflection uncorrected (m)	Reflection strength	Basal reflection power (dB increase)
2018	-81.0008	175.3327	31	-6	324.8	Moderate	20
2019.2	-80.9956	175.3366	31	-4	324	Very Weak	8

2018

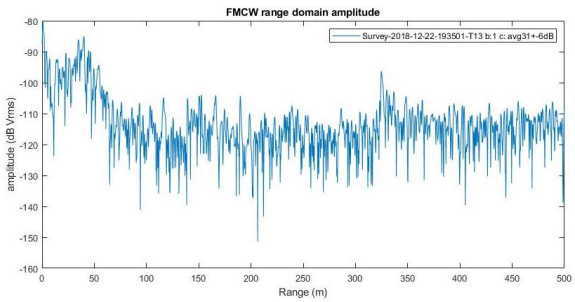

2019

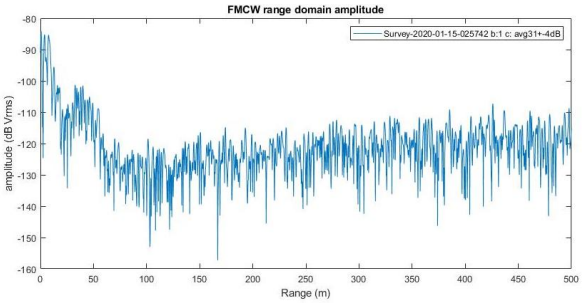

T14

Year	Latitude	Longitude	Attenuation (AVG)	Gain (dB)	Basal reflection uncorrected (m)	Reflection strength	Basal reflection power (dB increase)
2018	-81.3282	176.2769	20	-3	355.3	Moderate	33
2019.2	-81.3233	176.2790	31	-4	355.1	Moderate	28

2018

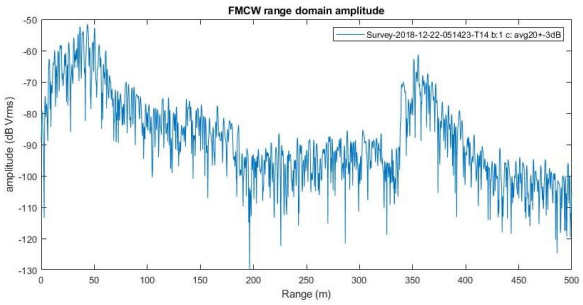

2019

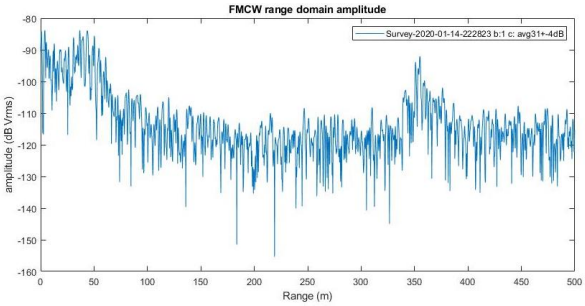

T15

Year	Latitude	Longitude	Attenuation (AVG)	Gain (dB)	Basal reflection uncorrected (m)	Reflection strength	Basal reflection power (dB increase)
2018	-81.6434	177.2730	31	-6	388.7	Moderate	38
2019.1	-81.6383	177.2690	31	-4	385.5	Moderate	15
2019.2			20	6	385.5	Moderate	25

2018

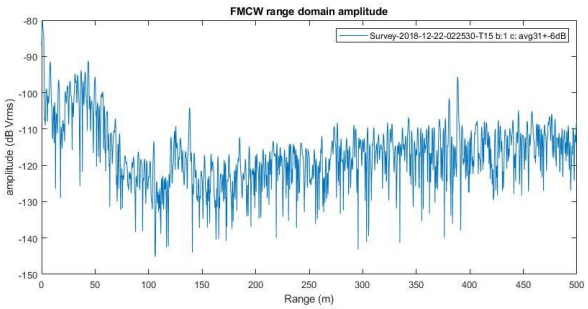

2019

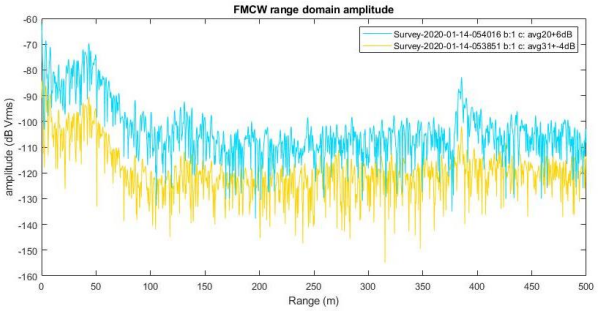

T16

Year	Latitude	Longitude	Attenuation (AVG)	Gain (dB)	Basal reflection uncorrected (m)	Reflection strength	Basal reflection power (dB increase)
2018	-81.9752	178.4184	31	-6	401.5	Weak	6
2019.1	-81.9681	178.4084	31	-4	399.8	Strong	34
2019.2			20	-4	400	Strong	40

2018

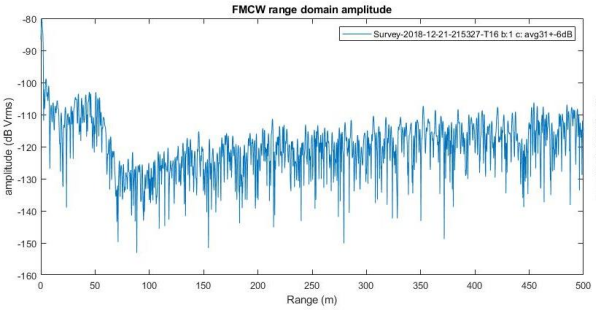

2019

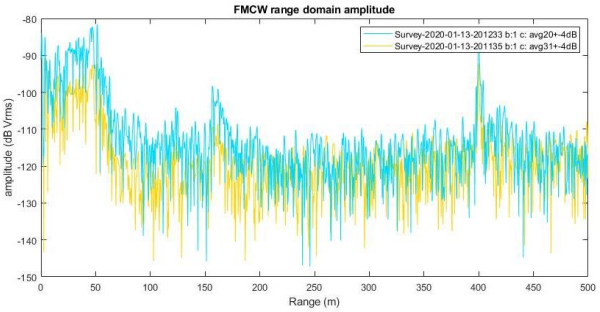

T17

Year	Latitude	Longitude	Attenuation (AVG)	Gain (dB)	Basal reflection uncorrected (m)	Reflection strength	Basal reflection power (dB increase)
2018	-82.3940	-179.9591	31	-6	475.6	Strong	26
2019	-82.3903	-179.9660	31	-4	475.4	Strong	49

2018

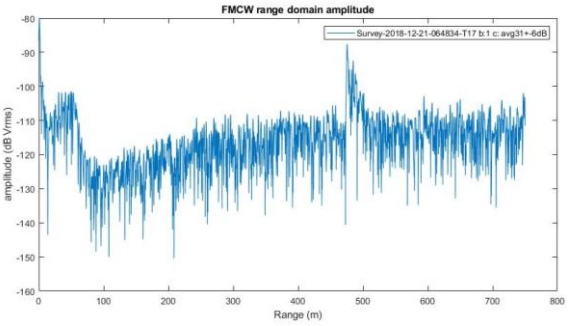

2019

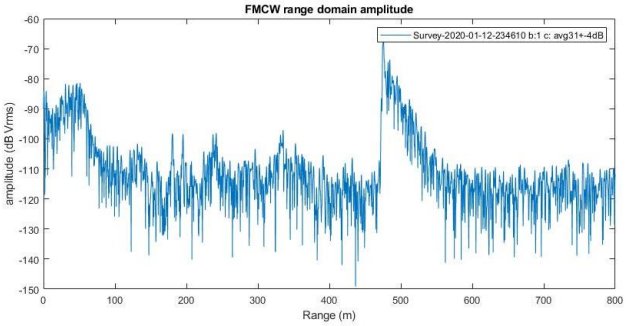

T18

Year	Latitude	Longitude	Attenuation (AVG)	Gain (dB)	Basal reflection uncorrected (m)	Reflection strength	Basal reflection power (dB increase)
2018	-82.8080	-178.1378	31	-6	510.5	Strong	47
2019.1	-82.8046	-178.1463	31	-4	509.9	Strong	40
2019.2			20	-4	509.9	Strong	46

2018

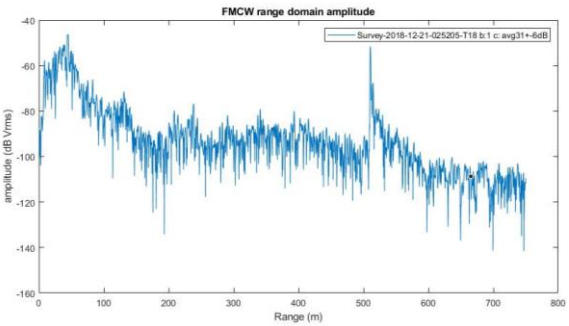

2019

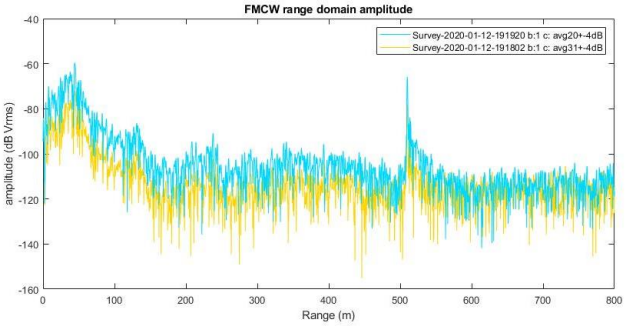

T19

Year	Latitude	Longitude	Attenuation (AVG)	Gain (dB)	Basal reflection uncorrected (m)	Reflection strength	Basal reflection power (dB increase)
2018	-83.2134	-176.1870	31	-6	570.6	Weak	21
2019	-83.2108	-176.2015	20	-4	572.5	Strong	30

2018

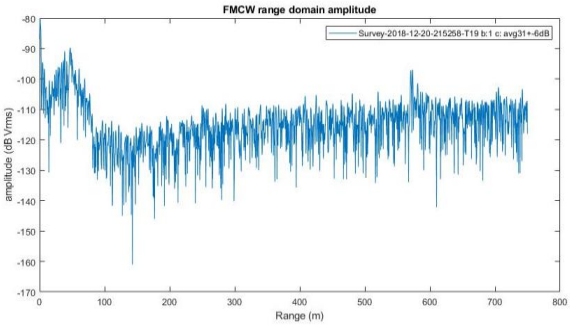

2019

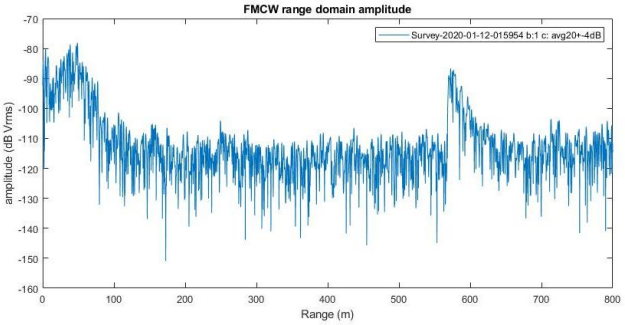

T20

Year	Latitude	Longitude	Attenuation (AVG)	Gain (dB)	Basal reflection uncorrected (m)	Reflection strength	Basal reflection power (dB increase)
2018	-83.5076	-174.7577	31	-6	608.7	Moderate	23
2019.1	-83.5055	-174.7768	31	-4	608.1	Strong	22
2019.2			0	-4	608.1	Strong	36

2018

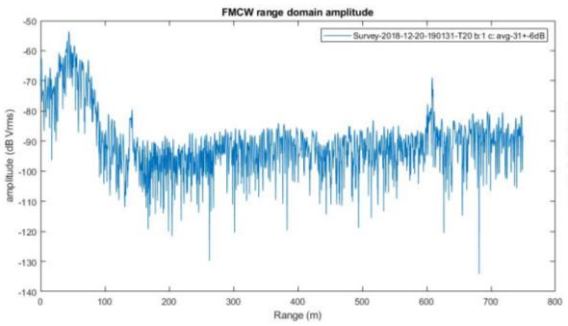

2019

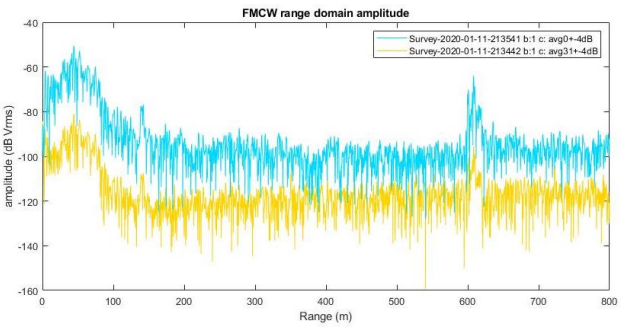

T21

Year	Latitude	Longitude	Attenuation (AVG)	Gain (dB)	Basal reflection uncorrected (m)	Reflection strength	Basal reflection power (dB increase)
2018	-83.7956	-173.2242	31	-6	649.6	Strong	53
2019	-83.7933	-173.2844	31	-4	648.8	Strong	42

2018

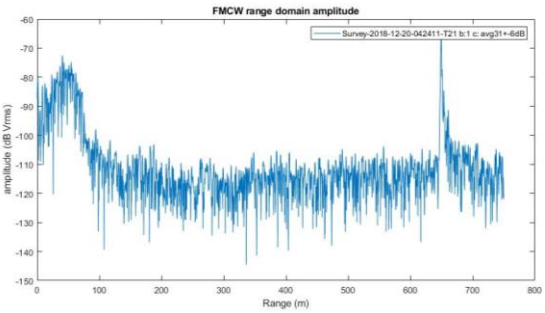

2019

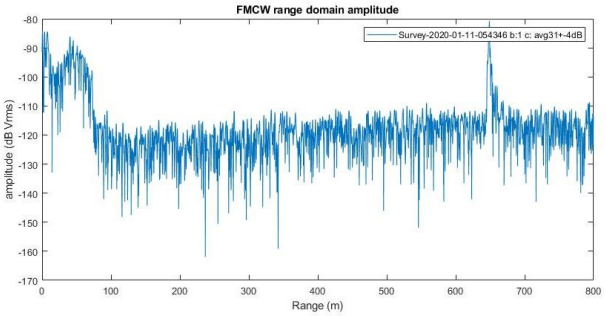

P1

Year	Latitude	Longitude	Attenuation (AVG)	Gain (dB)	Basal reflection uncorrected (m)	Reflection strength	Basal reflection power (dB increase)
2018.1	-84.0555	-171.2785	20	13	688.2	Strong	51
2018.2			15	-3	688.2	Strong	52
2018.3			10	-3	688.2	Strong	50
2018.4			10	-3	688.2	Strong	55
2018.5			10	-3	688.2	Strong	55
2018.6			20	-3	688.2	Strong	55
2018.7			10	-3	688.2	Strong	54
2019.1	-84.0539	-171.2962	20	-14	688	Strong	43
2019.2			20	-14	688	Strong	46
2019.3			0	6	688	Strong	52

2018

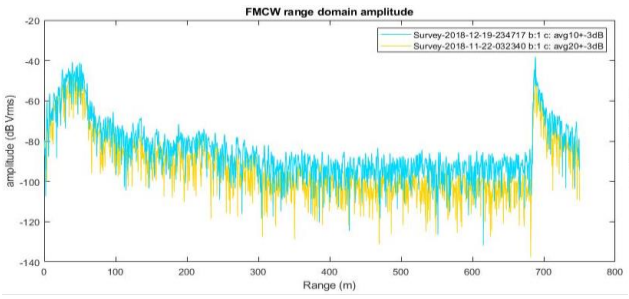

2019

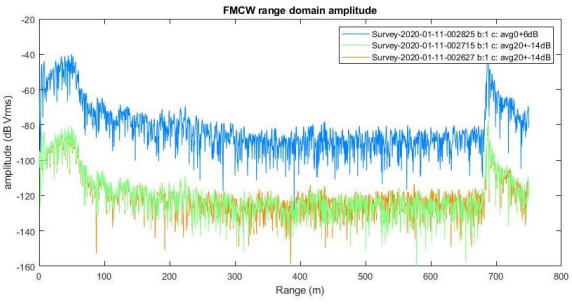

P2

Year	Latitude	Longitude	Attenuation (AVG)	Gain (dB)	Basal reflection uncorrected (m)	Reflection strength	Basal reflection power (dB increase)
2018.1	-83.9663	-169.3753	31	-6	693.7	Strong	63
2018.2			31	-6	693.7	Strong	55
2019.1	-83.9655	-169.3926	20	-4	693.7	Strong	59
2019.2			0	-4	693.7	Strong	38

2018

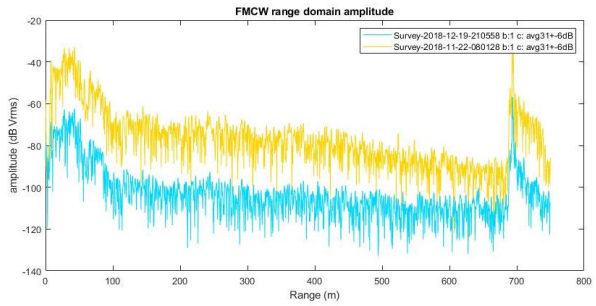

2019

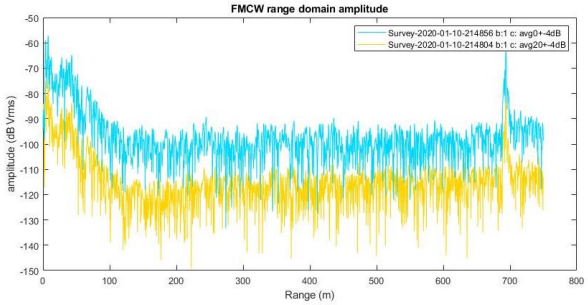

P3

Year	Latitude	Longitude	Attenuation (AVG)	Gain (dB)	Basal reflection uncorrected (m)	Reflection strength	Basal reflection power (dB increase)
2018.1	-83.8678	-167.2865	20	-3	702.7	Strong	54
2018.2			20	0	702.7	Strong	53
2018.3			20	0	702.7	Strong	54
2019.1	-83.8672	-167.3138	20	-4	702.9	Strong	57
2019.2			20	6	702.9	Strong	56

2018

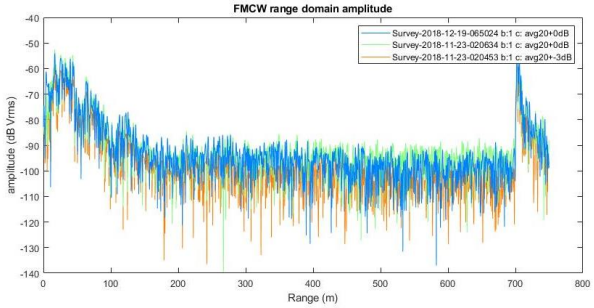

2019

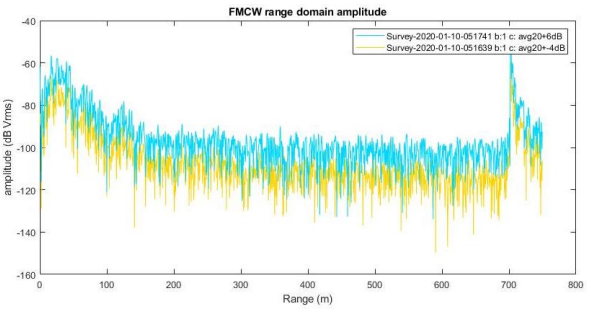

P4

Year	Latitude	Longitude	Attenuation (AVG)	Gain (dB)	Basal reflection uncorrected (m)	Reflection strength	Basal reflection power (dB increase)
2018.1	-83.2982	-163.6510	20	0	578.3	Strong	51
2018.2			20	-3	578.3	Strong	51
2018.3			20	-3	578.3	Strong	54
2019	-83.2978	-163.6540	20	-4	578.3	Strong	54

2018

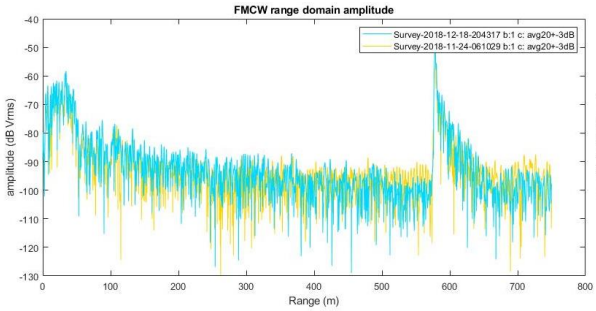

2019

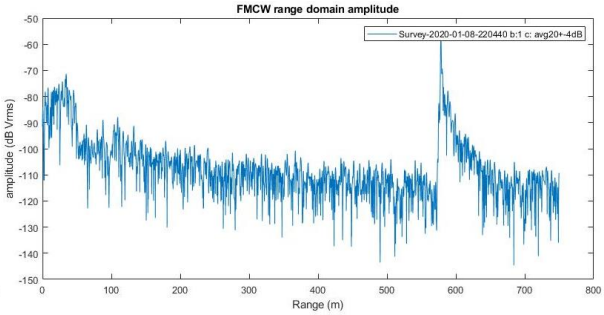

P5

Year	Latitude	Longitude	Attenuation (AVG)	Gain (dB)	Basal reflection uncorrected (m)	Reflection strength	Basal reflection power (dB increase)
2018.1	-83.0489	-163.9290	20	0	509.7	Strong	39
2018.2			31	-3	509.7	Strong	38
2018.3			31	-3	509.7	Strong	51
2019.1	-83.0471	-163.9357	20	-4	509.5	Strong	40
2019.2			31	-4	509.5	Strong	32

2018

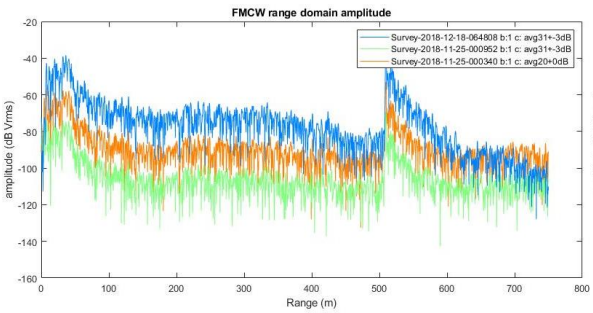

2019

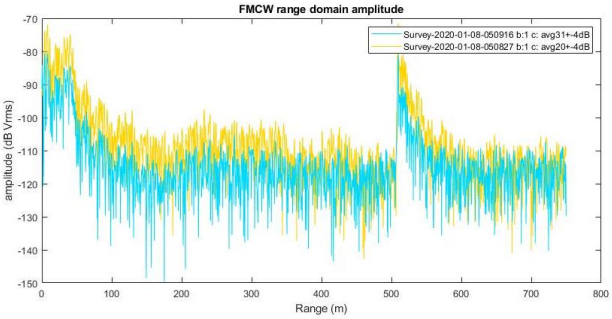

P6

Year	Latitude	Longitude	Attenuation (AVG)	Gain (dB)	Basal reflection uncorrected (m)	Reflection strength	Basal reflection power (dB increase)
2018.1	-82.7147	-163.1425	15	0	503.9	Moderate	24
2018.2			15	0	503.7	Moderate	19
2019.1	-82.7138	-163.1502	5	-4	503.7	Moderate	31
20192			20	6	503.7	Moderate	29

2018

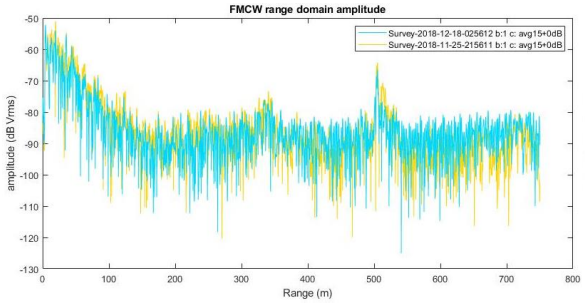

2019

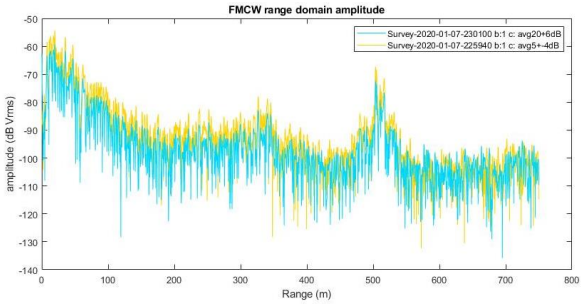

P7

Year	Latitude	Longitude	Attenuation (AVG)	Gain (dB)	Basal reflection uncorrected (m)	Reflection strength	Basal reflection power (dB increase)
2018.1	-82.5296	-162.2322	31	-3	475	Strong	50
2018.2			31	-3	475	Strong	39
2019	-82.5290	-162.2371	0	-4	474.5	Strong	44

2018

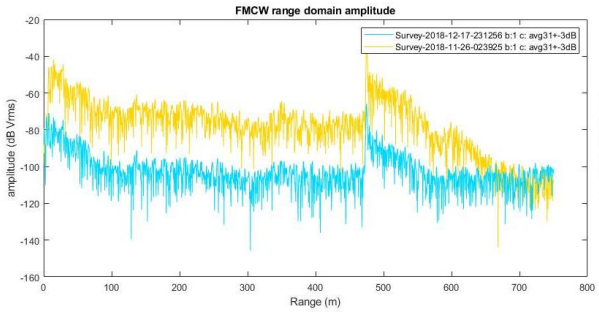

2019

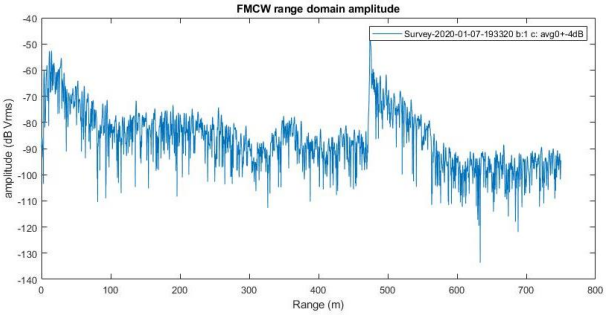

P8

Year	Latitude	Longitude	Attenuation (AVG)	Gain (dB)	Basal reflection uncorrected (m)	Reflection strength	Basal reflection power (dB increase)
2018.1	-82.6392	-160.9296	31	-3	484.8	Strong	31
2018.2			31	-3	484.8	Strong	33
2019	-82.6388	-160.9333	0	-4	484.3	Strong	34

2018

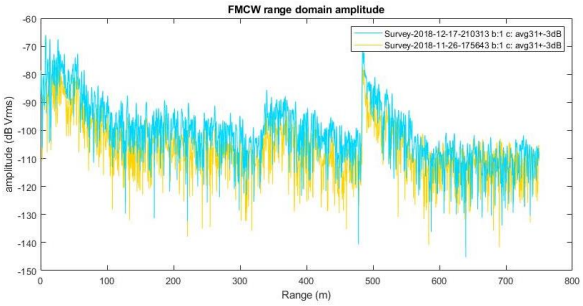

2019

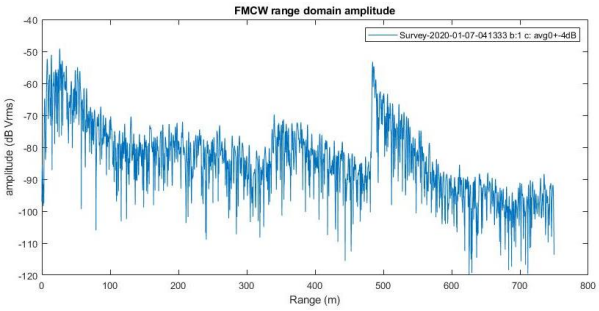

P9

Year	Latitude	Longitude	Attenuation (AVG)	Gain (dB)	Basal reflection uncorrected (m)	Reflection strength	Basal reflection power (dB increase)
2018.1	-82.7299	-158.4670	31	0	535.2	Strong	48
2018.2			31	0	535.2	Strong	42
2019	-82.7298	-158.4688	0	6	534.8	Strong	48

2018

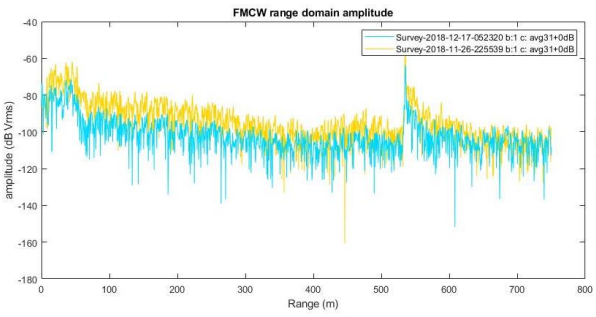

2019

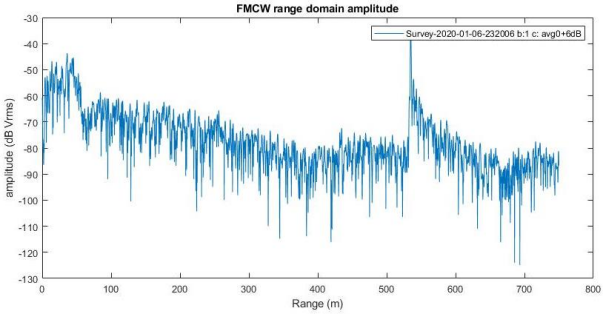

P10

Year	Latitude	Longitude	Attenuation (AVG)	Gain (dB)	Basal reflection uncorrected (m)	Reflection strength	Basal reflection power (dB increase)
2018.1	-82.7707	-156.5794	31	-3	583	Strong	48
2018.2			31	-3	583	Strong	37
2019	-82.7707	-156.5802	0	6	582.5	Strong	50

2018

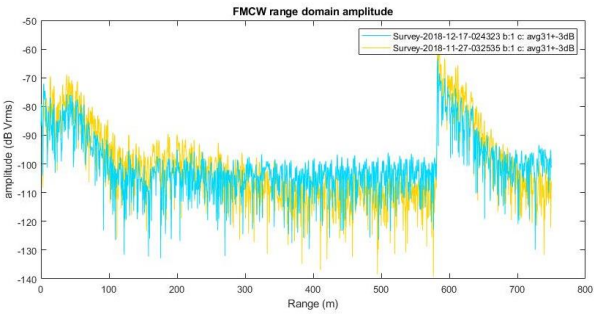

2019

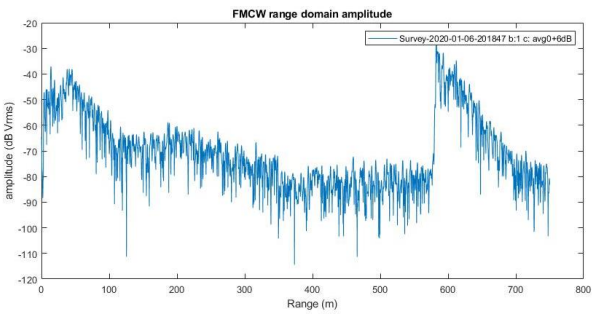

P11

Year	Latitude	Longitude	Attenuation (AVG)	Gain (dB)	Basal reflection uncorrected (m)	Reflection strength	Basal reflection power (dB increase)
2018.1	-82.7816	-155.5314	31	0	583.6	Strong	38
2018.2			31	0	583.8	Strong	52
2019	-82.7815	-155.5316	30	-4	583.2	Strong	46
Old			30	0	583.4	Weak	17

2018

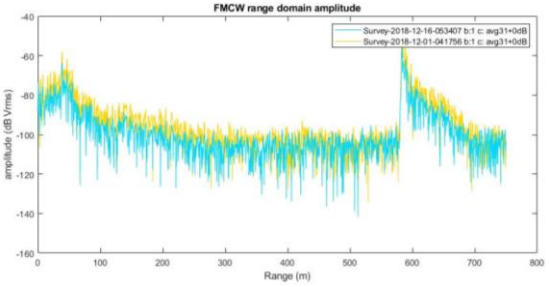

2019

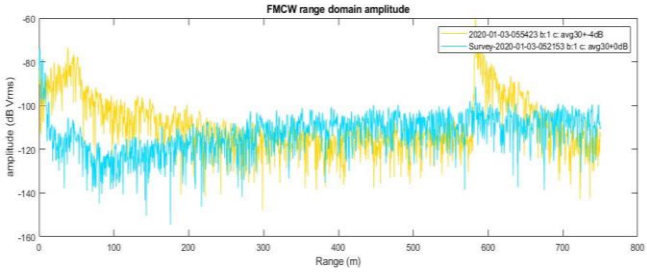

- *Blue -original pRES instrument*
  Yellow - new pRES instrument

Appendix C. Site Strain and Melt Rate Processing Outputs

Years denotes the year(s) of coverage between two summer measurements. Figures both show co-registered amplitude-range profiles in the upper panels. Bottom left displays matched internal layers and trend chosen from high correlation layer matches. Middle right shows phase information from both profiles. Bottom right shows modelled linear internal layer range changes projected to the basal thickness change. The residual is marked as basal melting.

T1

Year	Repeat time (Days)	Correg Shift (m)	Correg Correlation	Thickness change (m)	Strain Rate (/yr)	Error (/yr)	R^2	P	Melt (m)	Error (m)	Melt Rate (m/yr)	Melt Rate Error (m/yr)
2016	427	0.20	0.98	-0.878	-0.00111	9.00E-05	0.038	0.27786	0.403	0.023	0.344	0.020
2017	304	0.09	0.94	-1.065	-0.00109	3.86E-05	0.957	5.47E-29	0.799	0.006	0.961	0.007
2019	388	-0.06	0.94	-0.822	-0.00147	5.12E-05	0.985	1.68E-10	0.470	0.013	0.442	0.013
2015-16	717	0.30	0.93	-1.652	-0.00113	3.25E-05	0.977	2.78E-21	0.890	0.014	0.454	0.007
2018-19	791	0.11	0.93	-1.737	-0.00113	2.67E-05	0.992	2.56E-19	1.021	0.013	0.471	0.006

2016

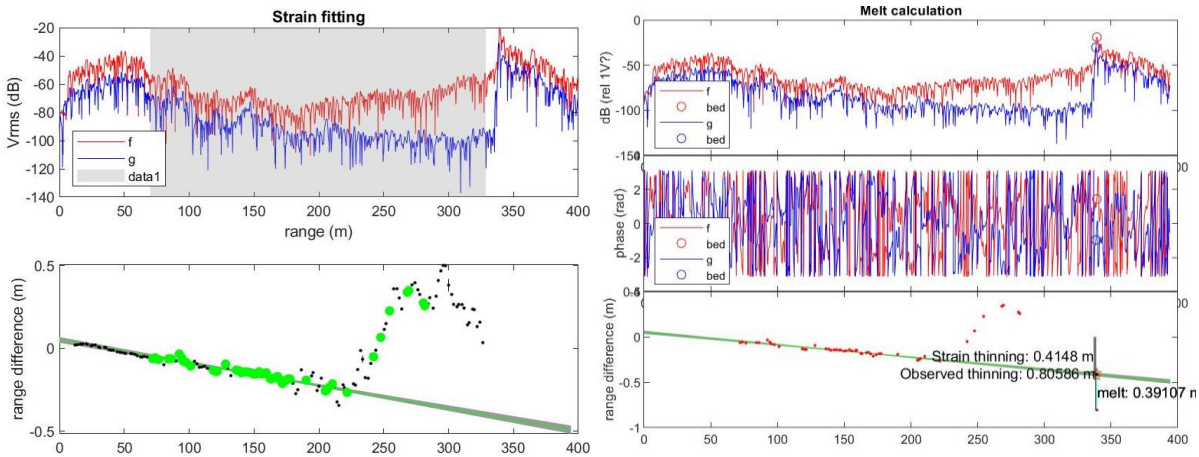

2017

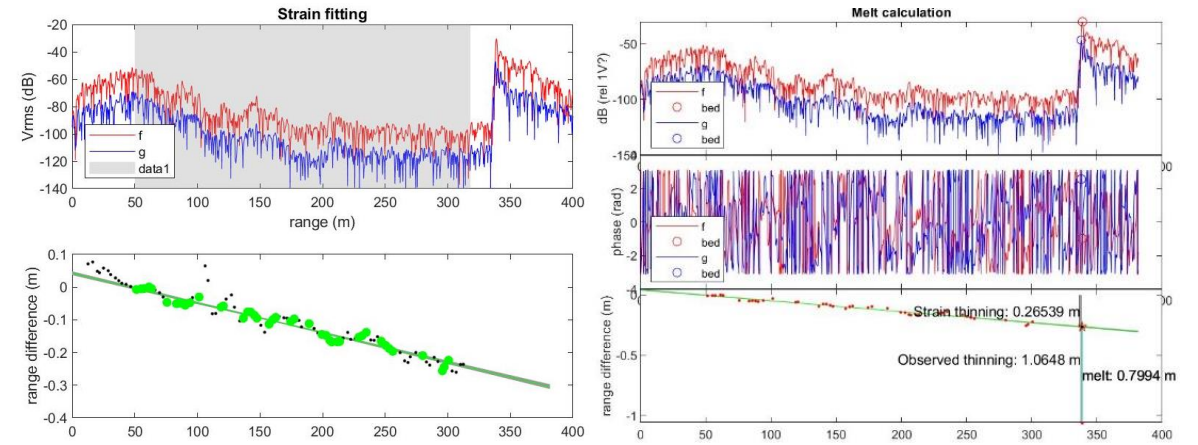

2018 – Poor correlation

2019

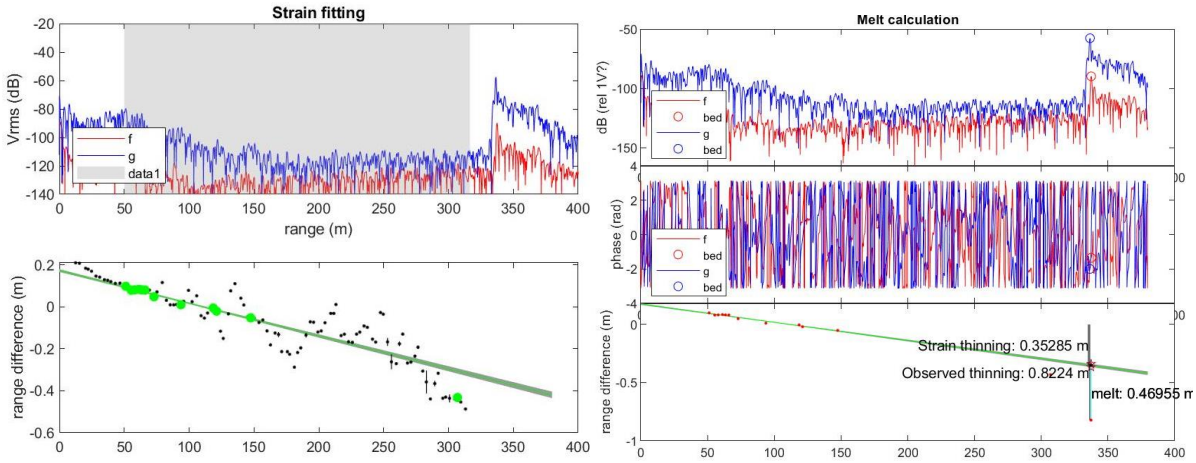

2016-17

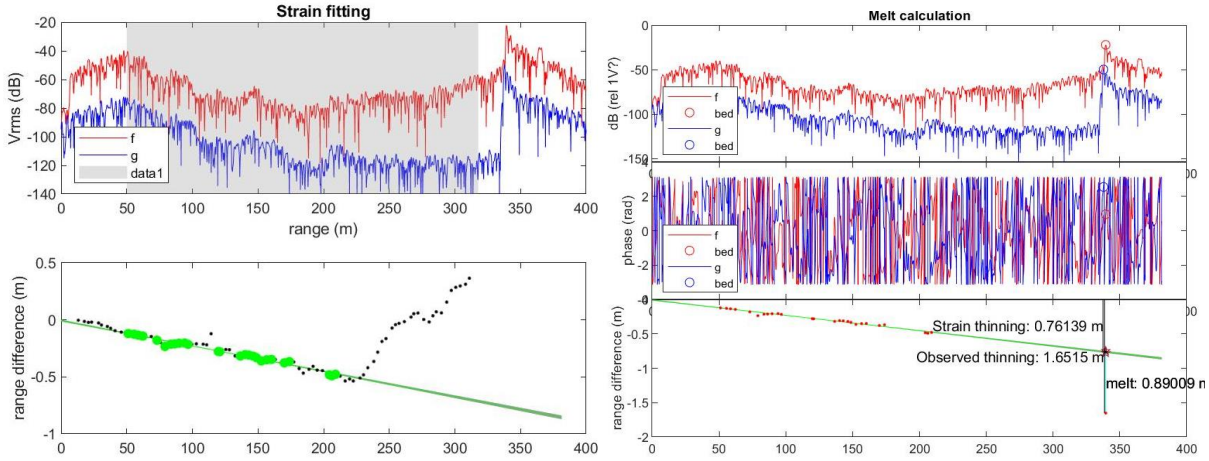

2018-19

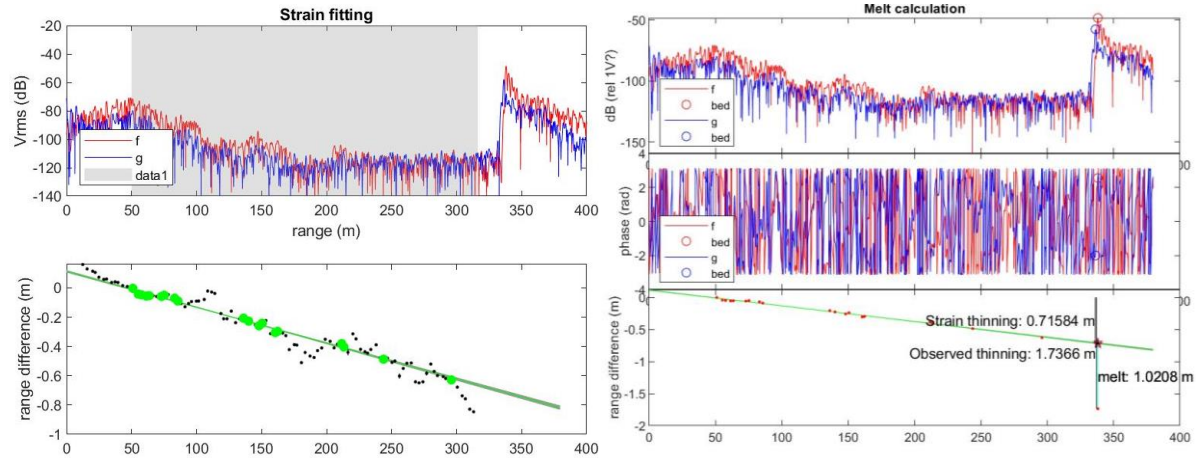

T2

Year	Repeat time (Days)	Correg Shift (m)	Correg Correlation	Thickness change (m)	Strain Rate (/yr)	Error (/yr)	R^2	P	Melt (m)	Error (m)	Melt Rate (m/yr)	Melt Rate Error (m/yr)
2016	413	0.11	0.97	-0.574	-7.99E-04	5.0E-05	0.88	1.3E-15	0.273	0.015	0.242	0.013
2017	304	0.17	0.93	-0.710	-8.60E-04	1.5E-04	0.68	7.2E-06	0.327	0.035	0.393	0.041
2019	389	0.04	0.85	-0.394	-0.00108	7.1E-05	0.96	1.3E-09	-0.072	0.021	-0.067	0.020
20161 7	717	0.30	0.96	-1.297	-0.00101	4.1E-05	0.97	8.7E-17	0.789	0.023	0.402	0.012
2018-19	791	0.30	0.91	-1.263	-9.46E-04	4.8E-05	0.97	9.4E-10	0.594	0.030	0.274	0.014

2016

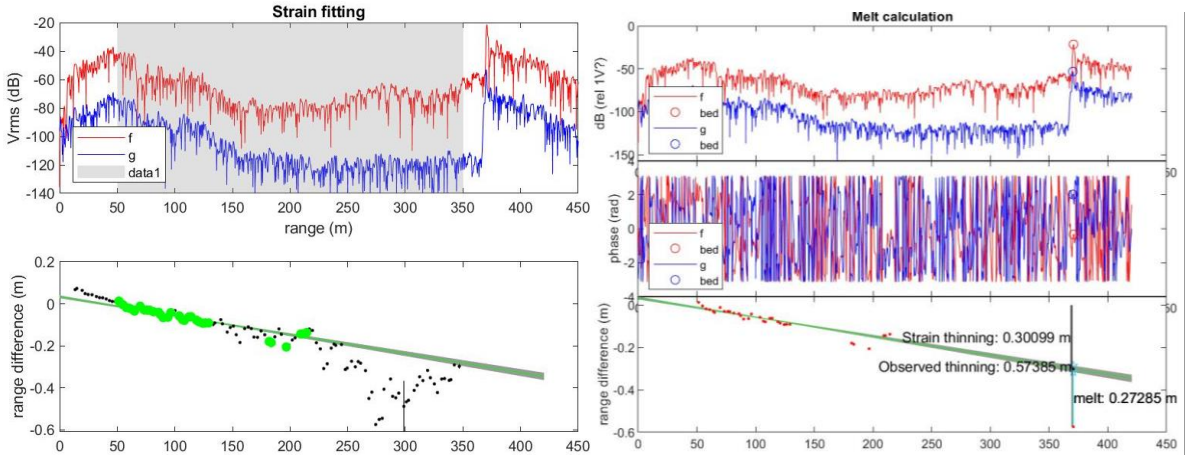

2017

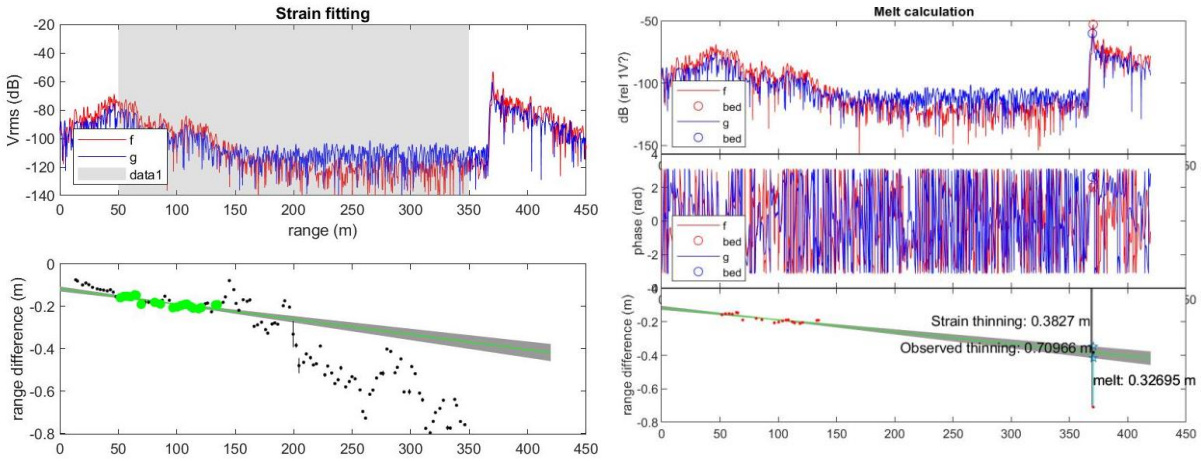

2018– No analysis

2019

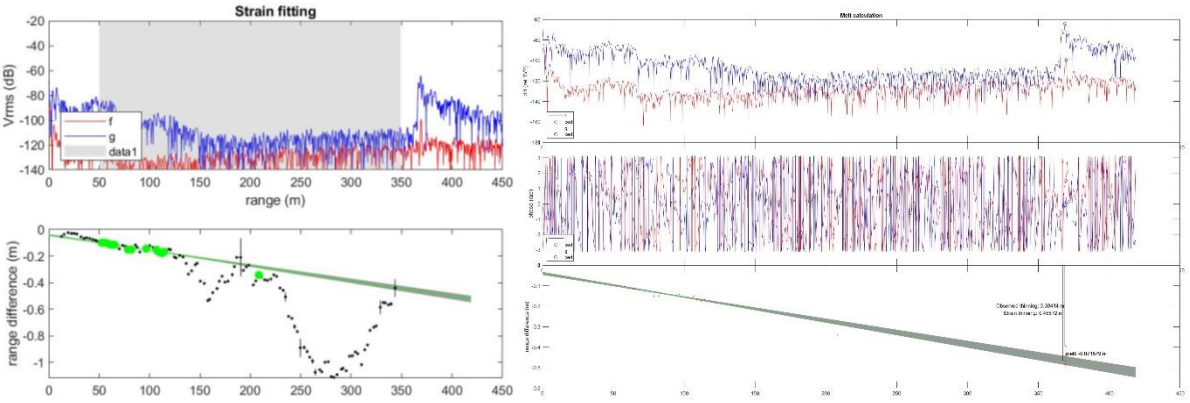

2016-17

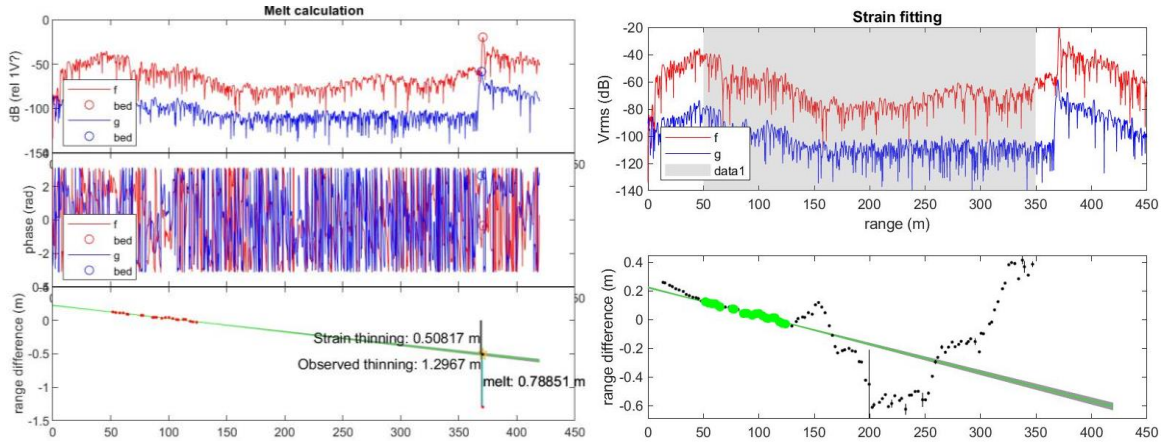

2018-19

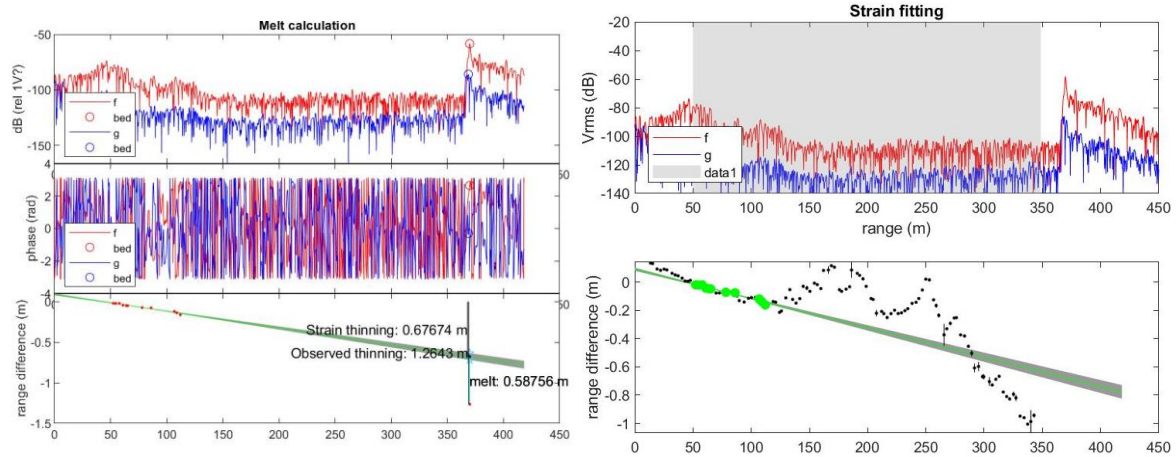

T3

Year	Repeat time (Days)	Correg Shift (m)	Upper Correlation	Thickness change (m)	Strain Rate (/yr)	Error (/yr)	R^2	P	Melt (m)	Error (m)	Melt Rate (m/yr)	Melt Rate Error (m/yr)
2016	427	0.06	0.99	-0.338	-4.67E-04	2.5E-05	0.26	7.1E-07	0.144	0.006	0.124	0.005
2017	304	0.26	1.00	-0.435	-0.00122	5.4E-05	0.86	4.7E-43	0.075	0.009	0.090	0.011

2016

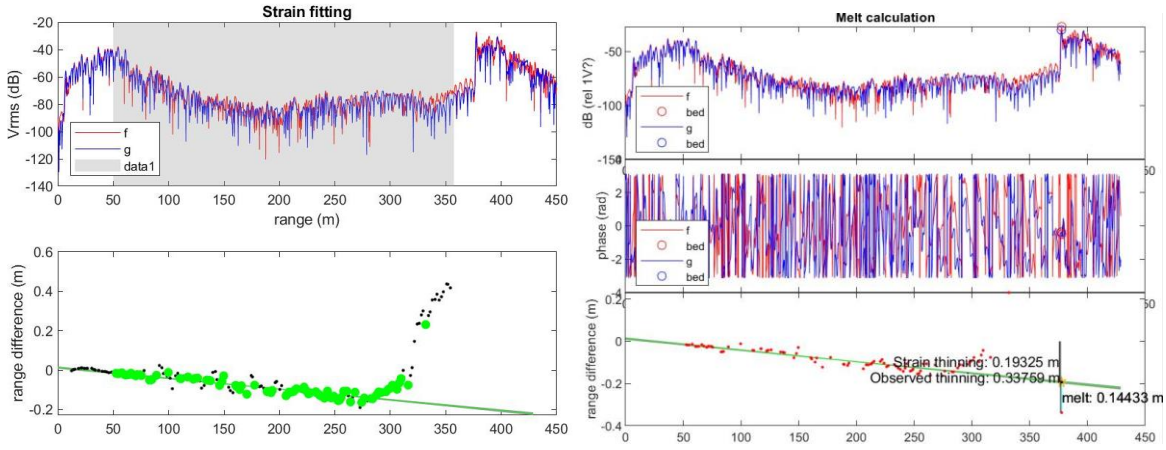

2017 – Lower 100m removed due to signal clipping

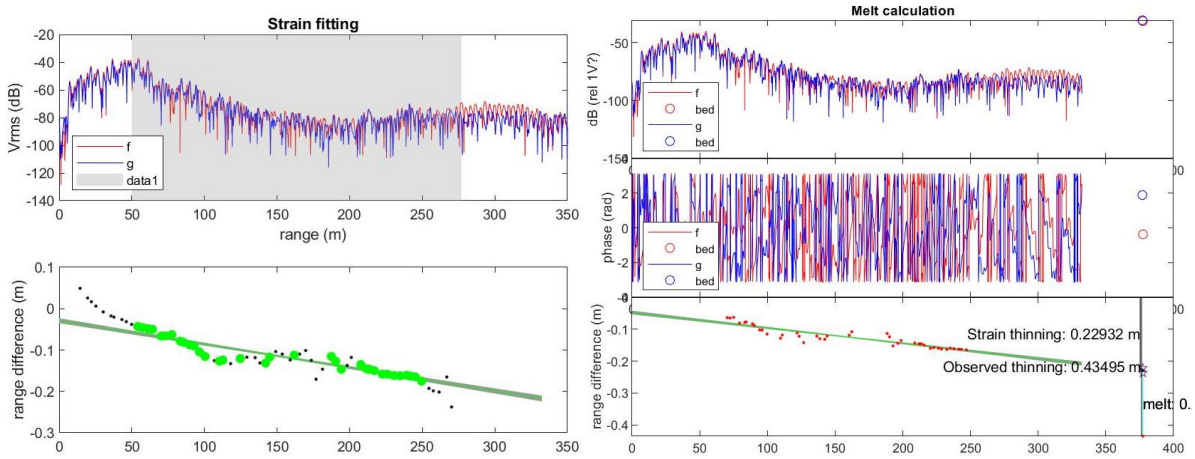

T4

Year	Repeat time (Days)	Correg Shift (m)	Upper Correlation	Thickness change (m)	Strain Rate (/yr)	Error (/yr)	R^2	P	Melt (m)	Error (m)	Melt Rate (m/yr)	Melt Rate Error (m/yr)
2016	413	0.09	0.93	-0.333	-2.60E-04	2.0E-05	0.37	5.3E-12	0.096	0.005	0.085	0.005
2017	304	0.30	0.95	-0.152	-4.60E-04	1.9E-05	0.81	5.5E-50	0.005	0.003	0.006	0.004
2018	402		0.91	0.040	-2.90E-04	3.6E-05	0.03	9.9E-02	-0.144	0.010	-0.131	0.009

2016

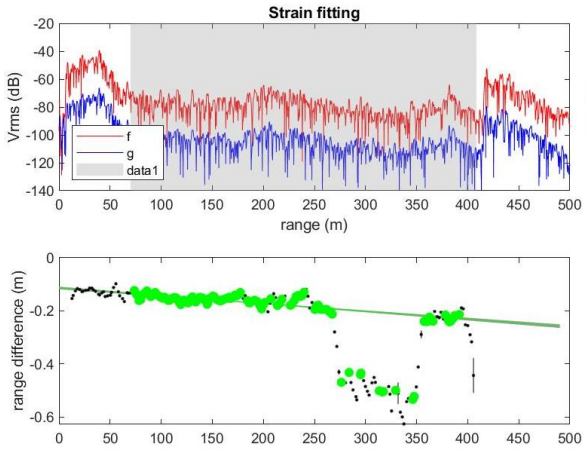

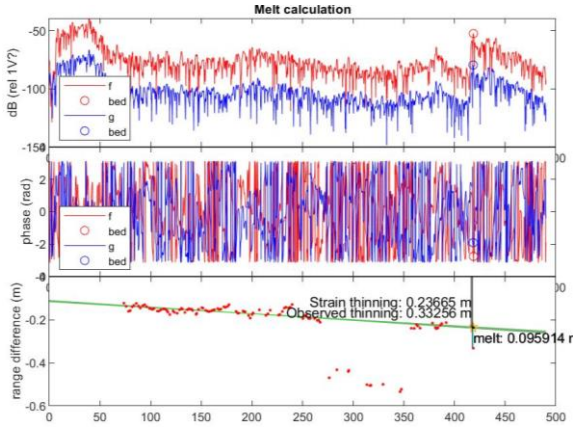

2017

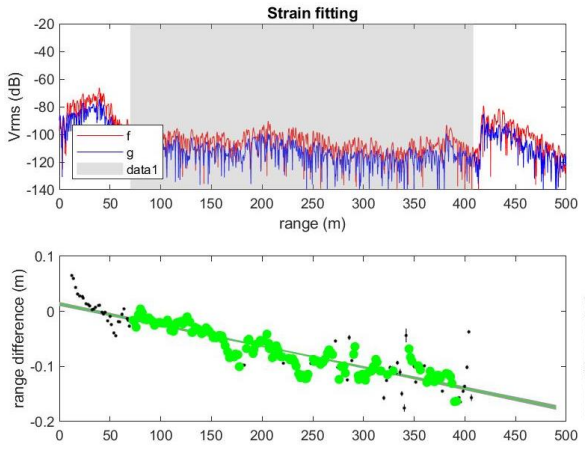

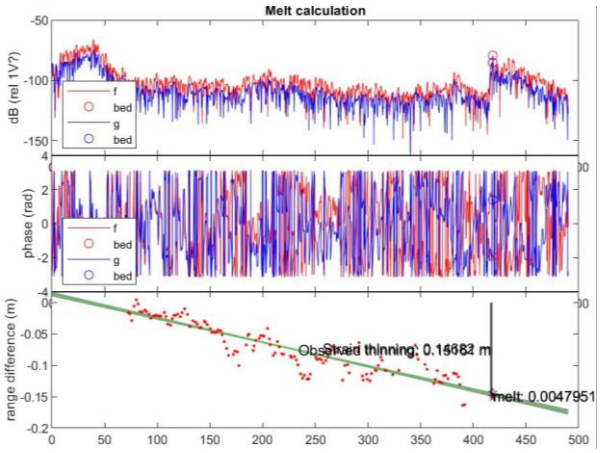

2018

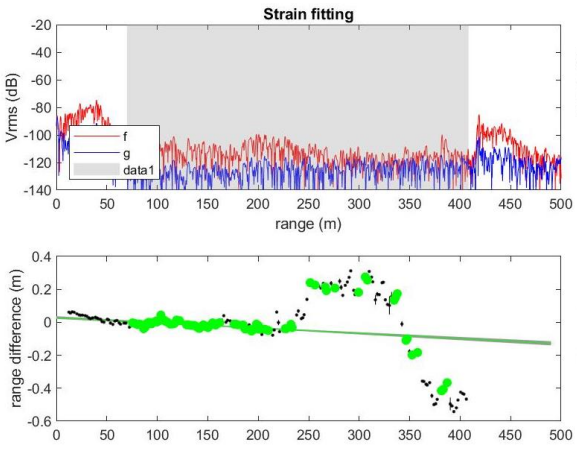

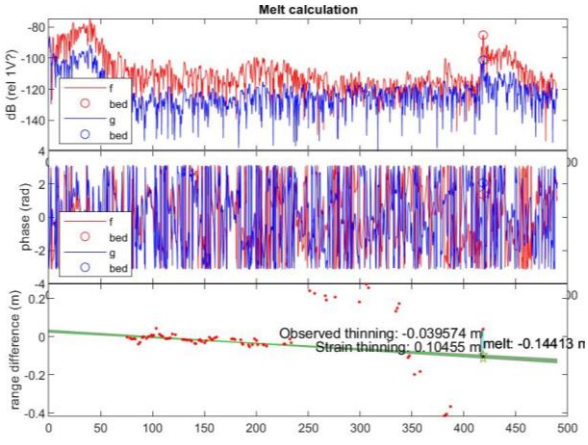

T5

Year	Repeat time (Days)	Correg Shift (m)	Correg Correlation	Thickness change (m)	Strain Rate (/yr)	Error (/yr)	R^2	P	Melt (m)	Error (m)	Melt Rate (m/yr)	Melt Rate Error (m/yr)
2016	421	0.17	0.97	-0.263	-5.13E-04	1.0E-05	0.95	4.2E-69	-0.015	0.002	-0.013	0.002
2017	296	0.256	0.97	-0.098	-5.72E-04	1.3E-05	0.94	1.2E-72	-0.022	0.002	-0.027	0.003

2016

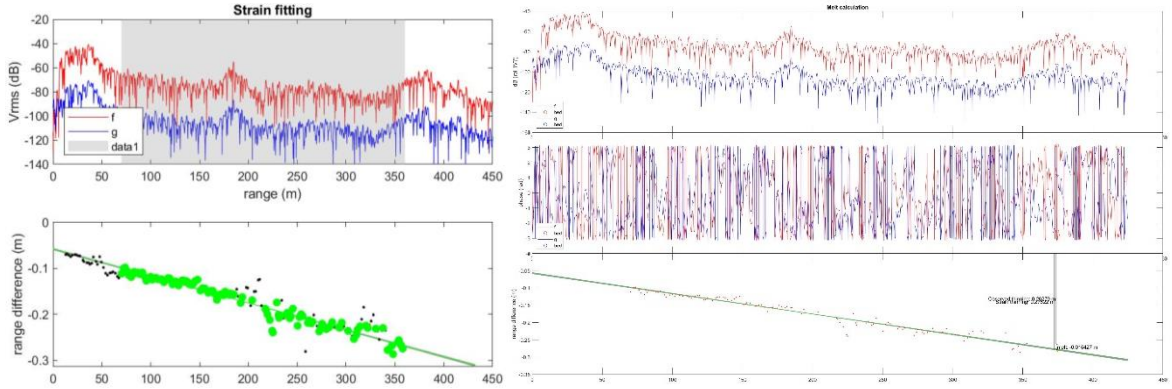

2017

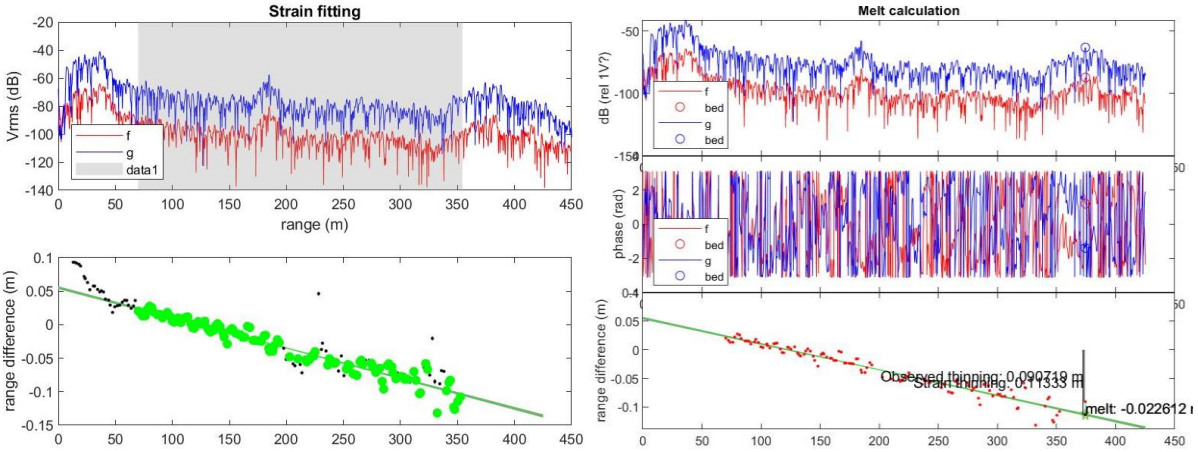

T6

Year	Repeat time (Days)	Correg Shift (m)	Correg Correlation	Strain Rate (/yr)	Error (/yr)	R^2	P
2016	420.9217	0.12779	0.96105	-4.25E-04	1.12E-05	0.955	7.79E-43
2017	296.4622	0.25559	0.9531	-4.59E-04	2.49E-05	0.88	1.66E-26

2016

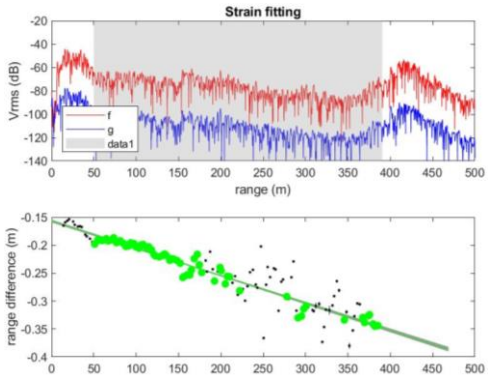

2017

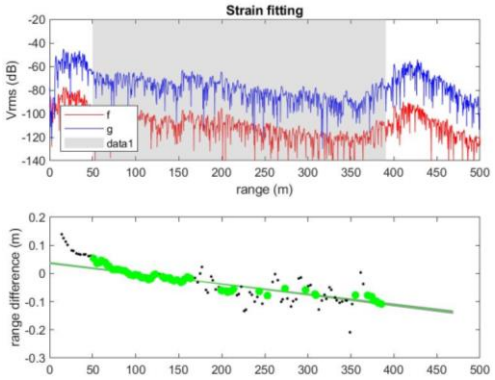

T7

Year	Repeat time (Days)	Correg Shift (m)	Correg Correlation	Thickness change (m)	Strain Rate (/yr)	Error (/yr)	R^2	P	Melt (m)	Error (m)	Melt Rate (m/yr)	Melt Rate Error (m/yr)
2017-18	789	0.09	0.96	-0.343	-4.71E-04	9.98E-06	0.89	2.9E-51	-0.002	0.005	-0.001	0.002

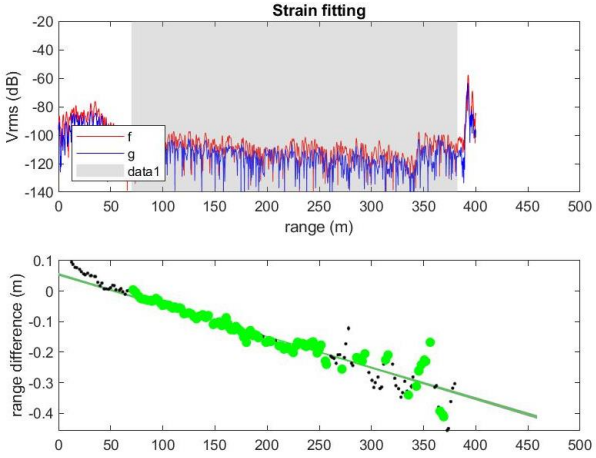

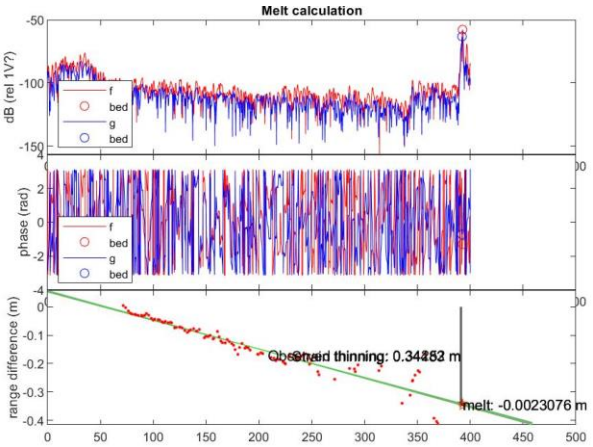

T8

Repeat time (Days)	Correg Shift (m)	Upper Correlation	Thickness change (m)	Strain Rate (/yr)	Error (/yr)	R^2	P	Melt (m)	Error (m)	Melt Rate (m/yr)	Melt Rate Error (m/yr)
789	0.19	0.95	-0.402	-5.11E-04	1.64E-05	0.9757	5.8E-25	0.013	0.008	0.006	0.004

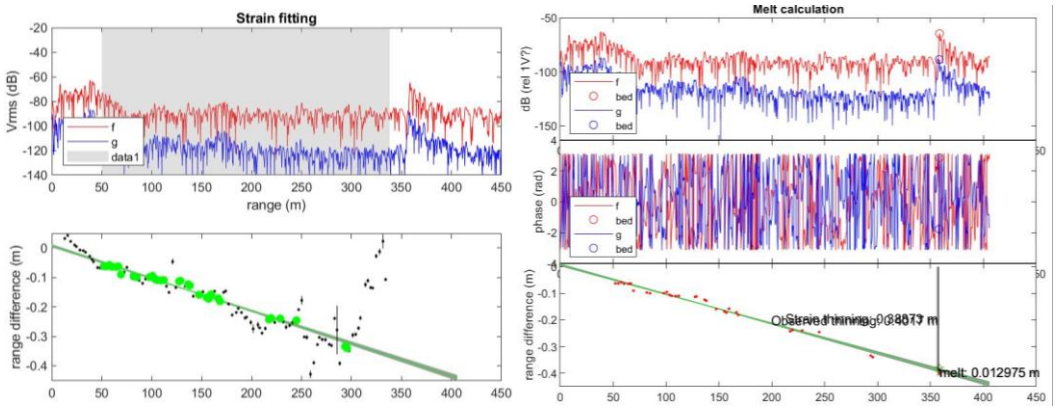

T9

Repeat time (Days)	Correg Shift (m)	Upper Correlation	Thickness change (m)	Strain Rate (/yr)	Error (/yr)	R^2	P	Melt (m)	Error (m)	Melt Rate (m/yr)	Melt Rate Error (m/yr)
719	0.17	0.93	-0.263	-4.40E-04	1.10E-05	0.9184	7.3E-29	0.035	0.004	0.018	0.002

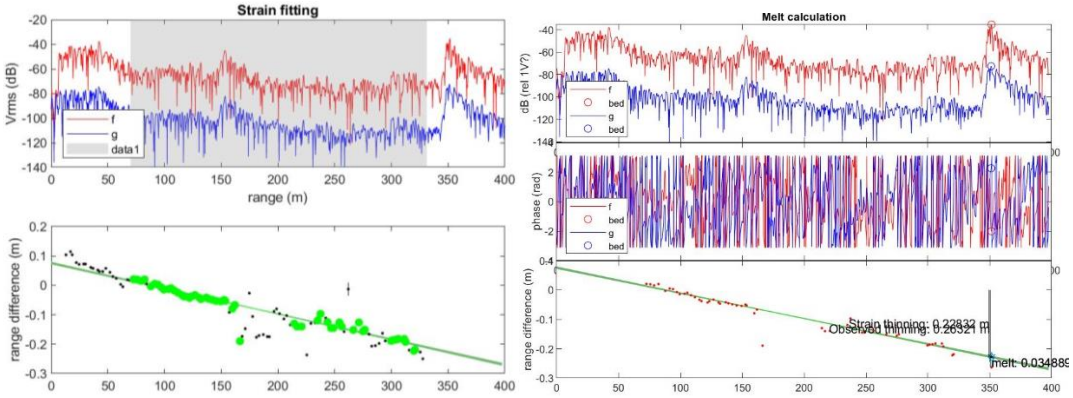

T10

Year	Repeat time (Days)	Correg Shift (m)	Correg Correlation	Thickness change (m)	Strain Rate (/yr)	Error (/yr)	R^2	P	Melt (m)	Error (m)	Melt Rate (m/yr)	Melt Rate Error (m/yr)
2016-17	718.92	0	0.88	-1.3177	-4.53E-04	1.94E-05	0.20	9.34E-05	1.177	0.008	0.598	0.004

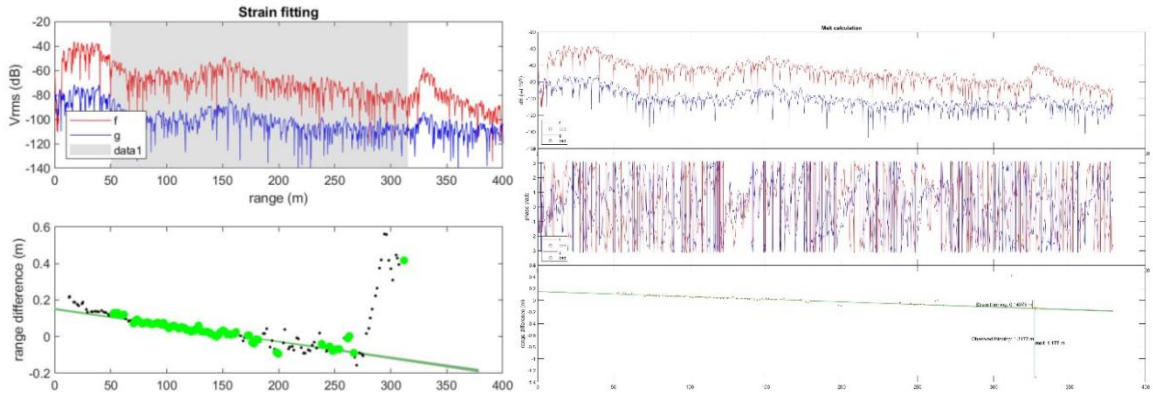

T11

Year	Repeat time (Days)	Correg Shift (m)	Correg Correlation	Thickness change (m)	Strain Rate (/yr)	Error (/yr)	R^2	P	Melt (m)	Error (m)	Melt Rate (m/yr)	Melt Rate Error (m/yr)
2016-17	729.89	-0.02	0.93	2.916	-5.41E-04	1.15E-05	0.97	7.45E-58	-3.082	0.004	-1.542	0.002

2015-2016

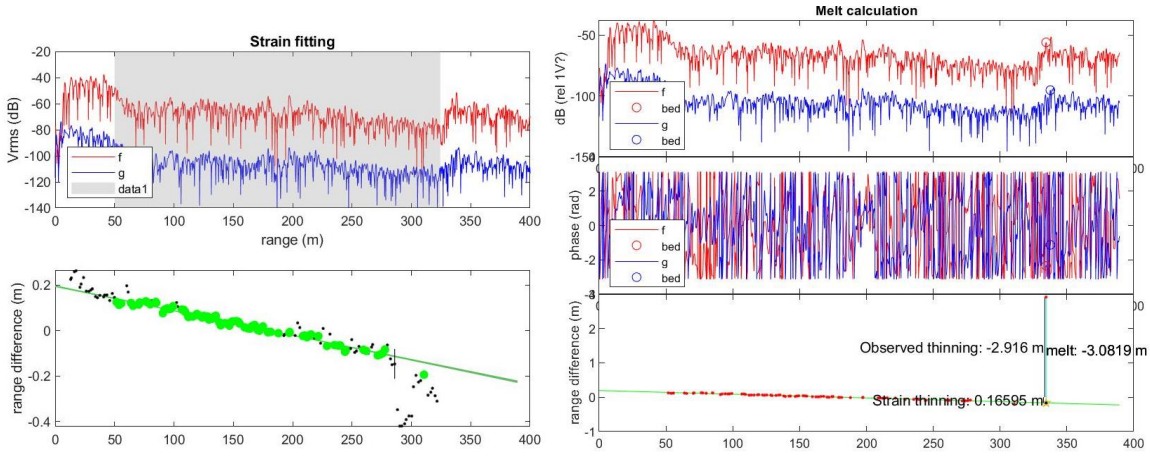

T12

Year	Repeat time (Days)	Correg Shift (m)	Correg Correlation	Thickness change (m)	Strain Rate (/yr)	Error (/yr)	R^2	P	Melt (m)	Error (m)	Melt Rate (m/yr)	Melt Rate Error (m/yr)
2015	422.02	0.064	0.99	-0.1342	-4.98E-04	8.41E-06	0.95	5.36E-77	-0.019	0.002	-0.017	0.002

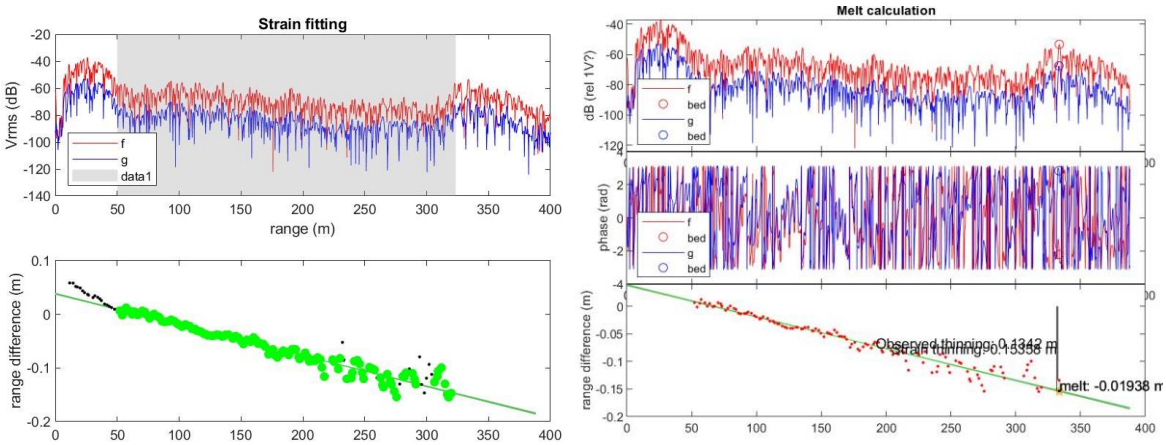

This measurement of basal change using the highest basal reflection from these profiles is deemed inaccurate due to the measured ice thickness of 370m exceeding the pRES interpreted thickness.

T13

Unable to resolve strain or melt rates.

T14

Year	Repeat time (Days)	Correg Shift (m)	Correg Correlation	Thickness change (m)	Strain Rate (/yr)	Error (/yr)	R^2	P	Melt (m)	Error (m)	Melt Rate (m/yr)	Melt Rate Error (m/yr)
2019	389	0.064	0.95	-0.271	-8.95E-04	3.03E-05	0.70	1.74E-18	0.013	0.007	0.012	0.007

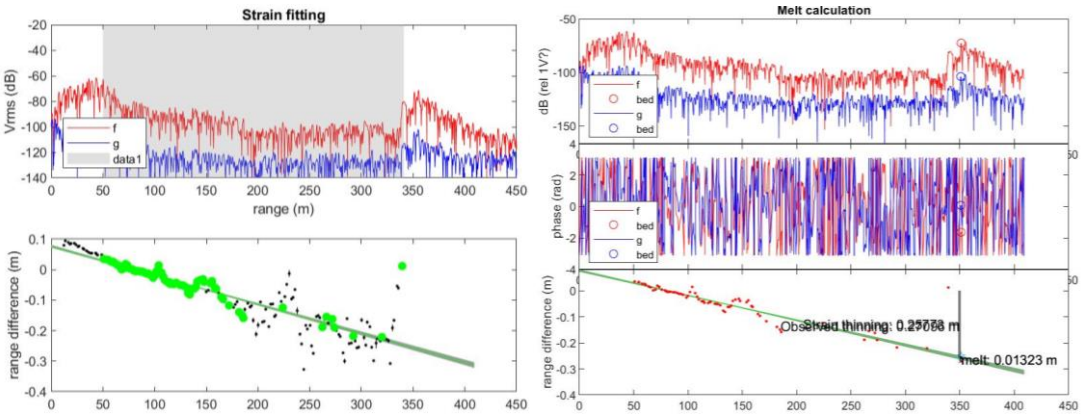

T15

Unable to resolve strain or melt rates.

T16

Unable to resolve strain or melt rates.

T17

Year	Repeat time (Days)	Correg Shift (m)	Correg Correlation	Thickness change (m)	Strain Rate (/yr)	Error (/yr)	R^2	P	Melt (m)	Error (m)	Melt Rate (m/yr)	Melt Rate Error (m/yr)
2019	388	-0.043	0.94	-0.551	-0.0013	6.01E-06	1.00	1.1E-213	0.025	0.002	0.024	0.002

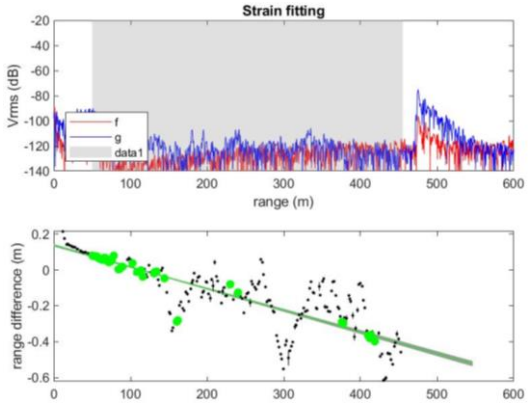

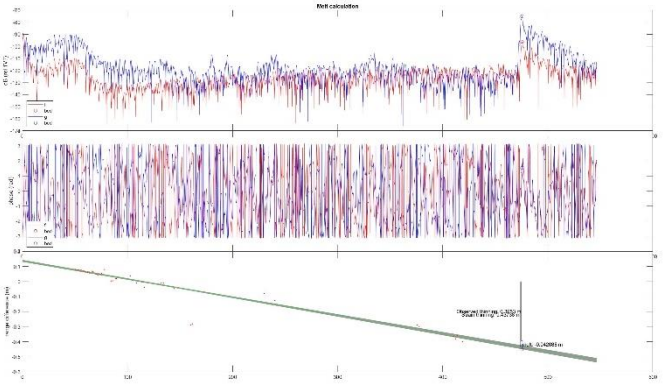

T18

Year	Repeat time (Days)	Correg Shift (m)	Correg Correlation	Thickness change (m)	Strain Rate (/yr)	Error (/yr)	R^2	P	Melt (m)	Error (m)	Melt Rate (m/yr)	Melt Rate Error (m/yr)
2019	388	-0.043	0.94	-0.551	-0.0013	6.01E-06	1.00	1.1E-213	0.025	0.002	0.024	0.002

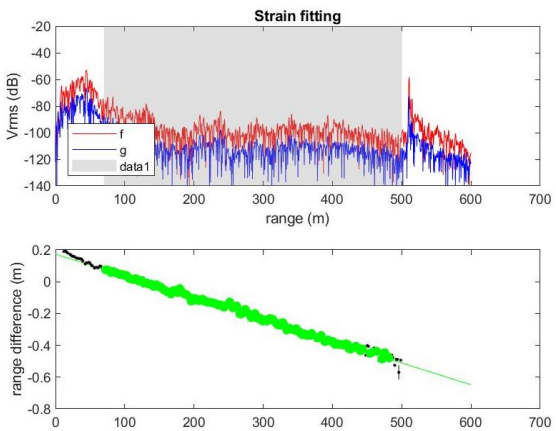

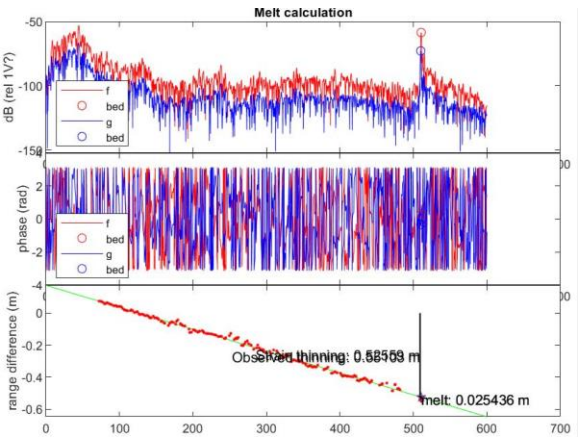

T19

Year	Repeat time (Days)	Correg Shift (m)	Correg Correlation	Thickness change (m)	Strain Rate (/yr)	Error (/yr)	R^2	P	Melt (m)	Error (m)	Melt Rate (m/yr)	Melt Rate Error (m/yr)
2019	387	0.095	0.96	-0.795	-0.0012	1.22E-04	0.47	1.60E-04	-0.017	0.059	-0.016	0.056

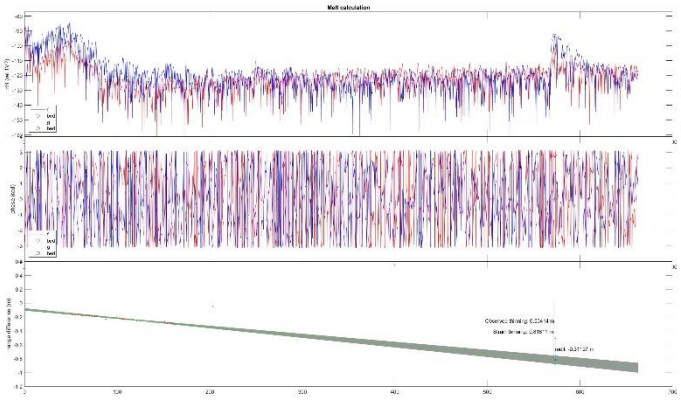

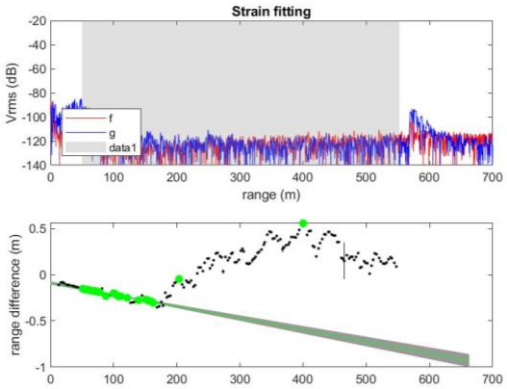

T20

Year	Repeat time (Days)	Correg Shift (m)	Correg Correlation	Thickness change (m)	Strain Rate (/yr)	Error (/yr)	R^2	P	Melt (m)	Error (m)	Melt Rate (m/yr)	Melt Rate Error (m/yr)
2019	387	0.047	0.97	-0.678	-0.001	3.55E-05	0.73	2.04E-13	0.155	0.017	0.146	0.016

First Basal Reflection

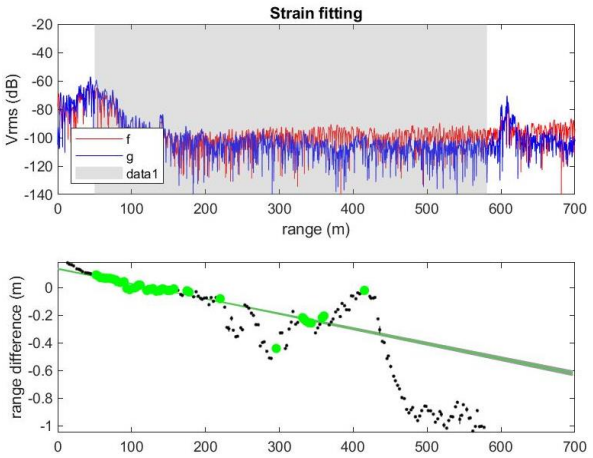

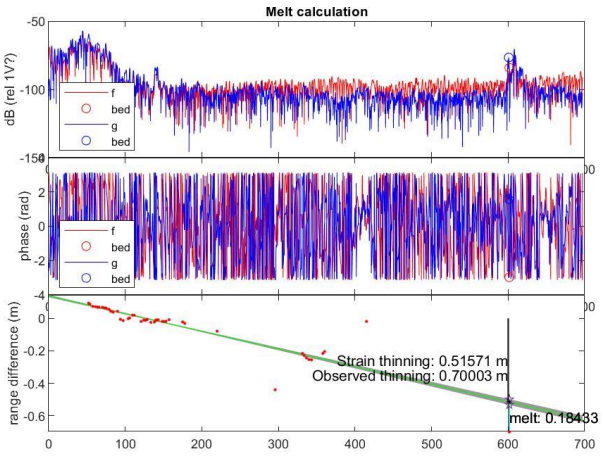

Second Basal Reflection

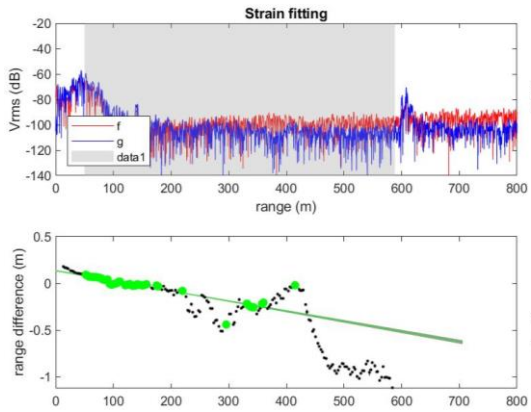

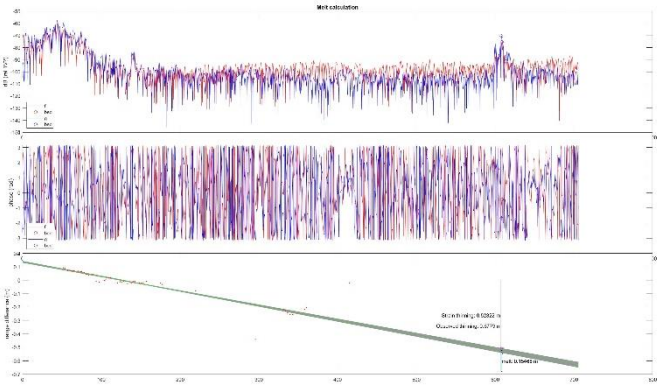

T21

Year	Repeat time (Days)	Correg Shift (m)	Correg Correlation	Thickness change (m)	Strain Rate (/yr)	Error (/yr)	R^2	P	Melt (m)	Error (m)	Melt Rate (m/yr)	Melt Rate Error (m/yr)
2019	387		0.95	-0.632	-4.76E-04	6.48E-05	0.14	0.083259	0.302	0.036	0.285	0.034

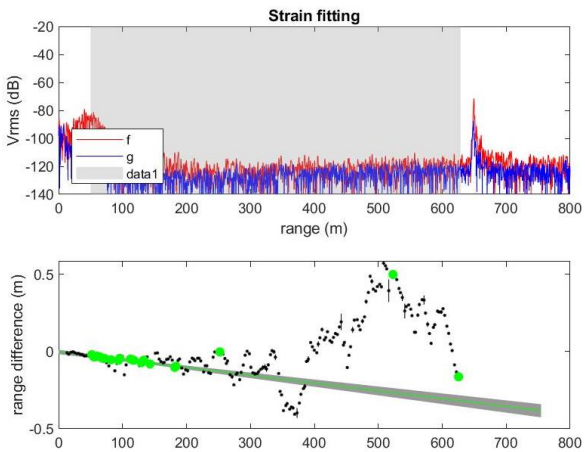

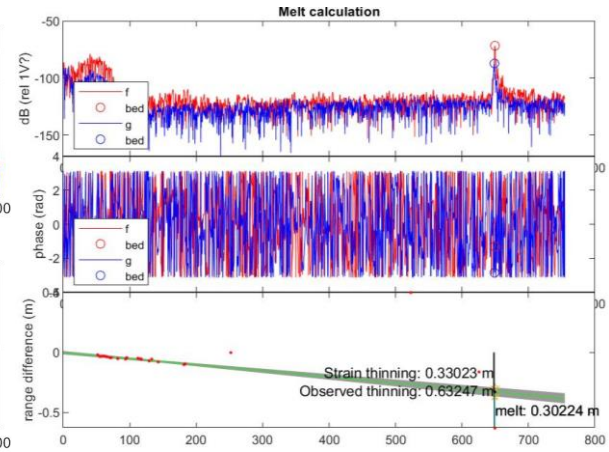

P1

Year	Repeat time (Days)	Correg Shift (m)	Correg Correlation	Thickness change (m)	Strain Rate (/yr)	Error (/yr)	R^2	P	Melt (m)	Error (m)	Melt Rate (m/yr)	Melt Rate Error (m/yr)
2019	387	0.128	0.97	-0.519	-3.48E-04	3.42E-05	0.86	1.11E-16	0.281	0.019	0.265	0.018

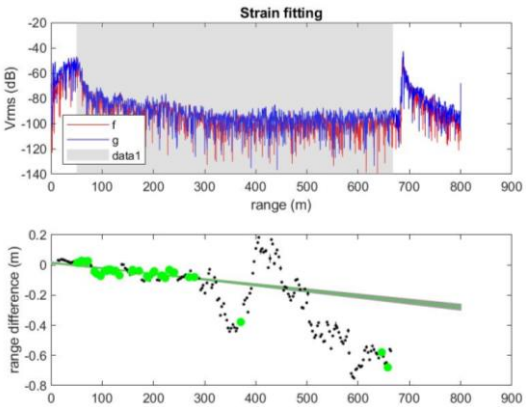

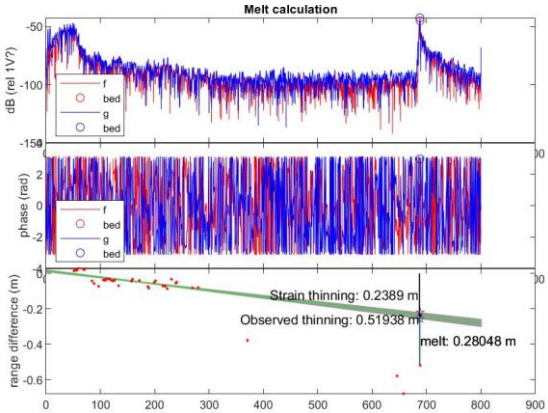

P2

Year	Repeat time (Days)	Correg Shift (m)	Correg Correlation	Thickness change (m)	Strain Rate (/yr)	Error (/yr)	R^2	P	Melt (m)	Error (m)	Melt Rate (m/yr)	Melt Rate Error (m/yr)
2019	387	0.128	0.96	-0.124	-2.19E-04	1.12E-04	0.66	5.52E-09	-0.060	0.063	-0.057	0.059
2020	360	0.035	0.96	-0.357	-4.04E-04	6.60E-05	0.00	7.43E-01	0.184	0.031	0.186	0.032

2019

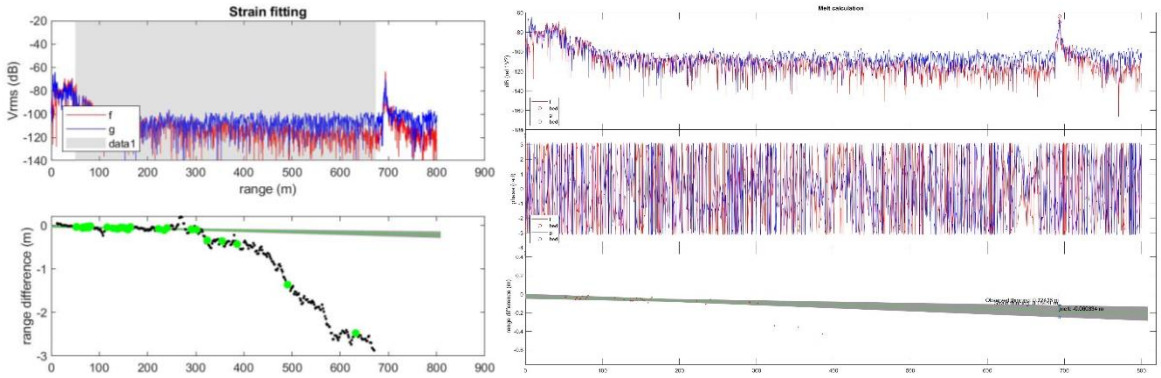

2020

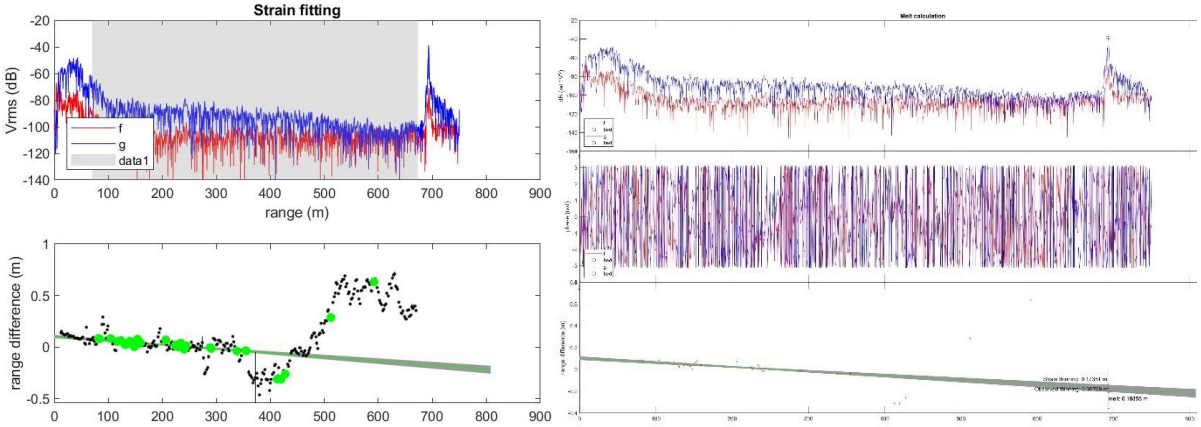

P3

Year	Repeat time (Days)	Correg Shift (m)	Correg Correlation	Thickness change (m)	Strain Rate (/yr)	Error (/yr)	R^2	P	Melt (m)	Error (m)	Melt Rate (m/yr)	Melt Rate Error (m/yr)
2019	413	0.043	0.97	0.223	4.62E-04	1.52E-05	0.95	3.29E-33	0.103	0.008	0.091	0.007
2020	360	-0.021	0.97	0.136	3.65E-04	4.22E-05	0.504	6.67E-08	0.074	0.0198	0.0746	0.0201

2019

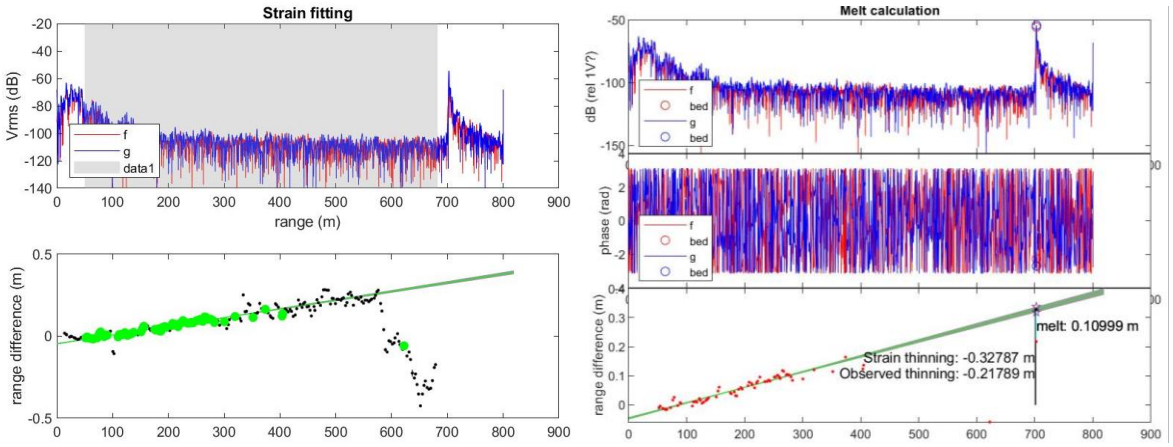

2020

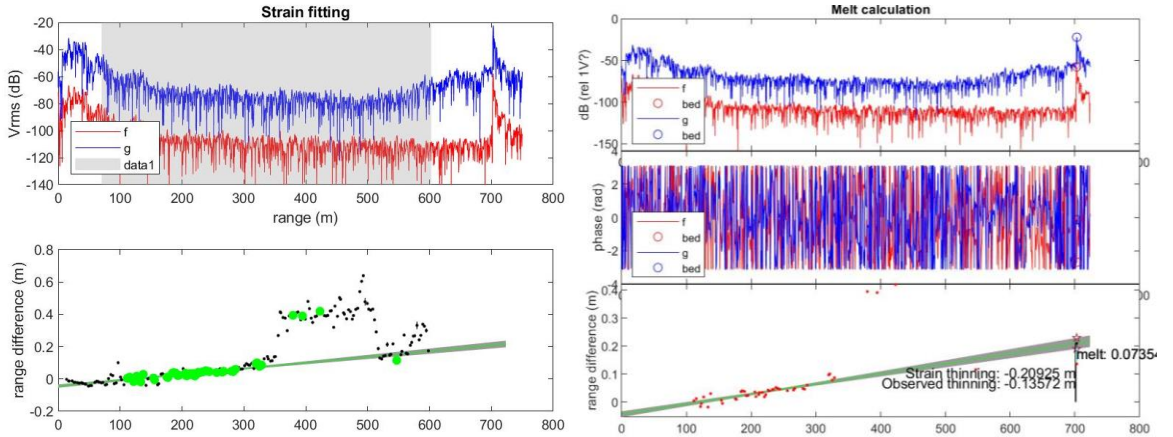

P4

Year	Repeat time (Days)	Correg Shift (m)	Correg Correlation	Thickness change (m)	Strain Rate (/yr)	Error (/yr)	R^2	P	Melt (m)	Error (m)	Melt Rate (m/yr)	Melt Rate Error (m/yr)
2019	411	0.128	0.99	-0.113	-1.02E-04	8.54E-06	0.42	1.22E-13	0.014	0.004	0.012	0.003
2019-20	772	0.043	0.98	-0.072	-8.36E-05	1.30E-05	0.67	5.29E-27	0.041	0.0105	0.0192	0.005

2019

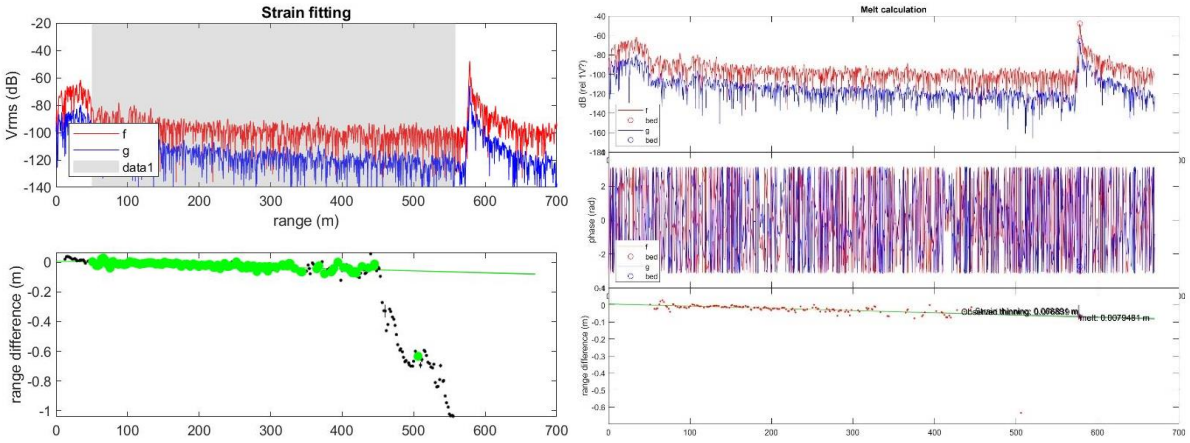

2019-20

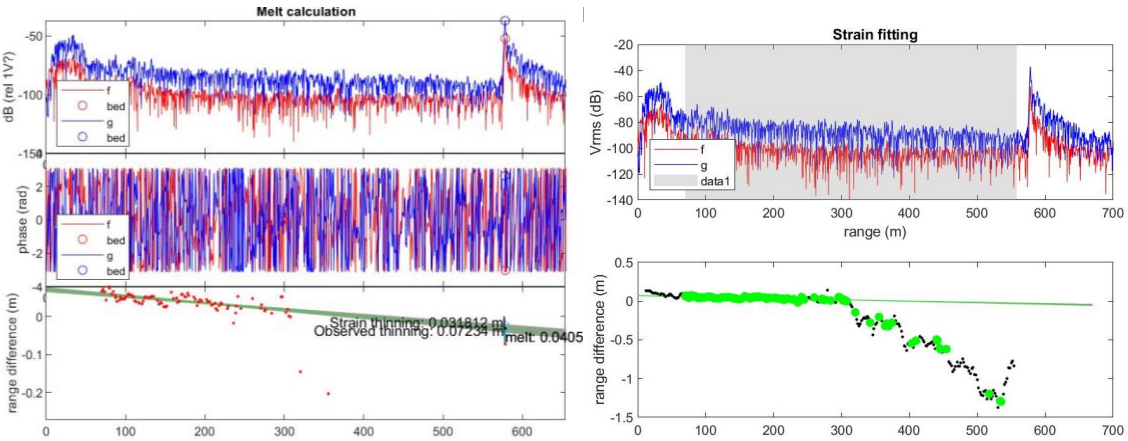

P5

Year	Repeat time (Days)	Correg Shift (m)	Correg Correlation	Thickness change (m)	Strain Rate (/yr)	Error (/yr)	R^2	P	Melt (m)	Error (m)	Melt Rate (m/yr)	Melt Rate Error (m/yr)
2019	386	0.043	0.99	-0.272	-3.68E-04	5.13E-06	0.97	1.43E-103	0.015	0.002	0.014	0.002

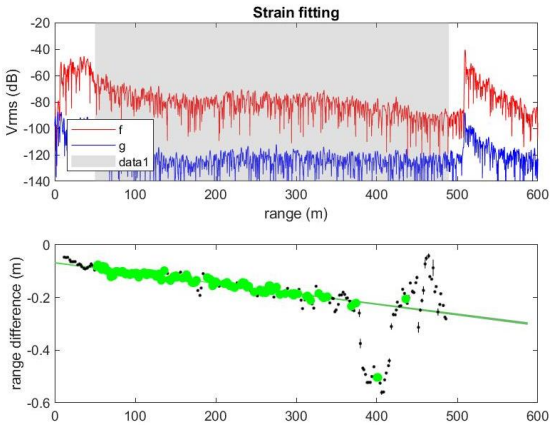

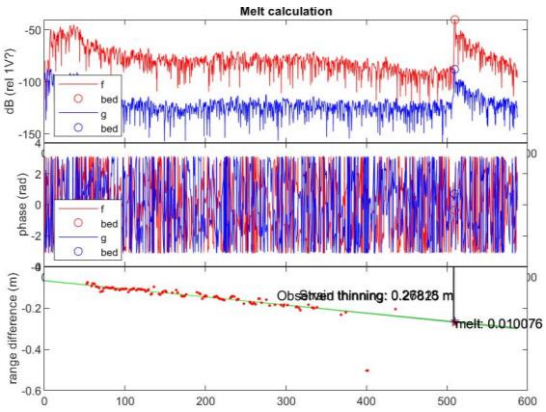

P6

Year	Repeat time (Days)	Correg Shift (m)	Correg Correlation	Thickness change (m)	Strain Rate (/yr)	Error (/yr)	R^2	P	Melt (m)	Error (m)	Melt Rate (m/yr)	Melt Rate Error (m/yr)
2019	408	0.043	0.94	-0.110	-1.71E-04	3.28E-05	0.60	4.21E-04	0.002	0.012	0.002	0.011

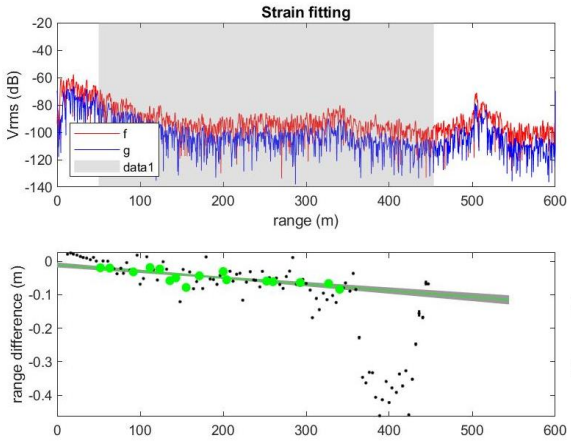

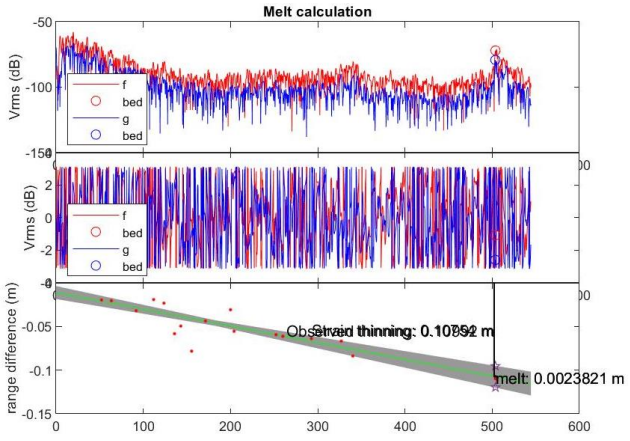

P7

Year	Repeat time (Days)	Correg Shift (m)	Correg Correlation	Thickness change (m)	Strain Rate (/yr)	Error (/yr)	R^2	P	Melt (m)	Error (m)	Melt Rate (m/yr)	Melt Rate Error (m/yr)
2019	408	0.085	0.97	-0.550	-9.55E-04	1.08E-05	0.99	1.97E-86	0.010	0.004	0.009	0.003

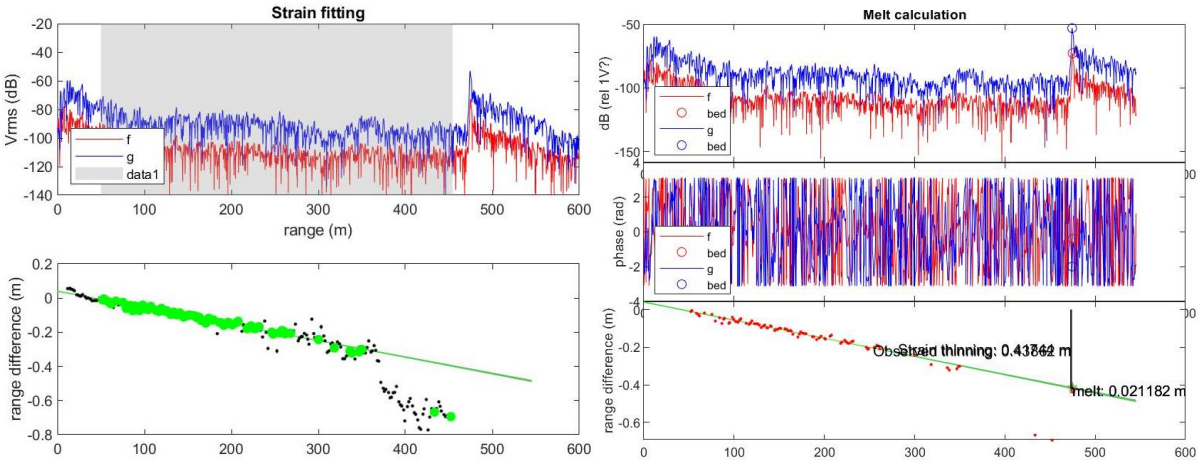

P8

Year	Repeat time (Days)	Correg Shift (m)	Correg Correlation	Thickness change (m)	Strain Rate (/yr)	Error (/yr)	R^2	P	Melt (m)	Error (m)	Melt Rate (m/yr)	Melt Rate Error (m/yr)
2019	385	0.043	0.98	-0.434	-8.07E-04	1.08E-05	0.98	7.04E-77	0.023	0.004	0.022	0.003

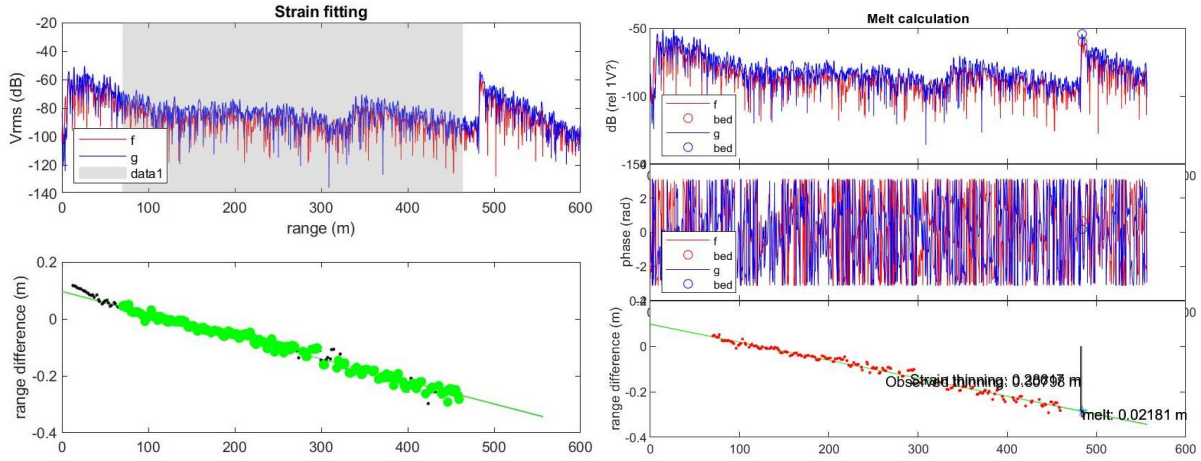

P9

Year	Repeat time (Days)	Correg Shift (m)	Correg Correlation	Thickness change (m)	Strain Rate (/yr)	Error (/yr)	R^2	P	Melt (m)	Error (m)	Melt Rate (m/yr)	Melt Rate Error (m/yr)
2019	406	0	0.921	-0.345	-6.68E-04	7.52E-06	0.99	2.12E-72	0.025	0.003	0.022	0.002

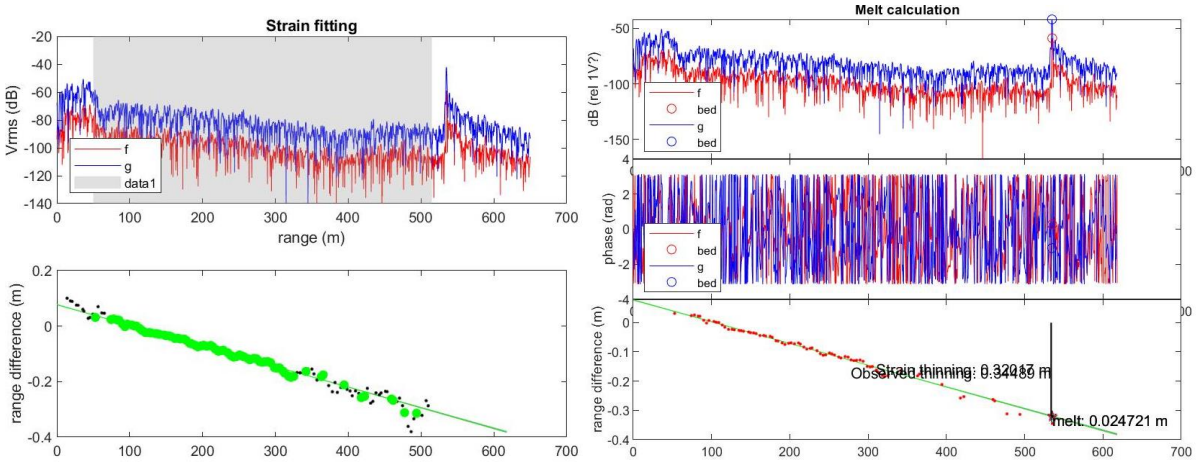

P10

Year	Repeat time (Days)	Correg Shift (m)	Correg Correlation	Thickness change (m)	Strain Rate (/yr)	Error (/yr)	R^2	P	Melt (m)	Error (m)	Melt Rate (m/yr)	Melt Rate Error (m/yr)
2019	406	0.000	0.96	-0.336	-0.00056	9.90E-06	0.97	1.03E-71	0.045	0.004	0.040	0.003

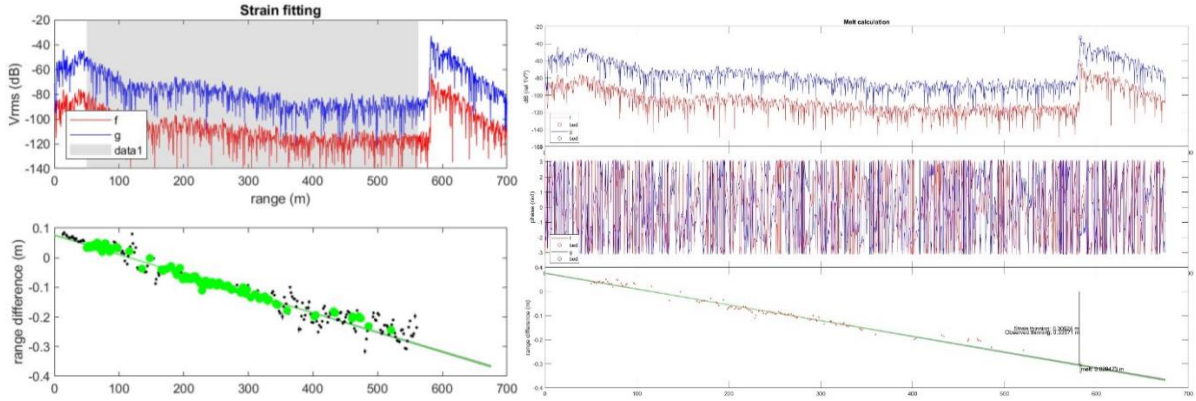

P11

Repeat time (Days)	Correg Shift (m)	Correg Correlation	Thickness change (m)	Strain Rate (/yr)	Error (/yr)	R^2	P	Melt (m)	Error (m)	Melt Rate (m/yr)	Melt Rate Error (m/yr)
383	-0.043	0.92	-0.354	-0.00044	2.86E-05	0.85	3.66E-20	0.152	0.012	0.145	0.011